Mario Arar

Investigations on Morphology and Electrode Modification in Organic/Inorganic Hybrid Solar Cells

PhD Thesis

Graz University of Technology

Institute for Chemistry and Technology of Materials

Head: Univ.-Prof. Dipl.-Ing. Dr.techn. Franz Stelzer

Supervisor: A.o. Univ.-Prof. Dipl-Ing. Dr.techn. Gregor Trimmel

Graz, September 2013

Statutory Declaration

I declare that I have authored this thesis independently, that I have not used other than the declared sources/resources, and that I have explicitly marked all material which has been quoted either literally or by content from the used sources.

Graz, _____   _____

           Date   Signature

Eidesstattliche Erklärung[1]

Ich erkläre an Eides statt, dass ich die vorliegende Arbeit selbstständig verfasst, andere als die angegebenen Quellen/Hilfsmittel nicht benutzt, und die den benutzten Quellen wörtlich und inhaltlich entnommene Stellen als solche kenntlich gemacht habe.

Graz, am _____   _____

           Datum   Unterschrift

---

[1]Beschluss der Curricula-Kommission für Bachelor-, Master- und Diplomstudien vom 10.11.2008; Genehmigung des Senates am 1.12.2008

Acknowledgements

"There is a fine line between wrong and visionary. Unfortunately you have to be a visionary to see it."

Sheldon Cooper (2009) [1]

First and foremost, I want to thank my supervisor Prof. Gregor Trimmel, who gave me the opportunity of researching for my thesis as the first physicist in a chemist's workgroup and perpetually supported me with helpful guidance. Furthermore, Dr. Andreas Pein deserves my humble thanks: he introduced me to this topic and was a tireless teacher and discussion partner. The same is true for Dr. Thomas Rath, a mine of information always having a sympathetic ear.

I further want to thank my dear colleagues for welcoming me from the very first day. The great atmosphere in the whole institute, our workgroup and our office made the last years fly past; in particular, I want to emphasize some people who enlightened my days with discussions, challenges and fun: I am much obliged to Christopher Fradler, Lukas Hauser, Meinhart Roth, and Andreas Pein (once more).

My special thanks are extended to the people in my everyday life:

My family, especially my parents, who paved the way for this thesis by enabling the way itself.

My friends, who maintained my work-life-balance in so many marvelous ways. Albeit there are many who would deserve to be listed here and it might seem unfair, I only want to mention Thomas Rothländer, who had to be both my friend but also the only one to proof-read this manuscript.

My love, Katharina - listed last, but always my prime!

Abstract

"[...] the acquisition of a new truth is like the acquisition of a new sense, which renders a man capable and recognizing a large number of phenomena that are hidden from another, as they were from him originally."

Justus von Liebig (1844)

(cited by Pauli (Fischer, trans.) (1907) [2])

Photovoltaics is the most obvious option for an enduring and stable energy supply. Thereof, nanocomposite solar cells have emerged as an interesting branch; their absorber layer is a blend of an organic and an inorganic nanoparticular semiconductor. At least in theory, they should be able to outperform classic inorganic solar cells, as they could combine the advantages of both types: among others, polymers offer flexible and lightweight thin layers through solution processing, inorganic nanoparticles allow for band gap tuning and good intrinsic properties. However, they still lack in terms of power conversion efficiency.

In the first part of this thesis the significance of the blend morphology on the solar cell's performance is investigated. In a series of nanocomposite PSiF-DBT:CIS solar cells with different polymer:inorganic ratios, the influence of interpenetrating networks is elucidated. The impact on charge carrier generation and percolation was scrutinized by means of I-V measurements, TEM/EDXS and TAS analyses, and supported through drift-diffusion-based simulations. Additionally, the separate contribution of the inorganic phase was studied by embedding the CIS nanoparticles into a polystyrene matrix, which is electronically inactive in the observed regime. Again, different polymer:inorganic ratios were examined and a surprising performance of the pure CIS-phase could be recognized, with the best solar cells exhibiting 1/4 of the power conversion efficiency compared to PSiF-DBT:CIS solar cells.

The second part describes a novel cathode modification by introducing a thin silver interlayer prior to the aluminum top cathode. In PSiF-DBT:CIS solar cells this modification shows a substantial increase in power conversion efficiency,

which is achieved through a significant enhancement in fill factor. Compared to pure Al and Ag cathodes, respectively, the relative enhancement amounts to approximately 25%. Introducing this small amount of silver does not lead to a continuous layer but to silver nanoparticles that develop inside an aluminum oxide interlayer formed between absorber layer and cathode. The improvement is found to be based on an enhanced charge carrier extraction. This cathode modification was also applied to polymer:PCBM solar cells; however, no performance increase could be observed. These findings lead to the assumption that the CIS-electrode interface could be the main obstruction.

Zusammenfassung

"[...] die Erwerbung einer neuen Wahrheit ist ein dem Menschen zugewachsener neuer Sinn, der ihn jetzt befähigt, eine Menge von Erscheinungen wahrzunehmen und zu erkennen, die einem andern unsichtbar und verborgen bleiben, wie sie es früher ihm selbst waren."

Justus von Liebig (1844) [3]

Die naheliegendste Option für eine dauerhafte und stabile Energieversorgung ist die Photovoltaik. Aus ihr entwickelte sich ein sehr interessanter Zweig: die Nanokompositsolarzellen. Diese zeichnen sich dadurch aus, dass ihre Absorberschicht eine Mischung aus organischen und anorganischen nanokristallinen Halbleitern ist. Zumindest theoretisch sollte es ihnen möglich sein, klassische anorganische Halbleiter zu übertreffen, da sie die Vorteile beider Materialien vereinen könnten: Polymere bieten unter anderem die Möglichkeit, aus der Lösung heraus flexible und leichte dünne Schichten aufzutragen. Anorganische Nanopartikel erlauben eine Abstimmung der Bandlücke und weisen gute intrinsische Eigenschaften auf. Allerdings konnten sie beim Wirkungsgrad bisher noch nicht gleichziehen.

Der erste Teil dieser Arbeit hebt die Wichtigkeit der Morphologie der Aktivschicht in Bezug auf die Leistung der Solarzelle hervor. In einer Versuchsreihe wurden PSiF-DBT:CIS Nanokompositsolarzellen mit unterschiedlichen Polymer:Anorganik-Verhältnissen hergestellt, um den Einfluss der sich gegenseitig durchdringenden Netzwerke zu beleuchten. Deren Auswirkung auf die Ladungsträgererzeugung und -perkolation wird zusätzlich mittels I-V-Messungen, TEM/EDXS sowie TAS Analysen und unterstützt durch Drift-Diffusions-Modell-basierte Simulationen untersucht.

Weiters wird der separate Beitrag der anorganischen Phase betrachtet, indem die CIS-Nanopartikel in eine Polystyrolmatrix eingebettet werden, welche im betreffenden Bereich elektronisch inaktiv ist. Wiederum erfolgt eine Untersuchung mit unterschiedlichen Polymer:Anorganik-Verhältnissen, die eine überraschend gute Leistung der reinen CIS-Phase offenbart.

Im zweiten Teil wird eine neuartige Kathodenmodifikation beschrieben, bei der eine dünne Silberzwischenschicht vor der Aluminiumkathode aufgebracht wird. Wendet man diese Modifikation in PSiF-DBT:CIS Solarzellen an, ergibt sich ein bedeutender Anstieg im Wirkungsgrad, der auf einer deutlichen Verbesserung des Füllfaktors beruht. Im Vergleich mit reinen Al- bzw. Ag-Elektroden erfahren diese Solarzellen eine relative Steigerung um etwa 25%. Das Einbringen dieses geringen Silberanteils führt nicht zu einer durchgehenden Schicht sondern zu Silbernanopartikeln, die sich in einer Aluminiumoxidschicht zwischen Aktivschicht und Kathode bilden. Diese Optimierung fußt auf einer verbesserten Ladungsträgerextraktion.

Diese Kathodenmodifikation wird zusätzlich in Verbindung mit Polymer:PCBM Solarzellen untersucht, allerdings kann dabei keine Verbesserung beobachtet werden. Diese Resultate führen zu der Annahme, dass die zu überwindende Barriere am Übergang CIS-Elektrode zu finden ist.

Contents

Contents

1. Introduction

"I'd put my money on the sun and solar energy. What a source of power! I hope we don't have to wait until oil and coal run out before we tackle that."

Thomas A. Edison (1931)

(cited by Newton (1989) [4])

1.1. Motivation for Photovoltaics

Prologue

In the late antiquity, alchemists sought after the philosopher's stone, a legendary chemical for transforming something common and inexpensive (base metal) into something greatly desired (gold or silver). In modern times, we are in pursuit of something similar: converting a readily available resource (solar radiation - which happens to be everlasting, according to human timescales) into a greatly desired goal: supplying the worlds energy demand infinitely. Hence, the research towards enhancing photovoltaics can perhaps be regarded to as "the quest for the modern philosopher's stone".

Admittedly, the history of photovoltaics is not limited to the last decades, according to Butti and Perlin it dates back to ancient Greek and Rome, about 2500 years ago.[5] However, the necessity for clean and renewable energy has never been greater.

Since the Second Industrial Revolution (also known as Technological Revolution) in the late 19th century the world's energy demand expanded rapidly, accompanied by a growing exploitation of natural resources. Fossil fuels provided a cheap and easily accessible energy supply; possible depletion or environmental pollution was neglected. Globalization, progressing industrialization and growth of world population steadily increased the energy requirements. As displayed in Figure 1.1, the world's energy production more than
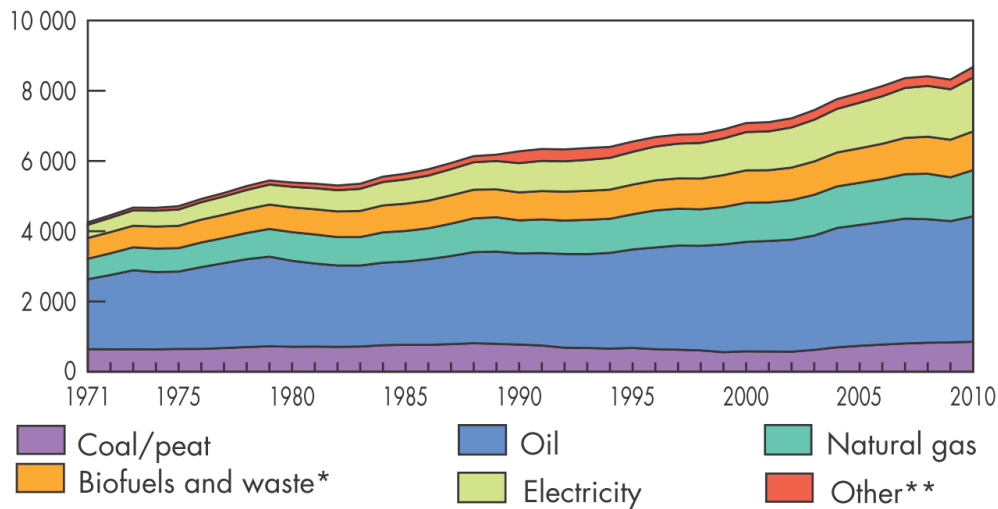
Figure 1.1.: World's total energy consumption from 1971 to 2010 subdivided by type. *Data prior to 1994 for biofuels and waste final consumption have been estimated. **Other includes geothermal, solar, wind, heat, etc.; Key World Energy Statistics ©OECD/IEA, 2012.[6]

doubled in the time period from 1971 to 2009.[7] The main branches of production are still of fossil origin, the contribution of solar energy is marginal at best.

However, in 2011 the International Energy Agency published their *Solar Energy Perspectives* [7], where a brighter future for photovoltaics is predicted. According to their estimations, in 2060 solar driven energy forms could contribute more than a third of the total energy demand (see Figure 1.2).

Our sun perpetually radiates energy to the earth at neither cost nor strain. The final frontier is to increase the conversion efficiency of solar power at competitive costs, reducing the need for non-renewable energy sources.

Oil 5%
Gas and coal 8%
Baseload 7%
Biofuels 13%
Biomass heat 6%
Geothermal heat 1%
Hydropower 6%
PV 13%
CSP 18%
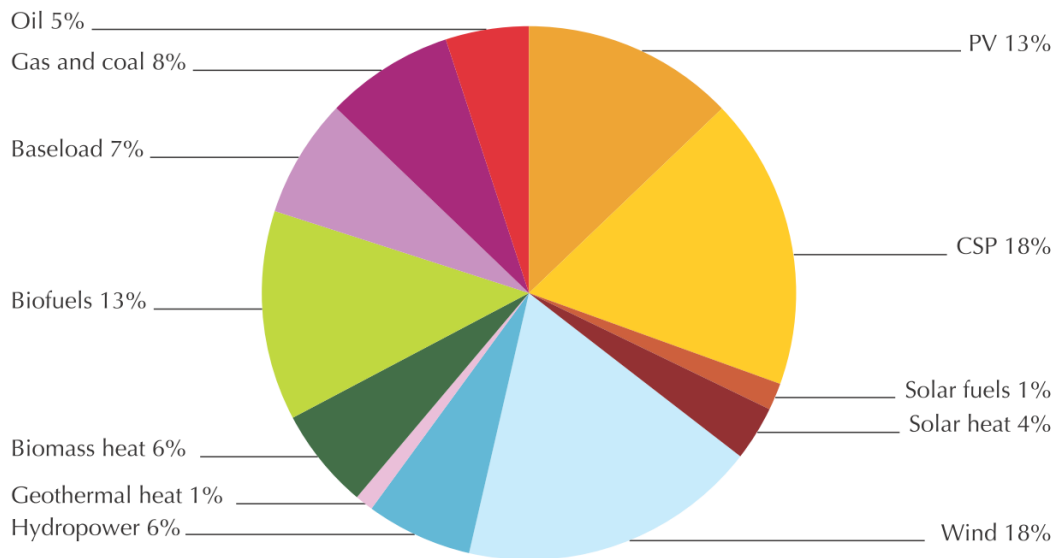Solar fuels 1%
Solar heat 4%
Wind 18%

Figure 1.2.: Estimation of total energy demand in 2060, subdivided by providing sources (PV: photovoltaics; CSP: concentrated solar power); Solar Energy Perspectives ©OECD/IEA, 2011.[7]

1.2. Next Generation: Polymer-Based Photovoltaics

The major benefits of photovoltaics, as mentioned above (Sec. 1.1), are apparent. Unfortunately, due to their production costs they are still not competitive to current primary energy sources on the large scale, albeit in certain regions individual photovoltaic solutions are definitely yielding a profit (monetarily and/or infrastructurally).

A hopeful step towards cost-effectiveness was the introduction of third-generation photovoltaics: polymer-based solar cells. From a technological point of view, polymer-based photovoltaics are unmatched when considering processing parameters as speed, cost, simplicity, and thermal energy demand.[8] However, owing to their still low power conversion efficiency (PCE), the processing advantages do not directly reflect the full cost of photovoltaic

electricity generation.

Over the last two decades the scientific community experienced great interest in polymer-based photovoltaics, research groups emerged and publication numbers of respective scientific papers grew exponentially. Additionally, some notable companies started to produce photoactive polymers on an industrial scale: a clear step towards commercialization. One recent branch of research introduces a hybrid form of solar cells where the organic matrix is interpenetrated by an inorganic semiconductor for several further advantages, which is also the foundation of this thesis. A common denominator with fully organic solar cells is the ease of processibility at still low PCEs. Though they are in the early stages of development compared to conventional Si-solar cells, they have achieved rapid PCE progression lately.

This development nourishes hope that this generation of photovoltaics manages to become an equal competitor to classical inorganic solar cells.

1.3. Aims of this Thesis

The main subject of this work was to investigate and gain knowledge regarding two vital issues: (i) the impact of different morphologies in nanocomposite solar cells, and (ii) the processes at the interface between electrodes and absorber layer. Thus, the scientific work presented in this thesis can be divided into two parts, subdivided into two separate chapters each:

Part 1: Morphology   The first part of this thesis comprises studies regarding the morphology of hybrid solar cells.

In **Chapter 3, "Variation of PSiF-DBT:CIS mass ratio"**, organic/inorganic hybrid solar cells (PSiF-DBT:CIS) were prepared and thoroughly investigated. Additionally, in cooperation with the Institute of Theoretical Physics of the Graz University of Technology, simulations to the morphological study were performed. Based on this experimental and theoretical approach conclusions about the performance of these hybrid solar cells could be drawn.

Chapter 4, "Polystyrene:CIS solar cells", covers an approach to fabricate solar cells, consisting of a resembling inorganic phase as above, embedded in a photo-inactive polystyrene matrix. This series was prepared to gain further knowledge about the separate photovoltaic contributions of each material.

Part 2: Electrode modification   A second topic spans investigations about a novel electrode modification and its impact on polymer-based solar cells.

In **Chapter 5, "Silver-modified Aluminum Electrodes in PSiF-DBT:CIS Solar Cells"**, a modification of the typical aluminum electrode with silver nanoparticles is introduced. A substantial increase in fill factor can be found, which is scrutinized thoroughly.

As a subsequent step, **Chapter 6, "Silver-modified Aluminum Electrodes in Polymer:PCBM Solar Cells"**, describes the examination of the influence of this electrode modification on polymer:PCBM solar cells.

2. Basics

"[...] we have to remember that what we observe is not nature herself, but nature exposed to our method of questioning."

Werner Heisenberg (1959) [9]

The well-established elemental principles presented in this chapter are only a brief summary; the interested reader is referred to three handbooks. If not noted otherwise, the basics concentrated in here can be found in these books:

- *The Physics of Solar Cells*, by Nelson [10]

- *Practical Handbook of Photovoltaics: Fundamentals and Applications*, edited by Markvart and Castañer [11]

- *Organic photovoltaics: mechanisms, materials, and devices*, edited by Sun and Sariciftci [12]

2.1. Photovoltaics: A Survey

To start off with, some of those most important milestones of the near past are listed, with emphasis on polymer-based solar cells, which led the way towards state-of-the-art photovoltaics. The used phrases and terms will be properly explained in the subsequent parts of this chapter.

1839 - Becquerel first observed and reported the photovoltaic effect as a consequence of illuminating certain materials in acidic solutions connected to electrodes.[13]

1887 - Hertz investigated spark jumps from an induction coil. He observed decreased spark lengths in absence of ultraviolet (UV) radiation and, thus, discovered the photoelectric effect.[14]

1905 - Einstein published four groundbreaking papers, whereof in the first he explained the photoelectric effect on discrete *energy quanta*.[15] In 1921 he received the Nobel Prize in Physics "for his services to theoretical physics, and especially for his discovery of the law of the photoelectric effect".[16]

1954 - Chapin, Fuller, and Pearson from Bell Telephone Laboratories published the first practical silicon p-n-junction photocell that achieved about 6% efficiency.[17] In the following decades many scientific and commercial technologies follow.

1958 - Kearns and Calvin presented the first photovoltaic "bilayer" system, consisting of magnesium phthalocyanine disks coated with a thin film of air-oxidized tetramethyl p-phenylenediamine.[18]

1978 - Morel et al. broke the 1% efficiency threshold for organic photovoltaic devices.[19]

1986 - Tang introduced the heterojunction concept for organic photovoltaics, making the charge carrier generation efficiency independent from bias voltage, thus, providing solar cells with high fill factors.[20]

1991 - O'Regan and Grätzel report a solar cell using dye-sensitized colloid titanium dioxide (TiO_2) films: dye-sensitized solar cells (DSSCs; also widely known as Grätzel cells) are brought into being.[21]

1992 - Sariciftci et al. were the first to publish photoinduced electron transfer from a polymer to buckminsterfullerene,[22] the basic form of today's most sophisticated acceptor material for organic photovoltaics.

2002 - Huynh, Dittmer, and Alivisatos demonstrated the first hybrid solar cell, where cadmium selenide (CdSe) nanorods act as inorganic acceptor material in an organic matrix.[23]

2012 - Heliatek announced to have crossed the 10% border with an organic (tandem) solar cell, reaching a certified power conversion efficiency of 10.7%.[24]

2013 (Sep) - The currently highest power conversion efficiency (reported by Heliatek) amounts to 12%.[25]

2.2. Organic Solar Cells

A fundamental distinction between inorganic and polymer-based solar cells consists in the generation of charge carriers. The common denominator is the excitation of electrons through incoming photons with an energy equal or greater than their band gap. In both cases excitons are generated, a pair of electron and corresponding hole bound by Coulombic interaction.

In typical inorganic semiconductors, the binding energy only amounts to a few electron volt (eV), so a dissociation of the charge carriers at room temperature is highly probable. The necessary field is provided at "homojunctions", *e.g.*, at the interface between two differently doped regions of the same semiconductor material. Typical organic semiconductors, however, produce excitons with strong Coulombic attraction (0.1 - 1.4 eV [26]), which demand an additional process for charge separation. For this purpose, a second material with an energetically fitting band is introduced. At the interface between these two

materials, the "heterojunction", an energetic difference exists, which offers a more favorable state for electrons, dissociating the bound electron-hole pair by transferring the electron to the other material. Due to this charge transfer, the latter material is denoted as *acceptor*, the first as *donor*.

The term "organic solar cell" denominates solar cells with both donor and acceptor being organic semiconductors. They are generally formed by a π-conjugated system, groups of carbon atoms with alternating single and multiple bonds. This system offers two great advantages: (i) good electronic transport properties (based on the relaxed delocalisation of electrons) and (ii) good optical properties.[27]

Their most prominent advantage is the almost infinite variety of structures due to chemical tailoring. It allows adjusting physical-chemical properties such as energy levels, solubility, processibility, *etc*. However, opposing to inorganic semiconductors, doping of organic solar cells is restricted to interstitials. Substitution is not an appropriate option as thereby chemical bonds can be broken easily.[27, 28].

The performance of organic solar cells greatly depends on the materials used but also on device layout, interlayers, additives, and, of course, the production process itself. A closer look at these topics is given in this and the following section.

2.2.1. Device Architecture and Physics

A basic layout of polymer-based solar cells is depicted in Fig. 2.1. Typically, it consists of an optically transparent substrate (*e.g.*, glass), a transparent elec-

trode (tin doped indium oxide (ITO)), the absorber layer and a metallic (reflecting) top electrode. In most cases, additional layers for performance augmentation are introduced; here a hole transport layer (HTL) is depicted (sometimes also termed electron blocking layer (EBL)); the influences of electrodes and interlayers are described in Sec. 2.2.3. The composition of the absorber layer is the major attribute of solar cells; both material (combination) and structure affect the physical processes occurring in the layer and are, therefore, crucial factors in the performance of solar cells (*vide supra*).
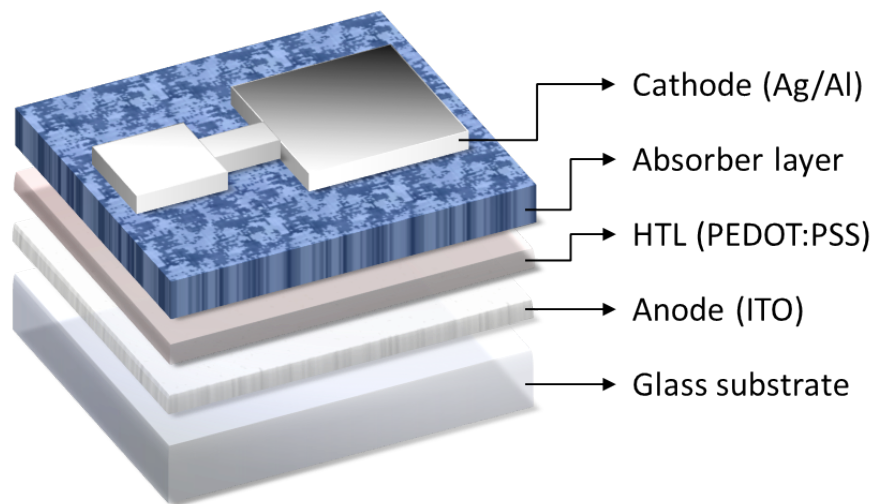

Figure 2.1.: Scheme of a typical organic solar cell layout.

A variation of this scheme is found in inverted solar cells, which are principally built upside-down. As a matter of course the choice of cathode materials changes as well as the use of interlayers. This layout has proven to be more stable [29, 30], with a PCE catching up on the records set with normal layouted polymer-based solar cells.[28]

2.2.1.1. Device Layouts

This section describes the differences in the physical processes resulting from a change of composition and morphology of the absorber layer of polymer-based solar cells. The influences of interlayers are neglected for the moment; only the absorber layer sandwiched between two electrodes is considered.

Separating excitons demands a driving force, which is in most cases a junction between semiconductor and metal (single layer) or between two semiconductors (bilayer, heterojunction, see Fig. 2.2). The lifetime of excitons (which is in the nanosecond regime [31]) distinctly limits their diffusion length; therefore, the device layout has a great impact on exciton dissociation and recombination, respectively. The following paragraphs illustrate diverse layouts for polymer-based solar cells as well as the charge carrier generation principles.

Single layer   Bilayer   Bulk heterojunction
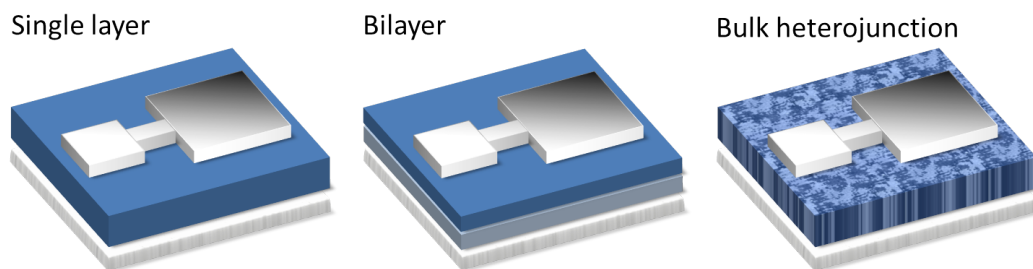
Figure 2.2.: Simplified scheme of typical solar cell device layouts; the absorber layers are sandwiched between two electrodes (top and bottom layer).

Single Layer In a single layer setup, the absorber layer only consists of a (doped) semiconductor; the separation takes place at the semiconductor-metal junction provided that they have differing work functions. Bringing the two materials together enforces an equilibration of their Fermi levels through

exchange of charge carriers across the junction (see Fig. 2.3). It is important to mention that the displayed relative values of the vacuum levels are only illustrations of a possible trend and shall not be taken for granted. Therefore, the vacuum level is omitted in the subsequent paragraphs.
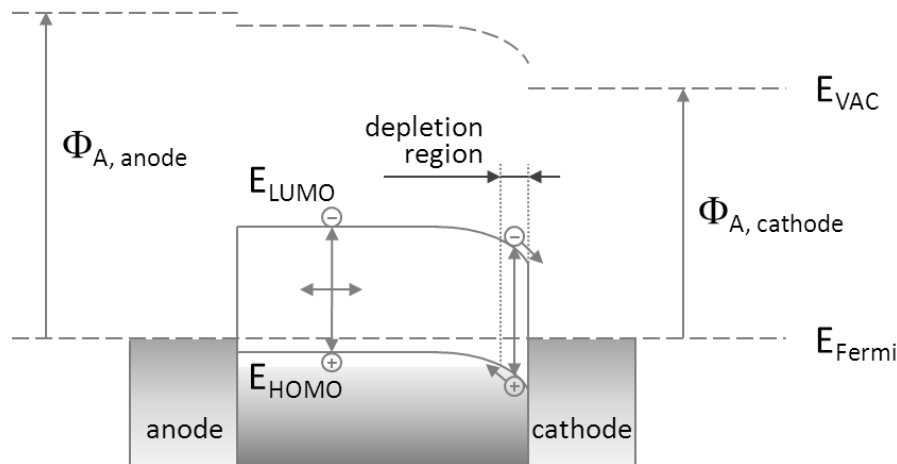

Figure 2.3.: Energy level scheme of a p-type semiconductor/metal junction and the occurring band bending through Fermi level pinning (E_{VAC}: vacuum level energy, E_{Fermi}: Fermi level energy, $E_{HOMO/LUMO}$: HOMO/LUMO energy levels of the semiconductor, Φ_A: work function of the anode or cathode)

This exchange is localized in the direct vicinity of the interface, where the bands of the semiconductor are bent towards the metal's levels, until the Fermi levels are equilibrated. The Fermi level of the semiconductor is thus pinned to that of the metal; accordingly, this effect is called "Fermi level pinning". If the metal's work function is higher than the semiconductor's, a Schottky-barrier is formed at the interface; its height is defined as difference between conduction (valence) band and Fermi level for n-type (p-type) semiconductors. If the Schottky-barrier reaches a certain height, a depletion region is formed which results in (for solar cells) typical rectifying properties. In case of a lower metal

work function, an ohmic contact is formed.[32]

The semiconductor's band energies in the bulk are unaffected; therefore, a potential gradient is built up, resulting in an electrostatic field at the junction. In this region, also called "space charge region", a diametrically opposed driving force for electrons and holes, respectively, is established and, thus, charges are being separated in this region. The space charge region does not extend very far into the semiconductor, so it is highly unlikely for excitons to be dissociated.

Bilayer A step towards better exciton dissociation is achieved through introduction of a second material with a different ionization potential and electron affinity to form a bilayer (see Fig. 2.4). If the difference of the two LUMO levels exceed the binding energy of the exciton, an efficient dissociation can be achieved. Organic/organic interfaces typically have aligned vacuum levels [33]; however, in case of organic/inorganic junctions strong interface dipoles may occur similar to metal/(in)organic interfaces. For the sake of understanding, these effects are excluded (an extensive review on this subject was published by Koch [34]).

One of the biggest advantages of this setup is the separated charge transfer: in the course of exciton dissociation the electrons are transferred to the material with the higher electron affinity. The holes remain in the other layer; therefore, the probability of recombination is reduced. Based on their preference of providing (donating) and collecting (accepting) electrons these materials are called donor and acceptor, respectively.
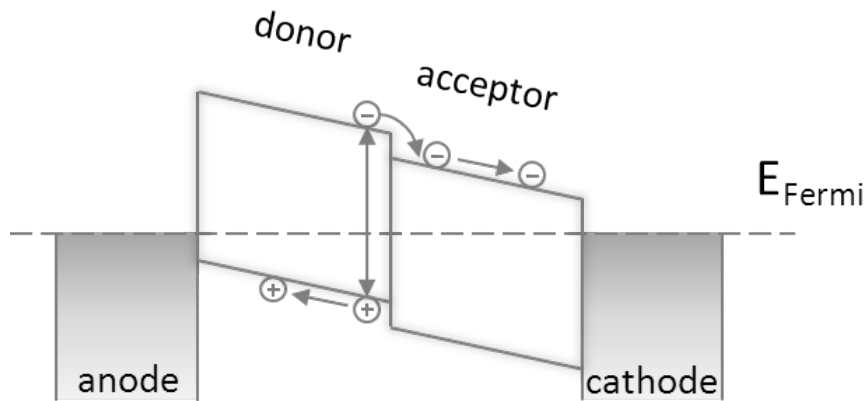
Figure 2.4.: Scheme of energy levels and exciton dissociation in a bilayer device.

Bulk Heterojunction   A big disadvantage of the bilayer structure is obvious: strong absorption, even with the high absorption coefficients of organic semi-conductors (typical factor: $\approx 10^3$, cf. [35, 36]), requires some layer thickness. The thicker the absorbing layer is, the longer is the mean distance for excitons to get to the interface. Therefore, this layout limits the efficiency as a trade-off between absorption and generation probability. As a logical consequence, the mean exciton diffusion length had to be reduced while maintaining the ab-sorber layer thickness, resulting in the bulk heterojunction device, where donor and acceptor are blended to a joint bulk with interpenetrating networks.[20, 37, 38]

These interpenetrating networks ensure short distances from each exciton gen-eration spot to a dissociating interface, thus, reducing recombination (as illus-trated in Fig. 2.5). A drawback of this structural type is the possibility of island formation; these (donor or acceptor) islands are dead ends for charge carriers, which are trapped and lost for current generation. Furthermore, an exact con-
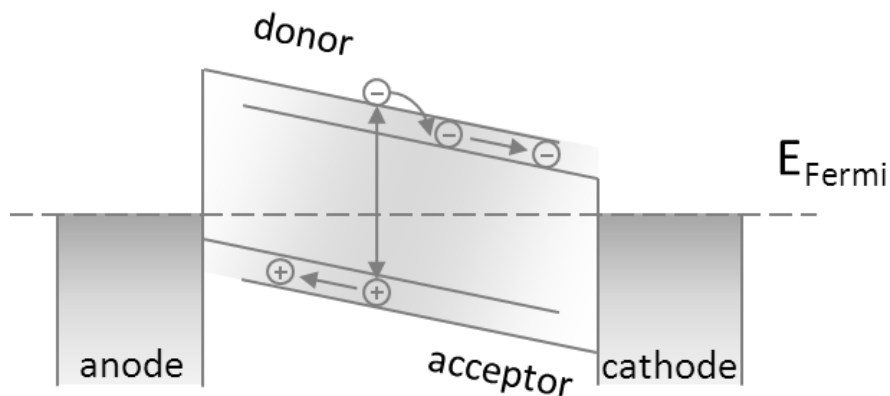
Figure 2.5.: Scheme of energy levels and exciton dissociation in a bulk heterojunction device.

trol of the morphology is virtually impossible; therefore, a multitude of experimental variables and parameters is introduced with this structure. However, due to its high efficiency this layout is the most common (*e.g.*, [39–41]).

Structured Heterojunction The theoretically ideal structure in terms of charge carrier generation would be a comb-like structure (at least in 2D) which offers both short distances to interfaces and continuous pathways for free charge carriers.[42] The realization of such a structure still poses a challenge due to the small dimensions; in particular, stable structures at the necessary aspect ratios form an obstacle hard to overcome.

A comparison of comb-like structures with more realistic morphologies using simulations based on the drift-diffusion model was, *e.g.*, presented by Gruber et al.[43]

Tandem Solar Cell In a single polymer-based solar cell the amount of absorbed (and utilized) photons is limited by the absorption ability of the used polymer and inorganic semiconductor. Photons with wavelengths not subject to absorption can easily pass through the layer and are, thus, lost for the process of charge carrier generation. A possibility to circumvent this issue is applying a second solar cell on top of the first one, ideally with a complementary absorption range, so as to absorb the unaffected photons (although two identical subcells can also exhibit high values, as reported by You et al. [44]). Typically, the two subcells are connected in series with a recombination layer, in which the electrons of the lower subcell recombine with holes from the upper subcell; thus, the sum of each subcell's open circuit voltage (V_{OC}) can be gained. Their respective remaining electrons and holes provide the current; its value is restricted by the subcell with the lower short circuit current (I_{SC}).[45] Based on the detailed balance limit of efficiency (reported by Shockley and Queisser [46], hence known as Shockley-Queisser limit), which determines the theoretical efficiency maximum of a single p-n junction solar cells, DeVos calculated the maximum efficiency for multiple subcells. According to his work, the maximum efficiency for a solar cell with a band gap of about 1 eV can be enhanced from ≈30% to ≈42% in tandem setup.[47]

2.2.1.2. Absorber materials

The most import characteristic of absorber materials is their band gap, which determines the threshold energy for photons to be absorbed. The smaller the band gap the more photons can be absorbed. However, for photons with en-

ergies higher than the band gap, the residual energy is converted in form of thermalization losses; additionally, smaller band gaps result in lower V_{OC}s.[48] To determine the most beneficial band gap, the energy distribution of the solar radiation at a given latitude at the earth's surface has to be taken into account. This eventually led to numerical simulations and calculations to identify an ideal band gap, indicating an ideal range of 1.1 to 1.7 eV for a single junction solar cell.[49] Kroon et al. emphasize in their review that in polymer-based bulk heterojunction systems the interplay between donor and acceptor plays an essential role and each systems ideal band gap has to be determined separately.[50]

Not only the band gap is crucial for a useful semiconducting material, but also its charge carrier mobility plays an essential role and so does abundance, toxicity, processibility and, of course, its price.

Amongst the most common donor polymers is poly(3-hexylthiophene-2,5-diyl) (P3HT); it offers a relatively small monomer unit (one thiophene unit with organic moiety) and good properties regarding morphology control.[51] While P3HT is popular for research, record cells always utilize low-band gap polymers due to their outstanding absorption.[52] As acceptor material there is no way of avoiding phenyl-C61-butyric-acid-methyl ester (PCBM) (or similar fullerene derivatives), as it can be found in virtually every organic record cell.[53]

2.2.2. Characteristic Solar Cell Parameters

The electrical characterization of a solar cell is determined through I-V measurements, which can be transferred to the typically used J-V curves by dividing the measured current through the solar cells active area (see Appendix, Sec. A.2.1, Eq. (A.1)). The green line in Fig. 2.6 illustrates such an exemplary J-V curve of a solar cell under illumination. Two important parameters can be directly obtained from this graph, namely V_{OC} and I_{SC} (and short circuit current density (J_{SC}), respectively).
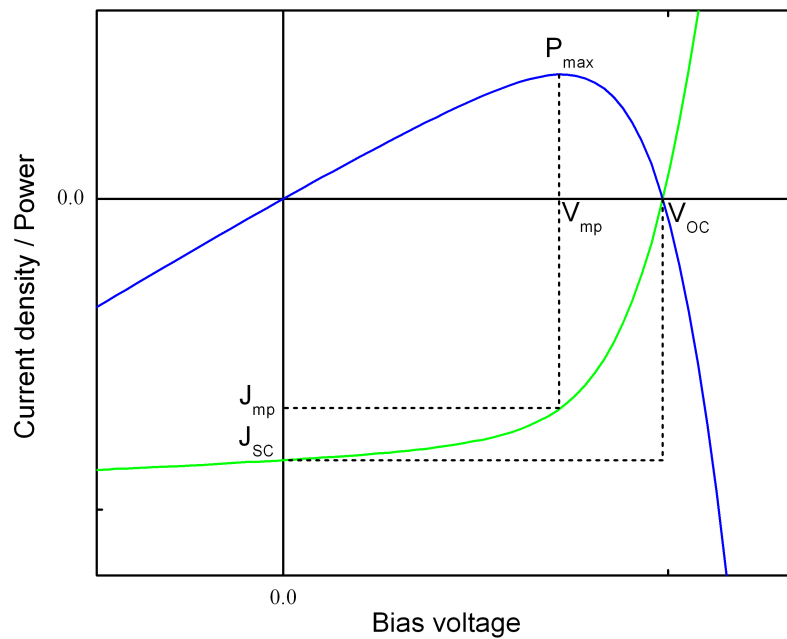

Figure 2.6.: Illustration of characteristic solar cell parameters. Green line: exemplary J-V curve; blue line: respective power generation plot. Marked values are described in the text.

V_{OC} represents the potential difference between the two electrodes without external load, *i.e.*, when there is no flow of current. Accordingly, I_{SC} is the current flowing through the solar cell, when the potential across the solar cells equals zero, *i.e.*, I_{SC} corresponds to the maximum current to be provided from the solar cell (*vide supra*).

Additionally, the electric power (P) can be calculated from the measured current (I) at a certain bias voltage (V) as

$$P = V\,I \tag{2.1}$$

The fourth quadrant of the J-V curve represents the operating regime of the solar cell, with the maximum power point (P_{max}) as the cell's operating point at corresponding voltage at the maximum power point (V_{mp}) and current density at the maximum power point (J_{mp}). The rectangles spanned by (V_{mp} x J_{mp}) and (V_{OC} x J_{SC}), respectively, represent the actual and theoretical maximum power outputs of the solar cell. Their ratio is the definition of the fill factor (FF):

$$FF = \frac{V_{mp}\,J_{mp}}{V_{OC}\,J_{SC}} \tag{2.2}$$

which can be understood as "quality factor" of the solar cell, with an ideal cell when FF equals 1.

The most prominent and, thus, important parameter of a solar cell is its PCE, sometimes also denoted as η. It describes the power provided by the solar cell

relative to the incident light power (P_{in}):

$$\eta = \frac{V_{mp} \, J_{mp}}{P_{in}} \cdot 100\% = \frac{V_{OC} \, J_{SC} \, FF}{P_{in}} \cdot 100\% \tag{2.3}$$

Another important index for solar cells is the incident photon to electron conversion efficiency (IPCE), also known as external quantum efficiency (EQE), which indicates the ratio of generated electrons per photons impinging on the solar cell (not to be confused with the internal quantum efficiency (IQE), which only takes absorbed photons into account):

$$IPCE = \frac{h \, c}{e} \cdot \frac{I_{SC}}{\lambda \, P_{in}} \cdot 100\% \tag{2.4}$$

The formula contains Planck's constant (h), speed of light (c), elementary charge (e), and wavelength (λ). For the utility of IPCE see Appendix, Sec. A.2.3.

2.2.3. Electrodes and Interlayers

Chen et al. have thoroughly investigated various influences of interfacial layers and reported them extensively.[54] In this subsection, only the most important facts for this work will be reproduced.

2.2.3.1. Electron Blocking Layers

The purpose of EBLs is to avoid a transport of electrons to the "wrong" electrode and also to block an injection of electrons into the absorber layer at high bias voltages while preserving an unobstructed hole extraction path.[55] Furthermore, ITO as bottom electrode exhibits a relatively large surface roughness, so a smooth EBL provides an additional advantage in terms of coating.

The most common EBL material is poly(3,4-ethylenedioxythiophene)-poly(styrenesulfonate) (PEDOT:PSS), a transparent conductive polymer with fitting energy levels to act as electron blocker. Alternatives are, *e.g.*, molybdenum oxide (MoO_3), vanadium oxide (V_2O_5) [56], and graphene oxide (GO) [57].

2.2.3.2. Hole Blocking Layers

Conversely, certain interlayers can be utilized as hole blocking layers between absorber layer and respective electrode. They have either a low work function in case of metals or a high highest occupied molecular orbital (HOMO) in case of semiconductors. Most common materials are titanium oxide (TiO_x) [58] and zinc oxide (ZnO) [59]. Further interesting possibilities base on polyelectrolytes, which influence the interface dipole between absorber layer and electrode.[60]

2.2.3.3. Electrode Materials

Necessary features of both top and bottom electrodes are a good conductivity and work functions fitting to the absorber materials. Of course, non-toxicity, abundance, good processibility and low-cost apply here as well. Bottom electrodes additionally have to be transparent, limiting the options. Typically, transparent conductive oxides are used (*e.g.,* ITO, fluorine doped tin oxide (FTO) or aluminum doped zinc oxide (AZO)) as well as silver micro-grid/PEDOT:PSS-layers. But recently patterned nanostructures and graphene sheets also emerge as transparent electrodes.[61, 62]

Top electrodes not only extract charge carriers but usually also reflect the incoming irradiation to effectively double the active layer thickness; therefore, (besides cost) high reflectivity and conductivity are the main selection criteria. Aluminum is a common choice, although due to its non-noble nature it is unfavorable in terms of stability. Silver has a slightly less beneficial work function at a higher cost; however, it is practically insusceptible to oxidation and is thus also a popular choice.

Solar cells with an inverted layout necessitate materials with higher work functions; albeit expensive, gold is a common choice.

Sometimes electrodes are additionally modified with certain interlayers which support charge carrier transport, blocking or extraction. Such an interlayer is thoroughly characterized in Sec. 5.

2.3. Organic/Inorganic Hybrid Solar Cells

In (fully) organic solar cells both absorber layer materials, donor and acceptor, are organic compounds. A different approach has been, *e.g.*, studied and reported by Greenham, Peng, and Alivisatos, who investigated charge separation and transport in organic-inorganic composites.[63] Solar cells with inorganic nanocrystals, also termed *hybrid* and/or *nanocomposite* solar cells, became a topic of interest for several groups. Inorganic nanoparticles are reported to have a multitude of advantages, especially in terms of versatility.[64]

First of all, there is vast assortment of possibilities; combining a fitting inorganic semiconductor with a conjugated polymer might allow for broadband absorption due to complementary wavelength sensitivities. Alivisatos pointed out, that nanocrystals can be a powerful instrument based on the ability to change their size and shape (*e.g.*, spheres, rods, fibers).[65] This offers a direct access to their band gaps, but can also provide influence on the morphology of absorber layers and, as a consequence thereof, on charge carrier dynamics.[66] Some of the more closely investigated materials are, *e.g.*, lead selenides [67] and sulfides [68], cadmium selenides [69] and sulfides [70], and copper indium selenides [71] and sulfides [72, 73].

2.3.1. The Organic Donor: PSiF-DBT

The conjugated polymer used in most parts of this work is PSiF-DBT, a polysilafluorene derivative as described by Wang et al. [74] Its chemical structure is depicted in Fig. 2.7. With highest (HOMO) and lowest unoccupied molecular
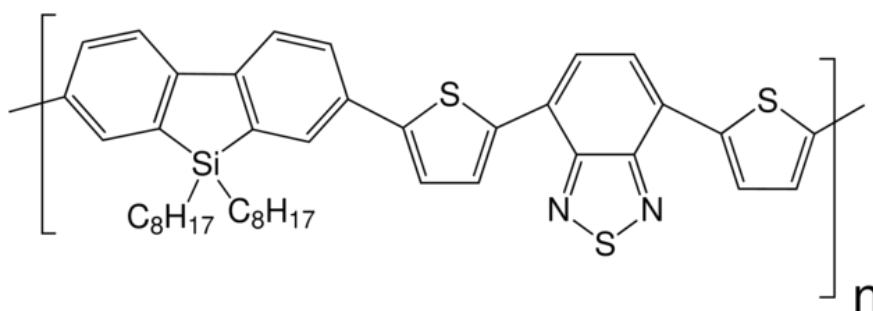
Figure 2.7.: Chemical structure of PSiF-DBT.

orbital (LUMO) levels of -5.39 and -3.57 eV, respectively, the optical band gap amounts to 1.82 eV.[74] This value should strike a balance between absorption capabilities and a good basis for a high V_{OC}; the latter is directly depending on the difference between the (p-type) donor's HOMO and the (n-type) acceptor's LUMO.[75] However, this is by far not the only influence; the V_{OC}'s origin is still disputed and, thus, field of great interest, *e.g.*, in [76–78].

Wang et al. have reported a PCE of 5.4% using a PSiF-DBT:PCBM absorber layer[74]; for a relatively uncommon material this high value clearly identifies the polymer as a worthy contestant.

2.3.2. The Inorganic Acceptor: Copper Indium Sulfide

In its crystalline form, copper indium disulfide ($CuInS_2$) is a ternary chalcopyrite (see Fig. 2.8) with a band gap of about 1.5 eV.[79] An exceptional feature of $CuInS_2$ is its tolerance to stoichiometry variations; additionally, a deviation from the stoichiometric Cu:In ratio leads to n-type conductivity in In-rich phases and, conversely, p-type behavior in Cu-rich phases.[80] A combination

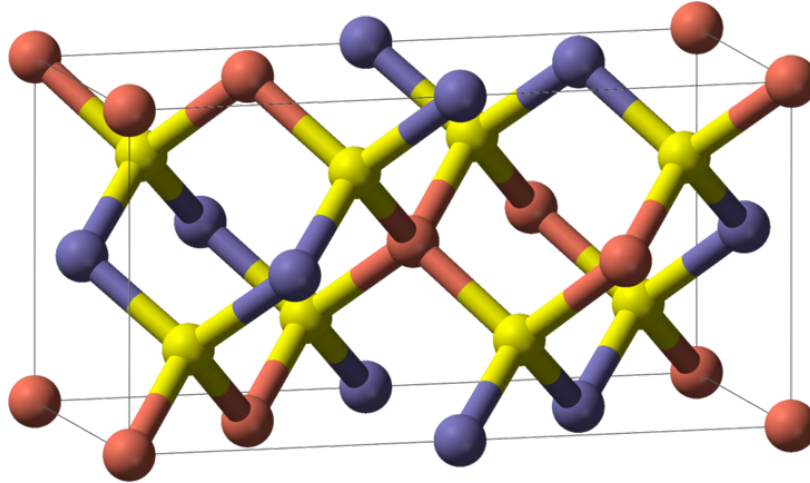of both properties offers a wide field of application.

Figure 2.8.: Chemical structure of a CuInS$_2$ elementary cell. Cu: red balls, In: blue, S: yellow.

In polymer-based solar cells copper indium sulfide (CIS) typically appears in a doped, non-stoichiometric state (therefore, CuInS$_2$ is replaced by CIS), often in a nanocrystalline form. Due to quantum confinement effects optical and electronic features are size dependent.[81] According to Arici, Sariciftci, and Meissner the band gap of CIS nanoparticles may even extend by 0.4 eV in each direction, increasing the band gap up to 2.3 eV.[82]

With this tuneability and its high extinction coefficient in the range of $\approx$1·10^{-5} cm^{-1} [83] it is a promising candidate for hybrid nanocomposite solar cells.

2.3.3. Forming Nanocomposite Layers

The nanocomposite layers presented in this work are prepared via the *in situ* route, where the nanoparticles are formed directly inside the polymer layer.[84] This is achieved through metal xanthate precursors, which decompose at a certain temperature to metal sulfides and volatile organic byproducts. Necessary decomposition temperatures are notably below 200 °C; this allows an application of these precursors in practically all conjugated polymers. An extensive review on the subject of *in situ* syntheses was published by Rath and Trimmel.[85]
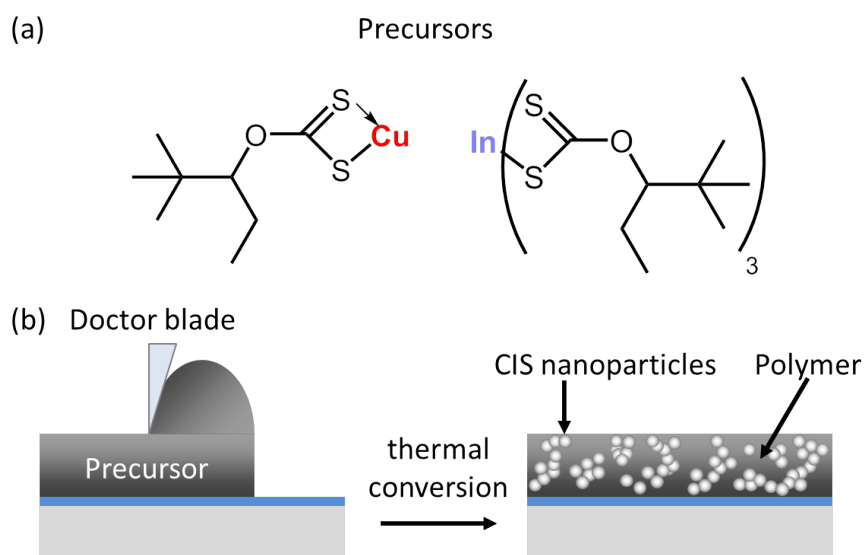
Figure 2.9.: Chemical structure of the precursors used to form CIS nanoparticles.[72] ©2012 American Chemical Society

The formation process is depicted in Fig. 2.9; in this work, a solution of copper and indium O-2,2- dimethylpentan-3-yl dithiocarbonate precursors (Fig. 2.9(a)) is mixed with PSiF-DBT; this solution is doctor bladed on the substrate

and subsequently subjected to thermal treatment at $\leq$ 200 °C (Fig. 2.9(b)).
A great advantage of this procedure is the formation of stable nanoparticles
without the need for capping ligands (and the accompanying process steps).
Thus, a nanocomposite layer is formed without the need of interfering addi-
tives.

3. Variation of PSiF-DBT:CIS mass ratio

"I must confess it was very unexpected and I am very startled at my metamorphosis into a chemist."

Ernest Rutherford (1908)

(cited by Dardo (2004) [86])

The following chapter is a reviewed and revised submission to

Influence of morphology and polymer:nanoparticle ratio on device performance of hybrid solar cells – an approach in experiment and simulation

Mario Arar, Manfred Gruber, Michael Edler, Wernfried Haas, Ferdinand Hofer, Neha Bansal, Luke X. Reynolds, Saif A. Haque, Karin Zojer, Gregor Trimmel and Thomas Rath

While the discussions on the simulation results emanate from a fruitful co-operation, the actual realization of the simulations presented in this chapter have been conducted by M. Gruber and K. Zojer. The TAS measurements were conducted by the team of S. A. Haque. The elucidations concerning the actual morphology by means of TEM/SAED were a valuable contribution by W. Haas (who conducted the TEM and SAED analyses and provided the respective images) and F. Hofer.

3.1. Introduction

Economic and future-oriented thinking eventually points toward a demand for renewable energy resources, whereof solar power is most promising for perpetual clean energy. Organic- or polymer-based solar cells offer cost effective processing from solution (*e.g.*, roll-to-roll coating) [8]. Therefore, they found great interest in the last couple of years and a large portion of research was devoted to polymer:fullerene solar cells, which is reflected in rather high power conversion efficiencies (PCE) approaching 10% (presently certified: 9.2% [28]) in single junction setup and 10.6% [53] as tandem cells. Up to now, this clearly surpasses those of hybrid solar cells, *i.e.*, inorganic semiconductor nanoparticles blended with a conjugated polymer, which at the present time steadily approach 5% PCE [87, 88]. However, the concept of inorganic-organic hybrid solar cells is still in the early stages of development, but experiences increasing attention and relevance based on promising features: (i) the shape and size of inorganic nanostructures can be altered in various ways to optimize the morphology of the hybrid absorber layer. By using nanorods or tetrapods instead of spherical nanoparticles, charge carrier transport can be enhanced maintaining a high interfacial area. (ii) Nanoparticles of diverse semiconductors with various band gaps and absorption profiles are readily available; in addition, their band gaps can be altered through size modification due to the quantum confinement effect in small nanoparticles [81, 89, 90]. Thus, incorporation of proper nanoparticles into the active layer can provide supportive absorption in complementary wavelength ranges. (iii) Inorganic nanoparticles are environmentally more stable and exhibit higher intrinsic charge carrier mobilities

32

compared to conjugated polymers [23]. The hybrid bulk-heterojunction (BHJ) system investigated herein is prepared *in situ* in one step using metal xanthate precursors. Blending these precursors with a conjugated polymer and subjecting the layer to mild thermal treatment, the metal xanthates decompose to form metal sulphide nanoparticles directly in the polymer matrix without by-products remaining in the absorber layer and without the necessity of using capping ligands for the stabilization of the nanoparticles. This innovative route was originally presented for the preparation of polymer:CdS [91, 92] and polymer:CIS [72, 93] hybrid solar cells. However, this versatile route can also be used to prepare hybrid solar cells comprising other material combinations like polymer:Sb$_2$S$_3$ [94] or small molecule:CIS [73]. Reynolds *et al.* [95] already showed that *in situ* prepared nanoparticles tend to form agglomerates in the polymer matrix, which is not the case, if the absorber layers are prepared using pre-synthesized, ligand stabilized nanoparticles. This agglomeration influences both donor-acceptor interface area and transport properties, and thus has significant impact on device performance. Furthermore, it is very likely that in the *in situ* formation process varying the acceptor loadings in the absorber layer has substantial impact on the morphology, especially on the agglomerate sizes. Moreover, the effect of changing donor:acceptor ratios on the nanoparticle size is still unclear. Using the *in situ* preparation technique, where no capping ligands are needed and the nanoparticles are formed directly inside the polymer matrix via a solid-state reaction, less interfering polymer at high acceptor loadings could lead to bigger agglomerates but also larger nanoparticles, which would again change the physical properties of the active layer [96]. Morphology, agglomeration and nanoparticle sizes are substantially influenced by the

composition of the absorber layer. Thus, a proper donor:acceptor ratio is essential for good device performances of bulk heterojunction solar cells, which has been shown and thoroughly investigated for several polymer:fullerene systems [97, 98]. Also for hybrid solar cells prepared via the classical route, where nanoparticles are formed separately with capping ligands and then blended with the polymer, experiments concerning the polymer:nanoparticle ratio in the absorber layer were already carried out [99, 100] and a certain excess of the inorganic nanoparticle phase turned out to be necessary for good device performance. However, thorough studies on this topic were not reported up to now for *in situ* prepared hybrid solar cells, and the knowledge based on hybrid solar cells prepared via the classical route cannot be transferred directly to *in situ* prepared hybrid solar cells. Therefore, in this study we investigate hybrid solar cells with absorber layers in which poly[(2,7- silafluorene)-*alt*-(4,7-di-2-thienyl-2,1,3-benzothiadiazole)] (PSiF-DBT; E_{HOMO} = -5.39 eV, E_{LUMO} = -3.57 eV [74]; the chemical structure is depicted in figure S1 in the supplementary data) is serving as donor with embedded copper indium sulphide (CIS; E_{HOMO} = −6.0/-5.6 eV, E_{LUMO} = -3.7/-4.1 eV [82]; see also figure S1 in the supplementary data) nanoparticles acting as acceptor; previous studies roughly indicated that a ratio of 1:9 is most beneficial for device performance [72]. Assuming a reasonable density of about 1.1 g cm^{-3} for PSiF-DBT and about 4.7 g cm^{-3} for CIS [101], respectively, this corresponds to a volumetric ratio of about 1:2. Such excess of inorganic nanoparticles is in most cases essential to ensure continuous percolation pathways in the acceptor phase which are needed for efficient charge transport [99, 102]. Exceptions to these findings are often observed if poly(3-hexylthiophene) (P3HT) is used as donor material combined with in-

organic nanoparticles; similar to P3HT:PCBM ([6,6]-Phenyl C61 butyric acid methyl ester) solar cells [103], donor:acceptor ratios of about 1:1 (v:v) suffice, *e.g.*, in P3HT:CdS absorber layers [88, 91]. In P3HT:ZnO hybrid solar cells best power conversion efficiencies have been observed for a polymer:nanoparticle volume ratio of 1:0.2 [104]. From literature data no general trend concerning most beneficial polymer:nanoparticle ratios across different material systems can be extracted. Therefore, it is essential to examine each material combination separately. The aim of this work was to elucidate experimentally how the morphology of absorber layers is affected by variation of PSiF-DBT:CIS ratios. Further focus was set on investigating the changes in device performances based on the different morphologies. In an attempt to directly connect the morphology to the I-V characteristics of the devices, three-dimensional simulations based on the drift-diffusion model under consideration of the distribution of the optical field in the solar cells were performed.

3.2. Experimental

3.2.1. Device Fabrication

PEDOT:PSS layers (Clevios P VP.AI 4083, Heraeus) were spin-coated from solution using deionized water (1:1, vol.) on glass/ITO substrates (Delta Technologies, R_S = 15 - 25 Ω/sq, sonicated in deionized water and isopropanol, O_2 plasma cleaned (FEMTO, Diener electronic)) and thermally dried in nitrogen atmosphere (150 °C, 15 min). Thereon, nanocomposite layers were prepared

by doctor blading of a chlorobenzene solution containing copper xanthates, indium xanthates (copper and indium *O*-2,2-dimethylpentan-3-yl dithiocarbonate; purchased from Aglycon, Austria; the chemical structures are depicted in figure S1 in the supplementary data) [93], and PSiF-DBT (OS0927, 1-Material, Chemsitech Inc., St. Laurent, Canada) and subsequent thermal treatment in a tube furnace (Heraeus 4/25, temperature program: 7 min heating from room temperature to 200 °C, holding time of 15 min at 200 °C) subject to nitrogen gas flow. Aluminum electrodes were deposited using a thermal evaporation chamber mounted inside a glovebox system (LABmaster dp, MBRAUN Glovebox Technology, Germany) at a base pressure of (3 - 6)x10^{-6} mbar (nitrogen atmosphere). The substrates were not cooled during evaporation.

3.2.2. Characterization

Current density-voltage (I-V) curves were recorded using a Keithley 2400 Source-Meter and custom-made Lab-View software. The solar cells were illuminated using a Dedolight DLH400D (used in conjunction with Dedolight DEB400D electronic ballast). The intensity of the incoming light was set to 100 mW cm^{-2} providing a spectrum quite similar to AM1.5G (determined using a KippZonen-CMP-11 pyranometer, no spectral mismatch was considered). The effective device area (0.04 cm^2) was defined by shadow masks applied to the solar cells. TEM analyses were conducted on a Tecnai F 20 microscope (FEI Company, 200 kV, Schottky emitter) equipped with a high resolution Gatan Imaging Filter (GIF), an UltraScanCCD camera and a Fischione HAADF STEM detector. EDX-spectrum images were acquired using a Digiscan II controller

and an EDAX Sapphire Si(Li) detector. EDX quantification was performed using the approximation for thin films by Cliff and Lorimer [105]. SAED patterns were measured on an FEI Tecnai 12 electron microscope. Layer thicknesses were additionally specified on a DekTak 150 surface profiler (Veeco). Micro- to millisecond transient absorption spectroscopy was performed on films under an N_2 environment and all data shown are scaled for the fraction of photons absorbed at the excitation wavelength. The samples were excited by a dye laser (Photon Technology International Inc. GL-301) pumped by a nitrogen laser (Photon Technology International Inc. GL-3300). Excitation was at 510 nm at an energy of 24 ± 2 µJ cm^{-2}. The samples were probed using a quartz halogen lamp (Bentham, IL1). The probe wavelengths were 1100 nm. The probe light was detected using a silicon or $In_xGa_{1-x}As$ photodiode and the signal subsequently amplified and passed through electronic band-pass filters to improve the signal to noise ratio.

3.2.3. Simulation

To simulate the impact of the volume ratio on the I-V characteristics of the devices in a direct manner, three-dimensional drift-diffusion-based simulations are performed. The device is represented by a three-dimensional slab of 100 nm x 100 nm surface area and a height corresponding to the thickness of the active layer (as schematically shown in Figure 3.1).

The slab is uniformly discretized into a mesh of 2 x 2 x 2 nm^3 voxels and 8 (=2x2x2) adjacent voxels were jointly treated as "particles" to account for the
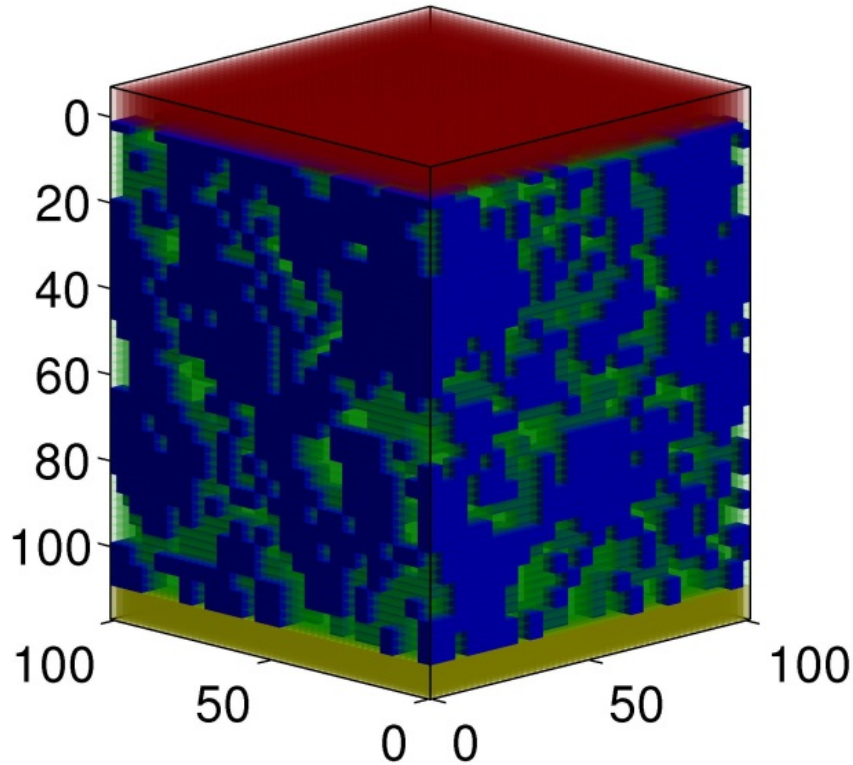
Figure 3.1.: Schematic representation of the slab used in the simulation (blend weight ratio 1:9); the extensions are given in nm, the CIS phase is indicated in blue, the polymer phase in green, PEDOT:PSS in red, and the Al cathode in yellow.

experimentally determined nanoparticle diameters of 3 nm (*vide supra*). Periodic boundary conditions were assumed at the slab's facets perpendicular to the electrodes, while injection currents are allowed to enter the device through the facets in contact with the electrodes (*vide supra*). Prior simulation of carrier transport, the interpenetrated network of polymer and nanoparticles corresponding to a given blend ratio was generated. The such generated networks ought to resemble possible morphologies that could occur upon blending the two materials under the side condition that the CIS nanoparticles tend to undergo agglomeration in the polymer matrix (as revealed by the TEM investi-

gations, *vide infra*). The distribution of light intensity within the active layer was calculated using the transfer matrix method [106]. Details related to the generation of the morphology and the calculation of the absorption profile across the device can be found in the Supplementary Data. To determine the I-V characteristics of the device, the motion of charge carriers and excitons within the generated morphology is modeled by solving the continuity equations for electrons, holes, and excitons, and the current density equations for electrons and holes self-consistently together with the Poisson equation [43, 107]. Each voxel is assigned to an effective mobility, a dielectric constant, and a transport level position. Holes are assumed to be transported in the highest occupied molecular orbital (HOMO) of the polymer and in the valence band edge of the inorganic particles; the transport levels for electrons are the lowest unoccupied molecular orbital (LUMO) and the conduction band edge, respectively. The offset of transport levels at the polymer:CIS interface was treated using generalized potentials [43, 108]. Excitons are exclusively generated within the polymer phase with a quantum efficiency of unity. Each photon absorbed within a CIS particle is assumed to be directly converted to a pair of mobile electrons and holes [43]. Further carriers are generated at the polymer:CIS interface upon dissociation of excitons arriving at the interface. The boundary conditions at the interface between the slab and the electrodes describe the injection of charge carriers via thermionic or (albeit unlikely) tunneling injection [43]; at the same time, these conditions control the amount of carriers exiting the device depending on the local electric field [107]. Excitons reaching these interfaces are quenched. The trapping and release of charge carriers in the polymer phase is considered by increasing the recombination rate by a factor

of 5 x 10^4; this is equivalent to the presence of a trap level separated by 0.27 eV from the transport levels. To be able to compare the simulated I-V curves for different blend ratios, the mobility values for electrons and holes in the polymer and in the CIS-phases, the dielectric constants, and the transport levels were kept constant for all blend ratios rather than being locally adjusted to the actual domain sizes.

3.3. Results and Discussion

The focus of this study is set on the influence of the morphology of the absorber layer on the overall device performance. In particular, the morphology and layer composition is anticipated to affect the hybrid-interface area, the percolation in both phases, and the absorption characteristics within the thin film structure. The variations in morphology were evoked by preparing a series of PSiF-DBT:CIS hybrid solar cells with different polymer:nanoparticle weight ratios, namely 1:3, 1:6, 1:9, 1:12, and 1:15, which correspond to volume ratios ranging from 1:0.7 to 1:3.5. In a first step, we analysed the influence of the different polymer:nanoparticle ratios on the morphology of the hybrid absorber layers by means of transmission electron microscopy (TEM). Therefore, thin films with weight ratios of 1:3, 1:9 and 1:15 were prepared on NaCl crystals and transferred to TEM-grids for the electron microscopic characterization. Transmission electron micrographs of these samples in two different magnifications are depicted in Figure 3.2 revealing the actual ratio-dependent morphology of the absorber layers.
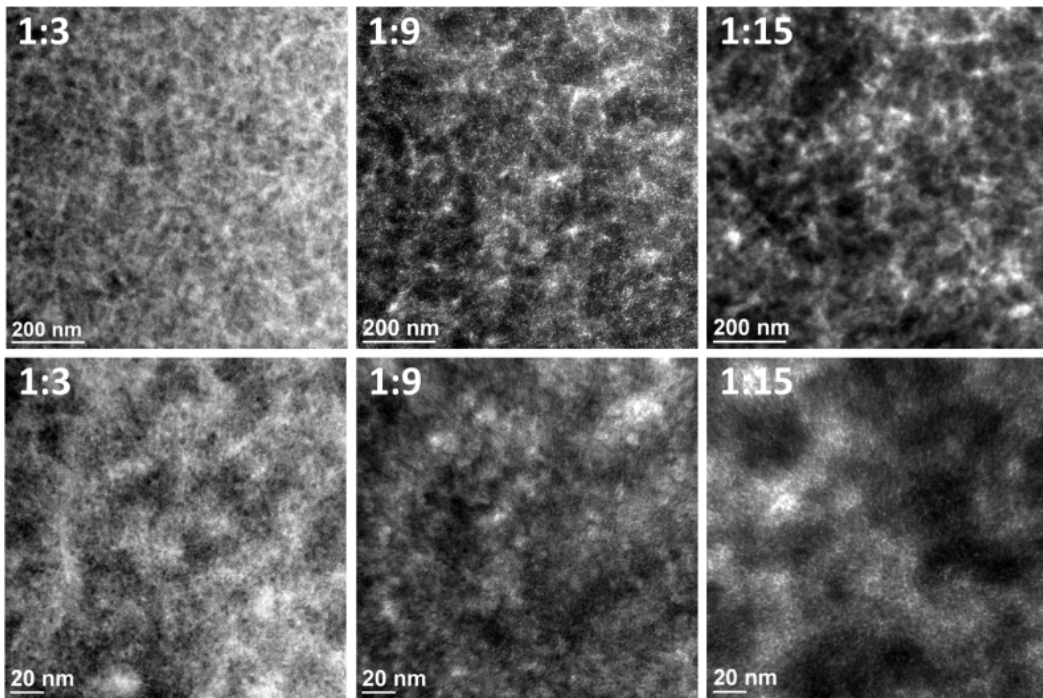
Figure 3.2.: Bright field TEM images of hybrid solar cells with different PSiF-DBT:CIS weight ratios in two different magnifications.

The lighter areas in Figure 3.2 represent regions with lower atomic number, in our case the conjugated polymer. Consequently, the darker areas identify the CIS-phase. From left to right, the polymer content decreases, resulting in more extensive darker areas. In addition, it is noticeable that not only the amount of darker regions increases, but an aggregation of the CIS phase can be observed as well. With increasing CIS content less isolated "dark" islands, which can be found in the TEM-images of the 1:3 sample, exist, so excitons have better access to interfaces with continuous CIS percolation paths to the respective electrode. The agglomerates of CIS in the polymer matrix seem to grow with higher CIS content; accordingly extending the polymer phase. This bears the risk of exceeding the exciton diffusion length and therefore increasing the chance for

recombination before the excitons are dissociated. The resulting charge separation characteristics of these samples were studied by transient absorption measurements, which will be discussed later. Moreover, as the nanoparticles tend to agglomerate in the polymer matrix, especially at higher nanoparticle loadings, the extraction of the size of single nanoparticles from the TEM-images presented in Figure 3.2 is difficult. However, the nanoparticle size is an important issue, as different sizes of nanoparticles are mostly accompanied by different optical and electronic properties [96]. Thus, a detailed investigation of the CIS agglomerates was conducted using dark field TEM combined with selected area electron diffraction (SAED); resulting micrographs are presented in Figure 3.3. The SAED patterns show diffraction rings, indicating that the nanocrystals in the sample have no preferential order and the diffraction pattern is in good agreement with reference data for chalcopyrite CIS (PDF 27-159). There are no distinct differences observable in the SAED patterns, which allows drawing the conclusion that the nanoparticles in the three samples have the same crystallinity and crystal structure. The dark field TEM images in Figure 3.3 were made using only one single reflection to image only selected nanoparticles with a specific orientation of the crystallite, which appear brighter in the micrograph. This method allows identifying single nanocrystals even in agglomerated areas. The respective dark field TEM images clearly show that in each sample the single nanoparticles have sizes of about 3 nm and that the nanoparticle sizes are independent from the polymer:CIS ratio. Thus, the charge carrier mobility of the CIS-phase can principally be assumed equal in all devices. For the sake of comparability, we assumed no charge carrier mobility change in the polymer phase as well. Furthermore, TEM-EDX (energy

dispersive X-ray) measurements were conducted to analyse the chemical composition of the formed CIS nanoparticles. The EDX spectra revealed the same copper:indium molar ratio of 1:1.6 for the three investigated samples (1:3, 1:9, 1:15 (w:w)). This copper:indium ratio was chosen deliberately, as a surplus of indium leads to n-type CIS [80], which is necessary for well performing polymer:CIS hybrid solar cells [93, 109].
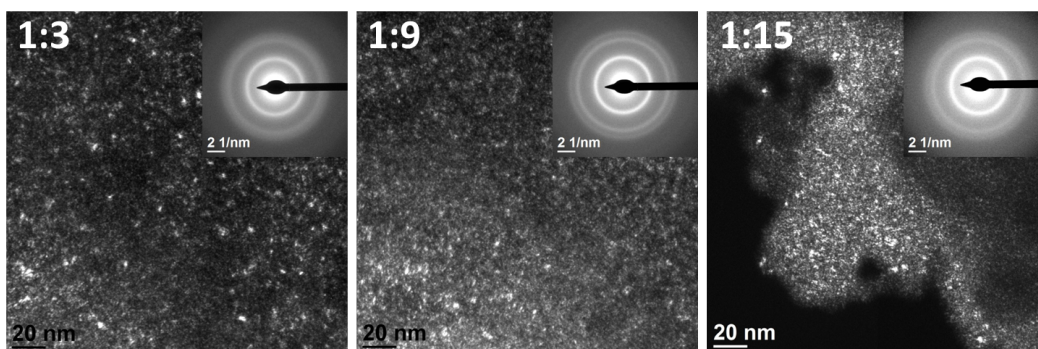

Figure 3.3.: Dark field TEM images of hybrid solar layers with different PSiF-DBT:CIS weight ratios using a specific reflection for imaging. The insets show the respective SAED patterns.

In a further step, PSiF-DBT hybrid solar cells were prepared with all 5 different polymer:nanoparticle ratios (1:3, 1:6, 1:9, 1:12, 1:15 (w:w)) using the simple device architecture glass/ITO/PEDOT:PSS/PSiF-DBT:CIS/Al. The respective solar cell parameters are shown in table 3.1. The thickness of the absorber layers of all the presented solar cells are in the range between 95 and 110 nm to ensure a good comparability of the devices. The exact values are also noted in table 3.1. The solar cells show PCEs of up to 1.7%. The 1:3 device shows a PCE of 0.78% while the PCEs of all the other samples range from 1.5 to 1.7%. The fill factor strongly increases from 1:3 to 1:9, and decreases slightly with higher acceptor loadings. The open circuit voltage (V_{OC}) is actually supposed to show

slightly decreasing behaviour; the prepared devices exhibit V_{OC} values ranging from 400 to 470 mV.

	Layer thickness (nm)	V_{OC} (mV)	J_{SC} mA cm^{-2}	FF %	PCE %
1:3	95 ± 5	464 ± 9	5.73 ± 0.17	29.1 ± 0.2	0.78 ± 0.04
1:6	100 ± 5	427 ± 3	8.69 ± 0.27	44.9 ± 2.6	1.66 ± 0.06
1:9	110 ± 5	414 ± 5	7.62 ± 0.22	52.7 ± 1.3	1.66 ± 0.05
1:12	110 ± 5	470 ± 8	6.81 ± 0.52	47.3 ± 3.6	1.50 ± 0.06
1:15	100 ± 5	399 ± 14	8.45 ± 0.75	48.6 ± 4.6	1.64 ± 0.24

Table 3.1.: Averaged solar cell parameters for different polymer:inorganic weight ratios on the basis of 10 solar cells from one device with equal layer thicknesses.

The short circuit currents (I_{SC}) of the solar cells in this series do not show a recognizable trend. The I_{SC} of the 1:3 device (5.73 mA cm^{-2}) is the lowest in this series, while the values for the other solar cells lie in the range between 6.8 and 8.7 mA cm^{-2}. A possible explanation for this behaviour could originate from the interplay of charge carrier generation and charge carrier transport in the absorber layer. At a first glance, a balanced volumetric ratio (corresponding to a w:w ratio of about 1:4.3) offers the highest probability for well distributed interfaces and thus high interfacial area. However, taking into account that agglomeration of the CIS particles to bigger units in the hybrid layers additionally facilitates the generation of long-lived charges and reduces their recombination probability by offering the electrons the possibility to move away from the dissociation sites [95], the optimum polymer:nanoparticle volume ratio for most efficient charge separation is expected to show a surplus of CIS phase.

Transient absorption measurements were performed to determine the efficiency of carrier generation in the polymer:CIS nanocomposite films. Details
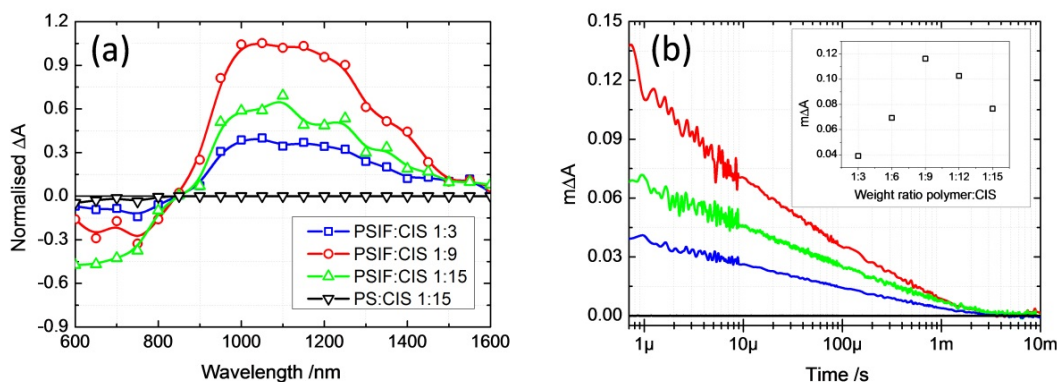
Figure 3.4.: (a) Transient absorption spectra at 10 µs after excitation at 510 nm of PSiF-DBT:CIS layers with different polymer:CIS weight ratios (1:3, 1:9, 1:15, and the control sample polystyrene:CIS 1:15). (b) Transient kinetics of the same films recorded at 1100 nm following excitation at 510 nm. The inset shows the signal size at 1 µs for all PSiF-DBT:CIS weight ratios which have been omitted from the other graphs for clarity.

of our transient absorption spectrometer have been published previously [110, 111]. Figure 3.4 shows the transient absorption spectra and corresponding transient kinetics for the different PSiF-DBT:CIS samples. The transient spectra presented in Figure 3.4(a) were obtained at 10 µs following pulsed laser excitation at 510 nm. The optical excitation of the three PSiF-DBT:CIS samples results in the appearance of broad transient absorption bands centred at approximately 1100 nm, and are similar in shape for all samples. These transient absorption bands may be attributed to photogenerated electrons and holes in the CIS and PSiF-DBT, respectively, since such a feature is absent in both the polystyrene:CIS control sample and the pristine PSiF-DBT layer [93]. The recombination kinetics presented in Figure 3.4(b) reveal that the generated charges have similar lifetimes in all three samples. The inset shows the signal magnitude against the polymer:CIS weight ratio, and reveals that the charge carrier generation is most efficient in the 1:9 sample (corresponding to

a polymer:CIS volume ratio of approximately 1:2), corroborating our previous conclusions [93]. The magnitude of the transient absorption signal (change in optical density, ΔOD) is related to the yield of long-lived charges. Moreover, the decrease in the magnitude of ΔOD is slightly faster at lower CIS ratios, supporting previous work which suggests that a partly agglomerated inorganic phase facilitates the generation of long-lived charges [95]. To connect the structural analysis and the optical properties of the blend layers to the electrical characteristics of the solar cells, simulations were performed. The goal of these simulations is to gain qualitative insight inasmuch photon absorption, charge carrier generation, and charge percolation in the blend layer affect the device performance as a function of the blend ratio.

The structure of the simulated blend layers is generated such that it encompasses as many as possible distinct morphologies due to a given blend ratio; representative cross-sections of the corresponding slabs are shown in figure 3.5. The inspection of the such generated slabs reveals that he largest interface between the polymer phase (shown in green) and the CIS phase (blue) is adopted for the weight ratio 1:3, *i.e.*, for a ratio slightly below volumetrically balanced. With increasing CIS admixture, agglomerates increase in number and size and an increasing number of pathways is formed, which are directly connecting (i) any CIS particle with the Al cathode (yellow) and (ii) the anode (red) with the cathode. The latter can be seen in the cross-section corresponding to weight ratio 1:15 in Figure 3.5.

The fraction of absorbed photons per incident photons for normal incidence as a function of the blend ratio is shown in Figure 3.6. The locally resolved den-
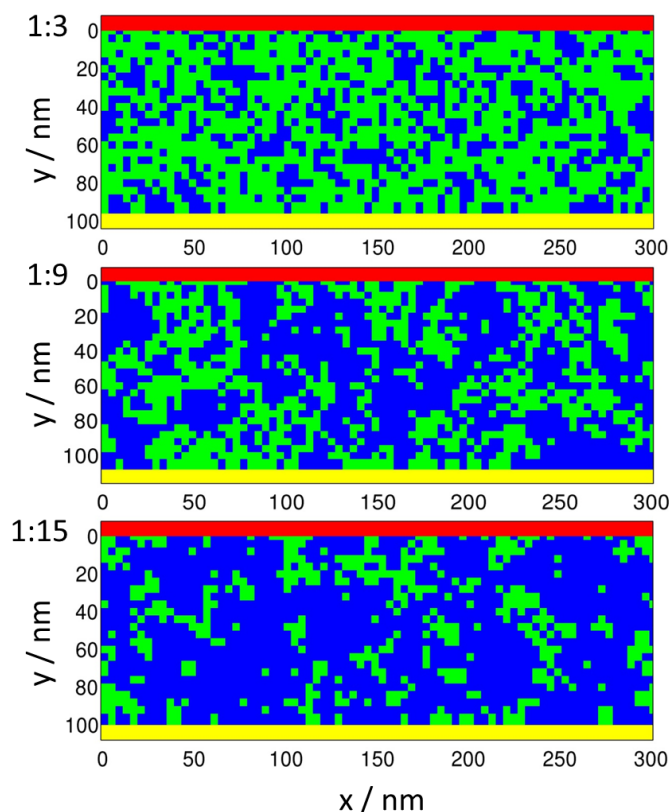
Figure 3.5.: Cross sections through the simulated slabs for the polymer:CIS blend weight ratios 1:3, 1:9, and 1:15 with CIS (blue) , polymer (green), the Al cathode (yellow), and the PEDOT:PSS anode (red).

sity of absorbed photons and the distribution of the optical field are given in the Supplementary Data. Remarkably, only 40% of the incident photons or less are absorbed within the semiconducting layer (open diamonds). The number of absorbed photons markedly decreases with increasing CIS content. While the blend harvests almost as many photons as the pristine polymer layer for the ratio 1:3, ca. 31% of the incident photons are available for charge generation in the 1:15 blend. The apparent recovery of absorption in going from 1:6 to 1:9 is due to the 10 nm thicker blend layer in the 1:9 device. To further elucidate which fraction of absorbed photons are going to contribute to charge
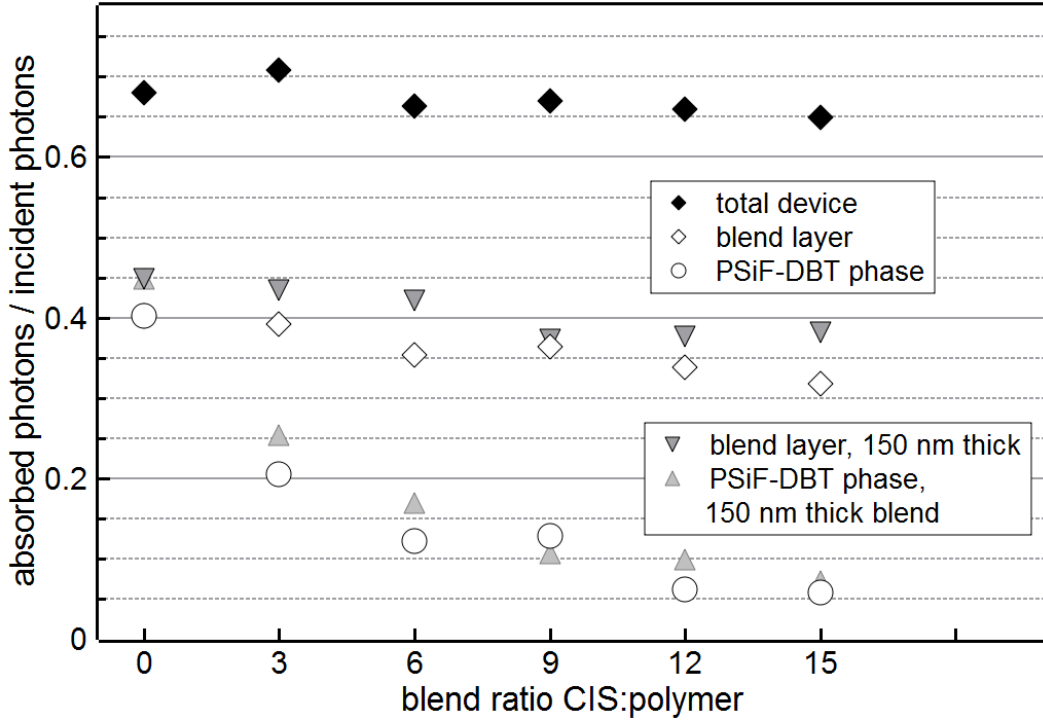
Figure 3.6.: Ratio of the absorbed to incident photon density for devices with different blend weight ratios and a pristine PSiF-DBT layer; shown is the ratio for absorption in the entire device (filled diamonds), in the absorber layer (open diamonds), and in the PSiF-DBT phase (circles). Additionally, this ratio corresponding to the absorber layer (downward triangles) and the PSiF-DBT phase (upward triangles) in hypothetical devices with 150 nm thick blend layers but otherwise same layer sequence.

carrier generation, the density of photons absorbed within the polymer phase, *i.e.*, the photons needed to generate mobile excitons, are shown (circles). While the polymer and the CIS fraction absorb approximately the same fraction of photons in the 1:3 device, the contribution of the polymer in comparison to CIS reduces to a third for 1:6 and 1:9 and even to less than 20% for the largest blend ratios. Remarkably, in the 1:6 and 1:9 devices a similar exciton density is generated due to a comparable density of absorbed photons, while transient absorption measurements detect that the concentration of interface excitons being able to dissociate into mobile charge carriers in the 1:9 blend is at least

twice as large as in the 1:6 blend (Figure 3.4). To ensure a valid comparison between the simulations and photon-induced absorption experiments, the absorbed photon density is also computed for devices containing absorber layers as thick as the films used for the transient absorption measurements (150 nm). The overall trend for such thicker films (triangles in Figure 3.6) resembles the trend from the devices of table 3.1. Thus, the amount of generated charges is given, at least to a large extent, by the size of the interface area rather than being simply determined by the number of initially absorbed photons.

Quantity		Parameters to describe exp. data	Idealized parameters
Electron transport level offset (eV)	ΔE_e	0.23	0.2
Hole transport level offset (eV)	ΔE_p	0.16	0.2
Built-in voltage (V)	V_{bi}	0.5	0.7
Work function PEDOT:PSS (eV)		4.60	4.80
Work function Al (eV)		4.10	4.10
Dielectric constant polymer	$\epsilon_{r,p}$	3.0	3.0
Dielectric constant CIS	$\epsilon_{r,CIS}$	8.5	8.5
Electron mobilities ($m^2V^{-1}s^{-1}$)	μ_e^P	10^{-9}	10^{-9}
	μ_e^{CIS}	10^{-7}	10^{-7}
Hole mobilities ($m^2V^{-1}s^{-1}$)	μ_h^P	4×10^{-8}	4×10^{-8}
	μ_h^{CIS}	4×10^{-8}	4×10^{-8}

Table 3.2.: Values of the parameters used in the simulations.

In a next step, the actual I-V characteristics of the devices are computed to discriminate between the impact of charge carrier generation and percolation. The parameters entering the simulations discussed below are collected in table 3.2. The electrons and holes are assumed to adopt averaged mobilities in the polymer and in the CIS-domains, where the mobility values are constants and, thus, independent of the domain sizes. The mobility values are chosen such that the currents at forward bias (for biases exceeding V_{OC}) match the
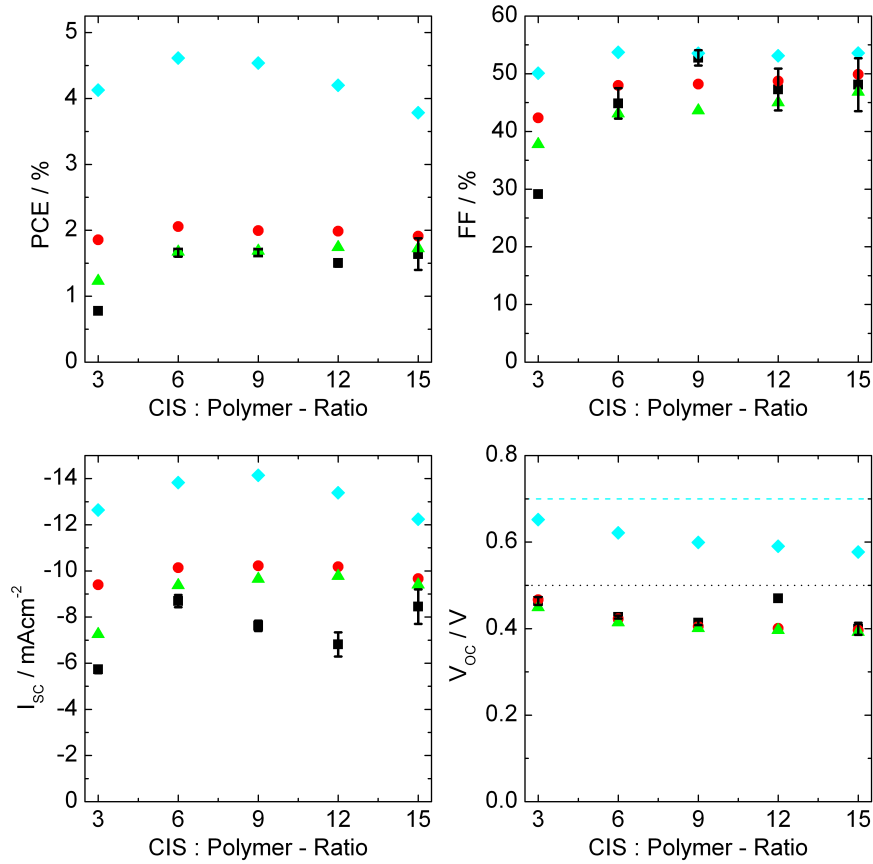
experimental curves.

Figure 3.7.: Comparison of the power conversion efficiency, fill factor, short-circuit current (I_{SC}), and open- circuit voltage (V_{OC}) extracted from experiments (black squares) with the corresponding parameters from the simulations (red circles), including additional trapping (green upward triangles), and for simulations using idealized parameters (cyan diamonds). Lower right panel: The built-in voltage V_{bi} of 0.5 V for the devices corresponding to experiment is indicated with a dotted line and $V_{bi} = 0.7$ V for idealized devices with a dashed line.

Figure 3.7 displays the figures-of-merit of the simulated I-V curves based on these parameters and the slabs shown in figure 3.5 in comparison to the experimental data (black squares). We convinced ourselves that the such simulated results can be used to gain a deeper qualitative understanding of the observed trends: Extensive tests using (i) mobility values varying by orders of magnitude

from those in table 3.2 and (ii) multiple slab geometries being independently generated for any given blend ratio yielded figures of merit that, albeit being quantitatively different, revealed the same trend as a function of the blend ratio. Moreover, all test calculations univocally predicted the same characteristic evolution of the shape of the I-V curves; this was true also when slabs with fully randomized positions of polymer and CIS-related voxels were considered. The quantitative differences in the figures-of-merit are due to a varying number of closed pathways and an additional preference of certain pathways due to enlarged mobilities (*vide infra*). The simulations corroborate the experimental finding that a volumetric ratio exceeding 1:1 (weight ratio above 1:4.3) is favourable to achieve higher photocurrents. Considering the similar I_{SC} values for polymer:nanoparticle ratios from 1:6 (w:w) to higher CIS loadings in combination with the results from the transient absorption measurements a considerable contribution of the CIS-phase to effective charge generation can be observed. This is supported by the decreasing absorption of the polymer phase and thus complementary high absorption in the CIS phase, as illustrated in Figure 3.6. Prior discussing the obtained trends in the parameters of the simulated curves in detail, it appears to be beneficial to discuss the evolution of the shape of the I-V curves. In Figure 3.8A, the positions of the transport levels of PSiF-DBT and CIS in the device are indicated. Panel B of Figure 3.8 shows the I-V curves for the blend-ratios 1:3 and 1:12 (w:w), as these two curves reflect the characteristic behaviour found in all simulations. At CIS loadings as small as 1:3 (circles), the open circuit voltage approaches the built-in voltage of 0.5 eV that is determined by the difference of the electrode work functions (cf. table 3.2 and Figure 3.8A).
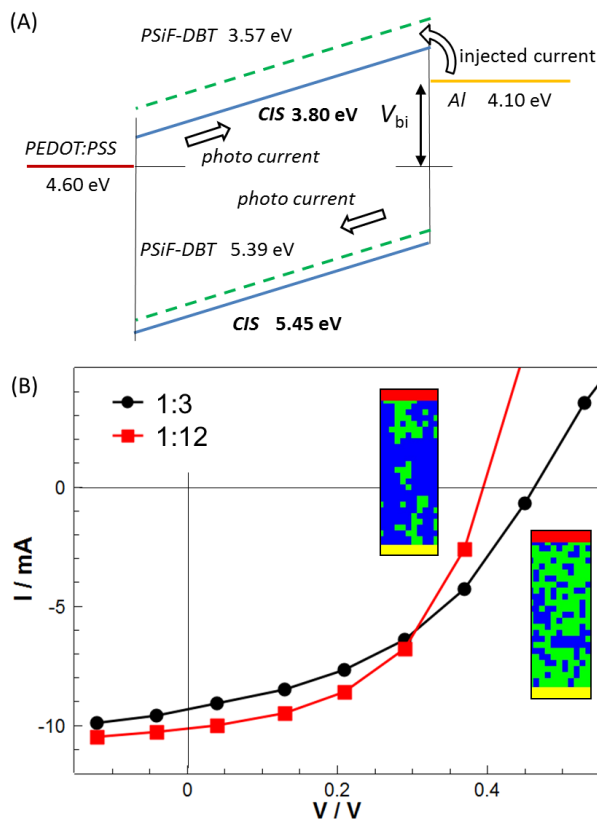
Figure 3.8.: (A) Schematical representation of transport level positions in the ITO/PEDOT:PSS/absorber layer/Al layer structure used in the simulations of the measured devices; here, shown for an external bias near open circuit. (B) Simulated I-V characteristics for the blend ratios 1:3 and 1:12 (w:w) using the parameters in table 3.2. The insets show an excerpt of the corresponding morphology (green: polymer content, blue: CIS content in the absorbing layer, red: PEDOT:PSS, yellow: Al).

The photo-generated mobile electrons, on the other hand, find only few closed pathways from the position of generation to the Al electrode; thus, the short circuit current remains smaller than what may have been expected from the efficiency of charge carrier generation. Increasing the CIS fraction in the blend leads to a more tightly-knit network of CIS clusters. Thus, the percolation of photo-generated electrons improves. Correspondingly, I_{SC} increases as can be

seen from the I-V curve of the 1:12 blend (squares). This is consistent with the finding that a volume fraction exceeding 50% (blend weight ratio 1:6 or higher) is needed to achieve an appreciable current (Figure 3.7, circles). The smaller I_{SC} values for the ratios 1:12 and 1:15 are, at least in part, explained by the smaller amount of photons absorbed in the corresponding devices (cf. Figure 3.6, diamonds). However, increasing the volume fraction of CIS also enables efficient percolation for "dark" electrons injected from the Al cathode due to the completion of pathways connecting the cathode with the anode through the active layer (Figure 3.8A, inset Figure 3.8B). Thus, the turn-on bias of the dark current shifts to lower voltages and the net current observed for biases approaching the built-in voltage is already determined by the injected "dark" current (Figure 3.8B, squares).

As a result, V_{OC} is markedly smaller than the built-in voltage; in fact, it steadily reduces with increasing CIS volume fraction (Figure 3.7, circles). Due to the larger electron mobility in the CIS phase, the slope of the I-V characteristic near V_{OC} increases and gives rise to improved fill factors (Figure 3.8b, squares). The trend in the overall power conversion efficiency is most strongly influenced by the dependence of I_{SC} on the blend ratio. An additional consideration of carrier trapping within the polymer discloses the same overall trend, but yields a better quantitative agreement of the simulated curves with the experimental ones (triangles in Figure 3.7). Since the morphology due to a particular blend ratio essentially determines the ability of the electrons to traverse the device, there is always a trade-off between efficient harvesting of photocurrent (large fraction of CIS) and preventing the flow of the dark electron current (small fraction of CIS). Hence, fill factor, open-circuit voltage, and short-circuit cur-

rent adopt their maximum independent from each other and cannot be simultaneously optimized by altering the blend ratio. A balanced hole and electron percolation is, therefore, a crucial prerequisite to improve the devices. A hypothetical, idealized system (table 3.2, right column) containing a thicker blend layer (150 nm) for improved absorption and possessing equal hole and electron transport level offsets and an enlarged V_{bi} (0.7 eV) exhibits indeed substantially larger I_{SC} and efficiencies (Figure 3.7, diamonds) while qualitatively preserving the dependence of the solar cell parameters on the blend ratio.

3.4. Conclusion

Experimental data as well as the results from simulations yielded interesting insights in charge generation and transfer in *in situ* prepared hybrid solar cells. Thorough investigation of the influence of a variation of the polymer:nanoparticle ratio on the morphology of the absorber layer as well as on charge carrier generation disclosed the following findings:

- the nanocrystal size is the same in all samples independent from the polymer:nanoparticle ratio

- the nanoparticle agglomerates enlarge with increasing nanoparticle concentration

- a clear maximum of charges generated in the polymer phase is found at a polymer:nanoparticle weight ratio of 1:9 corresponding to a volume ratio of about 1:2, even though the absorption of the polymer exhibits only

intermediate values compared to higher polymer loadings, indicating a beneficial donor:acceptor interfacial area at this ratio

- the marked trend in the charge generation maximum due to exciton dissociation is neither reflected in the short-circuit current density of the prepared solar cells nor in any of the simulations - starting from a polymer:CIS weight ratio of 1:6 the I_{SC} does not change significantly with higher CIS loadings

The interplay of polymer and CIS regarding absorption, charge generation, and percolation sums up to a complicated relationship. The crucial solar cell parameters (I_{SC}, V_{OC}, FF) exhibit characteristic trends independent from each other and thus, solely by altering the blend ratio a concerted optimisation is not possible. Charge generation stemming from the polymer necessitates a large interface for exciton dissociation. Increasing the CIS ratio enlarges the interface facilitating both the charge generation probability and electron transport to the respective electrode. Additionally, CIS itself is a photoactive semiconductor and, therefore, contributes to the generation of charges leading to additional photocurrent. At a certain surplus of CIS, continuous pathways between anode and cathode are formed. These pathways support charge carrier injection at both electrodes, which has the detrimental effect of reducing the open circuit voltage through "dark" electron currents. The simulations were able to replicate the trends revealed by experimental data rather well, allowing to gain deeper insights into the correlations between morphology, charge generation, and solar cell characteristics. Furthermore, they provide an example of what could be possible by slight adjustment of electron and hole transport level off-

sets and built-in voltage, which could be realised through chemical tailoring and material optimisation. Additionally, by introduction of suitable interlayers, the significant dark current, especially in the devices with higher CIS content, should be reduced.

3.5. Supplementary Data

Contributions from simulation methodology: Generation of the morphology related to a given blend ratio: Initially, all mesh cells in the active layer were assigned to the polymer; to mimic the experimentally determined nanoparticle diameters 3 nm (*vide supra*), 8 (=2x2x2) adjacent voxels were jointly treated as "particles". The original polymer particles were successively replaced by CIS nanoparticles until the desired blend ratio was reached: A particle a randomly chosen position was converted to CIS if more than 8 of the 18 neighbouring particles (facet and edge) were inorganic already. Otherwise, the particle is converted with a probability of 5%.

Absorption profile: The photon flux absorbed in the active layer is determined using the optical electric field distribution and the complex indices of refraction

PSiF-DBT   HOMO-LUMO Levels

Precursors
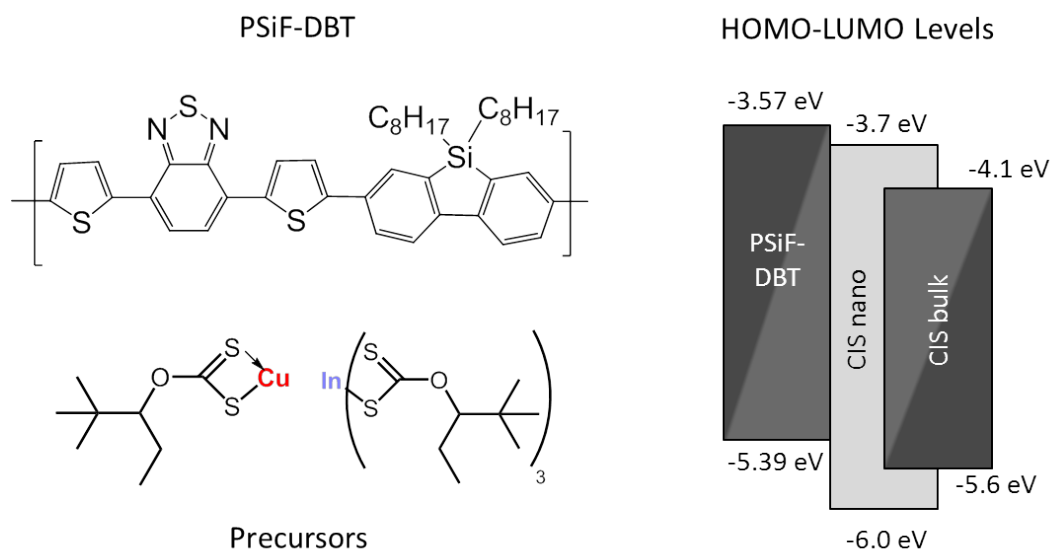
Figure 3.9.: Chemical structure of PSiF-DBT and Cu- and In-xanthates as well as the respective HOMO and LUMO levels (in case of CIS both levels of bulk and nanoparticular CIS are given, as reported in [82].

following the adaption of the transfer matrix method described in [106]. The model slab used for the optical simulations contains the active layer (generated as described above) that is sandwiched between glass, ITO, and PEDOT:PSS layers and the Al layer. For each voxel in a stack of voxels in y-direction (Figure 3.10), the transfer and transition matrices are computed and the dissipation function determined for a spectral power density corresponding to the AM1.5 solar spectrum. This dissipation functions are averaged for all stacks of the slab. To obtain the photon density, the averaged dissipation function is divided by the corresponding photon energy for each wavelength. After integration of the photon density over the spectral range corresponding to the solar spectrum AM1.5, the overall number of photons absorbed in a given depth of the device is obtained. The total number of absorbed photons is then calculated by

further integrating along the extension of the model slab. The complex indices of refraction $\tilde{n}$ = n + iκ for Al, glass, and ITO were taken from [112] and for PEDOT:PSS from [113]. The index of refraction, n, of CIS is taken from [114] and used to extract the imaginary part from the absorption spectrum. For the polymer PSiF-DBT, a constant n=1.8 was assumed and κ extracted from the absorption spectrum.
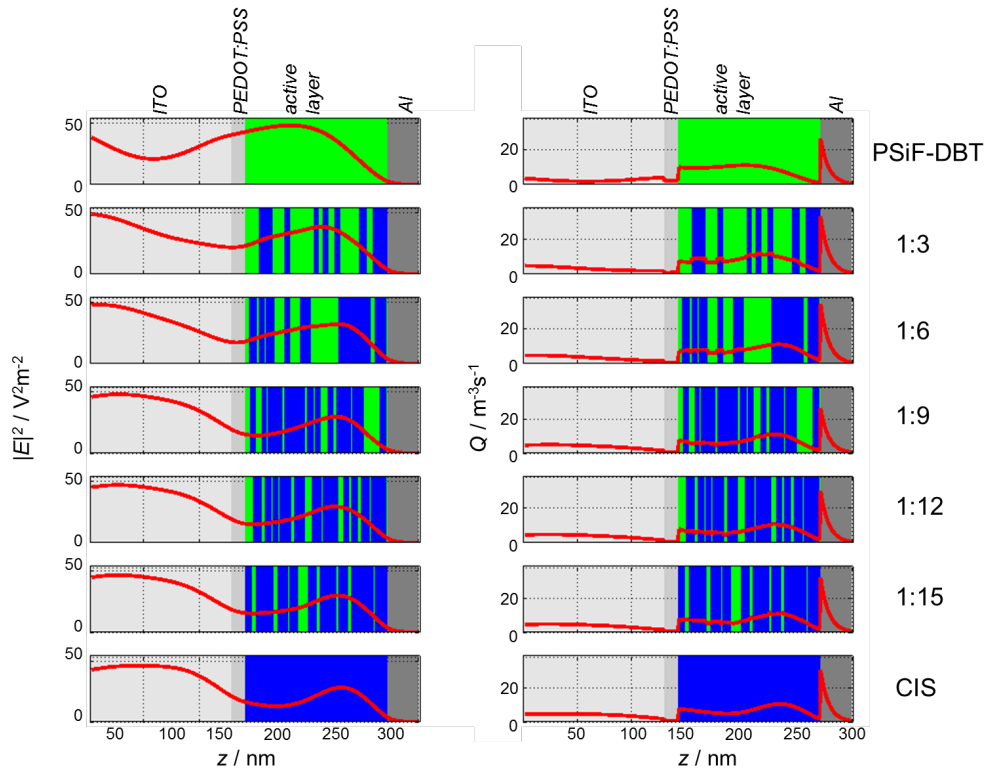
Figure 3.10.: Distribution of the strength of the optical electric field squared (left) and density of photons absorbed per second, Q, (right) for a cross-section of the device for pristine PSiF-DBT and CIS semiconducting layers and blend layers with the PSiF:CIS ratios 1:3, 1:6, 1:9, 1:12, and 1:15. As a guide to the eye, the morphology of the blend layers is represented by the polymer-CIS arrangement of a selected stack; the polymer is indicated with green, the CIS phase is shown in blue.
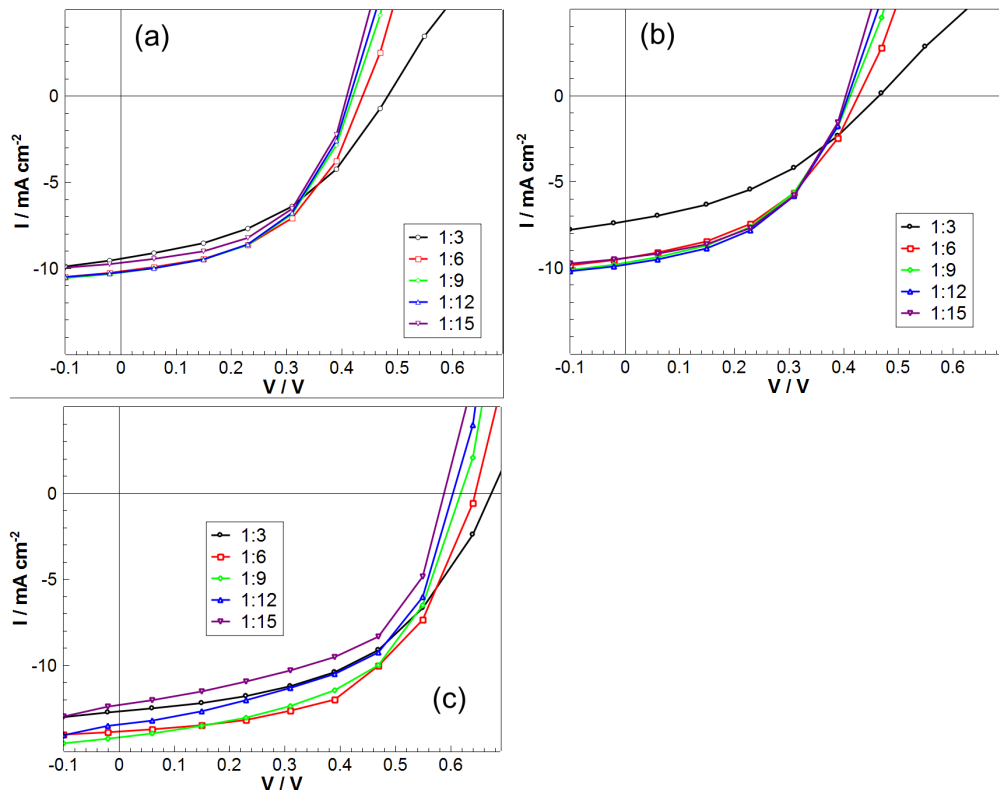
Figure 3.11.: Simulated I-V characteristics using the parameters as stated in table 3.2 of the manuscript. The characteristic solar cell parameters extracted from these curves are depicted in figure 3.7. (a) I-V curves in correspondence with the devices built (center column in table 3.2), (b) as in (a) with consideration of charge carrier trapping in the polymer phase, and (c) simulated I-V curves of the idealized device (right column in table 3.2).
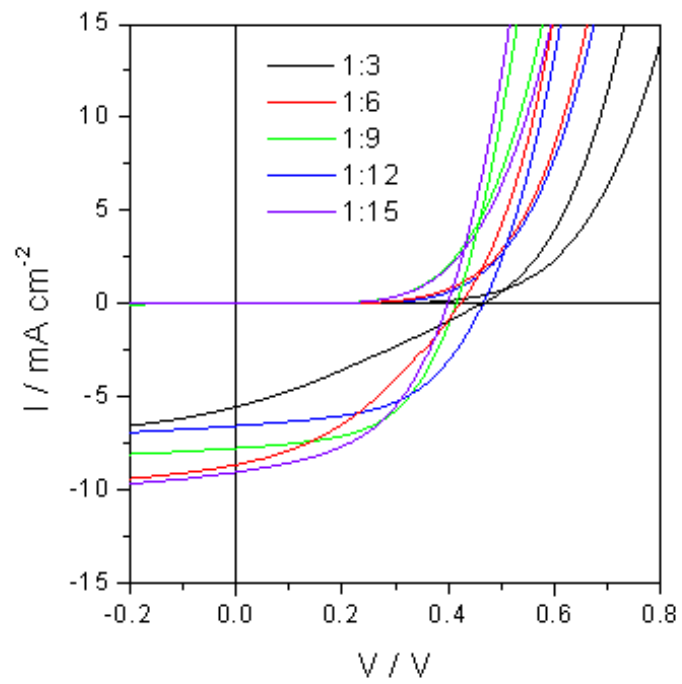
Figure 3.12.: Typical current density-voltage characteristics of experimentally measured hybrid solar cells with different polymer:CIS weight ratios.

4. Polystyrene:CIS solar cells

"Science cannot solve the ultimate mystery of nature. And that is because, in the last analysis, we ourselves are part of nature and therefore part of the mystery that we are trying to solve."

Max Planck (1932) [115]

4.1. Introduction

One of the main reasons for choosing copper indium sulfide as acceptor material is its absorption capability, resulting in enhanced photocurrent generation. Charge carrier generation resulting from excitons generated in the polymer have already been discussed in Chapters 2 and 3. Copper indium sulfide by itself should also be able to generate charge carriers, as is easily deducible from all-inorganic $CuInS_2$ solar cells (*e.g.*, reviewed in [80]). Typically, it has been used in its crystalline form, so a direct knowledge transfer to nanoparticular $CuInS_2$ is probably not reasonable.

In our studies, we use CIS with a surplus of indium to provide an n-type phase, which is necessary for PSiF-DBT:CIS hybrid solar cells to work properly.[93, 109] To determine whether, and if so, to what extent the n-CIS contributes to the hybrid solar cells by itself (*i.e.*, without excitons from the polymer), the photoactive PSiF-DBT was replaced by polystyrene (PS). In this setup, PS serves as an optically transparent, electrically insulating filler material to provide an absorber layer similar to that of standard hybrid PSiF-DBT:CIS solar cells. A similar approach has been reported by Chaudhuri et al., where lead sulfide (PbS) nanoparticles were prepared from solution by *in situ* thermolysis in a PS matrix.[116]

Initially, ultraviolet-visible spectrophotometry (UV-Vis) measurements were conducted to ensure that introducing the polymer filler does not interfere with the optical characteristics of CIS nanoparticles. An array of PS:CIS solar cells with several polymer:inorganic mass ratios has been prepared, investigated by means of transmission electron microscopy (TEM) and compared

with nanocomposite PSiF-DBT:CIS solar cells in terms of J-V characteristics. The absence of a donor polymer shifts the focus of interest to the other interfaces of the absorber layer. Similar approaches are few and far between in scientific literature; Arici, Sariciftci, and Meissner [82] have investigated stoichiometric (*i.e.*, undoped) CIS nanoparticles as pure layer on PEDOT:PSS as well as embedded in a highly p-doped PEDOT:PSS layer. Motoyoshi et al. [117] have fabricated and characterized bilayers of p-type CIS and n-type TiO_2 (electrodes: FTO and Al). Their study resembles the below-mentioned investigation rather than that of Arici, Sariciftci, and Meissner. However, neither group was able to fabricate solar cells with noteworthy photovoltaic parameters.

In this part of my work, I want to present the ability to produce working PS:CIS solar cells. On that basis, the aim of this section is to enlighten the standalone features of n-type CIS nanoparticles embedded in a polymer matrix.

4.2. Experimental

PEDOT:PSS layers (Clevios P VP.AI 4083, Heraeus) were spin-coated from solution using deionized water (1:1, vol.) on glass/ITO substrates (Xin Yan Technology Ltd., R_S = 10 Ω/sq, sonicated in deionized water and isopropanol, O_2 plasma cleaned (FEMTO, Diener electronic)) and thermally dried in nitrogen atmosphere (150 °C, 15 min). PS:CIS layers were thereon prepared by doctor blading of a chlorobenzene solution containing copper xanthates, indium xanthates (copper and indium *O*-2,2-dimethylpentan-3-yl dithiocarbonate) [93], and PS and subsequent thermal treatment on a programmable heating plate (CAT MCS66, varying temperature programmes, *vide supra*) in nitrogen

atmosphere. Different mass ratios were chosen to establish comparability to PSiF-DBT:CIS solar cells. Aluminum and silver electrodes and interlayers were deposited using a thermal evaporation chamber mounted inside a glovebox system (LABmaster dp, MBRAUN Glovebox Technology, Germany) at a base pressure of 8×10^{-6} mbar (nitrogen atmosphere). Evaporation rates: AgAl electrode: Ag 0.1 Å s^{-1}, Al 0.1 Å s^{-1} for the first 10 nm, then 10 Å s^{-1}; pure Ag or Al electrodes: 0.1 Å s^{-1} for the first 10 nm, then 10 Ås^{-1}. Current density-voltage (J-V) curves were recorded using a Keithley 2400 SourceMeter and custom-made Lab-View software. The solar cells were illuminated using a Dedolight DLH400D (used in conjunction with Dedolight DEB400D electronic ballast). The intensity of the incoming light was set to 100 mW cm^{-2} providing a spectrum quite similar to AM1.5G (determined using a KippZonen-CMP-11 pyranometer, no spectral mismatch was considered). The effective device area (0.04 cm^2) was defined by shadow masks applied to the solar cells. Layer thicknesses were specified on a DektakXT surface profiler (Bruker). UV-Vis spectra were recorded using a Lambda 35 spectrometer equipped with an integrating sphere (PerkinElmer). Samples for TEM analyses were spin-coated from solution on a NaCl substrate and thermally treated as stated above. The substrate was then dissolved in deionized water. The remaining film was again washed in deionized water and applied to a TEM grid. TEM analyses were conducted on a Tecnai F 20 microscope (FEI Company, 200 kV, Schottky emitter) equipped with a high resolution Gatan Imaging Filter (GIF), an UltraScanCCD camera and a Fischione HAADF STEM detector.

4.3. Results and Discussion

As a first step, TEM analyses of a thin, pure CIS layer were conducted to determine, if using PS affects the *in situ* formation of CIS nanoparticles.
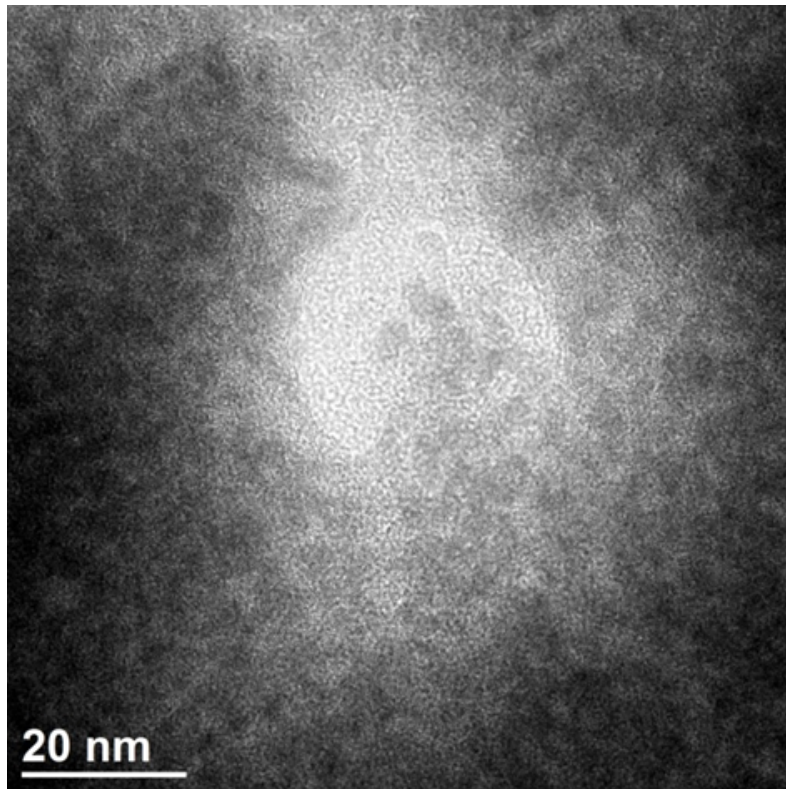
Figure 4.1.: Bright field TEM image of a PS:CIS layer (recorded by W. Haas).

Fig. 4.1 shows a bright-field TEM image of a PS:CIS sample. At the center of the image distinctly outlined nanoparticles are revealed; these nanoparticles have a size of about 3 to 5 nm, which is in good agreement to former analyses that have been conducted in PSiF-DBT:CIS hybrid solar cells (see Sec. 3.2). Hence, this is a clear evidence for equivalent nanoparticle formation.

Thin layers of PS hardly exhibit considerable absorbance in the visible regime;
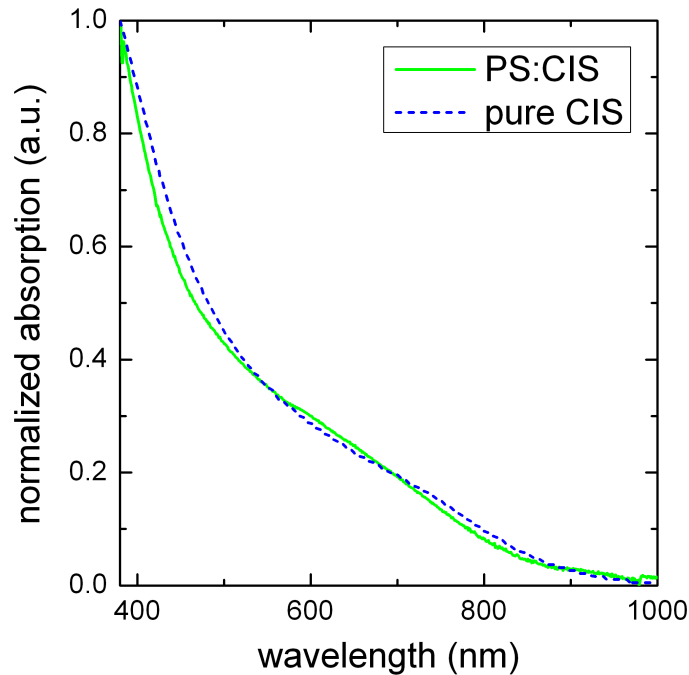
Figure 4.2.: Comparison of normalized absorption spectra of a pure CIS layer and a PS:CIS blend (mass ratio 1:9).

nonetheless, a different arrangement of nanoparticles might result in different optical parameters. Therefore, a second step included UV-Vis measurements of PS:CIS samples to compare the results with absorption spectra of pure CIS nanoparticle layers.

Inside the polymer matrix the effective absorption layer thickness can only be approximated. So, to provide a convenient way of comparing the absorption spectra, the absorption was normalized in the regime from 380 to 1000 nm (below 380 nm the influences of PS and glass substrate are interfering).

Albeit these two results of course are no proof that optical and electronic behaviour of CIS is equal in both PS and PSiF-DBT, it is still a solid foundation

to work with.

Based on this fundament, a series of glass/ITO/PEDOT:PSS/PS:CIS/Al solar cells with differing polymer:inorganic ratios has been prepared. Focus was set on preparation of solar cells with similar layer thicknesses, which were found to be in the range of 90 to 100 nm. The resulting characteristic parameters are summarized in Tab. 4.1. The V_{OC} values are in the range of 400 to 420 mV, thus, roughly comparable to the hybrid solar cells with PSiF-DBT as photoactive counterpart (cf. Sec. 3.3). The same is true for the fill factor: obviously, a mass ratio of 1:3 results in the lowest value, increasing the amount of CIS to 1:9 and beyond substantially enhances this parameter.

	V_{OC} (mV)	J_{SC} mA cm^{-2}	FF %	PCE %
1:3	425 ± 15	2.76 ± 0.06	30.7 ± 0.5	0.36 ± 0.02
1:9	401 ± 27	3.45 ± 0.21	44.8 ± 1.2	0.62 ± 0.07
1:15	417 ± 16	2.79 ± 0.15	45.9 ± 2.0	0.53 ± 0.06

Table 4.1.: Averaged solar cell parameters for different polymer:inorganic weight ratios on the basis of 5 solar cells each from one device with Al cathode.

In a typical hybrid solar cell, the explanation would be based on the resulting morphology and the (in-)sufficiency of continuous pathways for efficient charge carrier generation and transport. In this absorber layer there is only one electrically active component; so in principal, there are two possible operational mechanisms in this solar cell:

(i) Basically, PEDOT:PSS is a (highly) p-doped semiconductor; therefore, the interface between PEDOT:PSS and CIS could act as p-n heterojunction similar to typical inorganic solar cells. However, due to its strongly doped state PEDOT:PSS is usually claimed to be a conductive polymer; it resembles rather

metallic than semiconductor characteristics. This is also supported by the fact that hardly any values for its HOMO/LUMO levels are reported; instead, as a typical characteristic parameter the work function is given, which clearly indicates the conformity with metallic electrodes.

(ii) As described in Sec. 2.2.1.1 the metal-semiconductor interface at the Al-cathode could form a Schottky-barrier. However, formation of a Schottky barrier depends on the work functions of metal and semiconductor. A metal with lower work function than the Fermi level of the semiconductor would form an ohmic contact, while higher work function metals build up a Schottky barrier.[32] The barriers height equals to the difference between work function (metal) and electron affinity (semiconductor). An exact value for the electron affinity of CIS nanoparticles as used in this work is not known; according to Arici, Sariciftci, and Meissner [82] it ranges from 4.1 to 3.7 eV, Zhong et al. [118] have claimed the conduction band to have its lowest level at about 3.8 eV. The strong doping based on the surplus of indium shifts the Fermi level to a potential close to the conduction band; an approximation to the conduction band itself is probable. Therefore, at nanoparticular CIS-Al surfaces, the work function of Al is always higher than the electron affinity of CIS and, thus, a Schottky barrier is induced. The difference in doping level (the aluminum contact can be seen as heavily doped semiconductor) pushes the entire depletion region onto the CIS-phase.[119]

Additionally, the aforementioned metallic character of PEDOT:PSS requires taking this side of the semiconductor into consideration as well, as it also offers a metal-semiconductor junction. Its high work function would definitely qualify it for a Schottky barrier; however, the built-in field drives the electrons

towards the Al cathode (additionally, Kislyuk et al. [120] have found that PE-DOT:PSS as part of a PEDOT:PSS-CdSe/CdTe Schottky barrier only acts as hole-collecting layer).

Therefore, exciton dissociation would only take place in the depletion region close to the cathode. Though the nanoparticles tend to agglomerate (see 3.3), a fair volumetric fraction has to be occupied by the CIS-phase to provide continuous paths across the whole layer thickness.

A closer look at the J-V curve of a champion solar cell (Fig. 4.3) reveals that, albeit the shunt resistance has room for improvement, the main reason for the relatively low fill factor is based on the serial resistance.
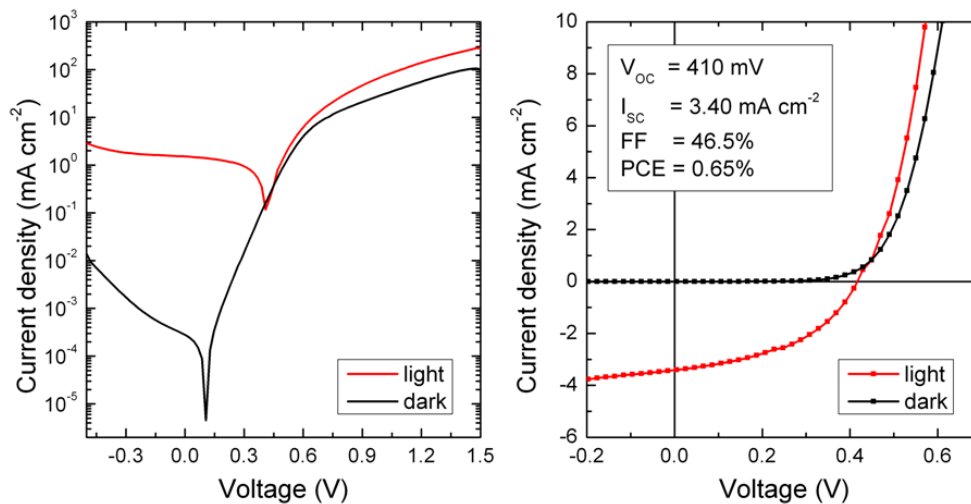
Figure 4.3.: J-V curves of a champion PS:CIS solar cell under illumination and in the dark.

The fill factor hardly changes when increasing the mass ratios from 1:9 to 1:15, while in PSiF-DBT:CIS hybrid solar cells it has a clear maximum at 1:9. In anticipation of findings discussed in a later chapter (Ch. 6), the interface between CIS-phase and cathode seems likely to be a crucial parameter regarding the fill factor. This could also explain the aforementioned result: in hybrid

solar cells holes are transported to the anode through the polymer (besides the CIS-phase, obviously); therefore, hole extraction takes place at the polymer-PEDOT:PSS and CIS-PEDOT:PSS interface, respectively. In PS:CIS solar cells, the sole hole extraction interface is limited to CIS-PEDOT:PSS. Similarly to the obstruction at the CIS-cathode interface an additional resistance might occur at CIS-PEDOT:PSS junctions.
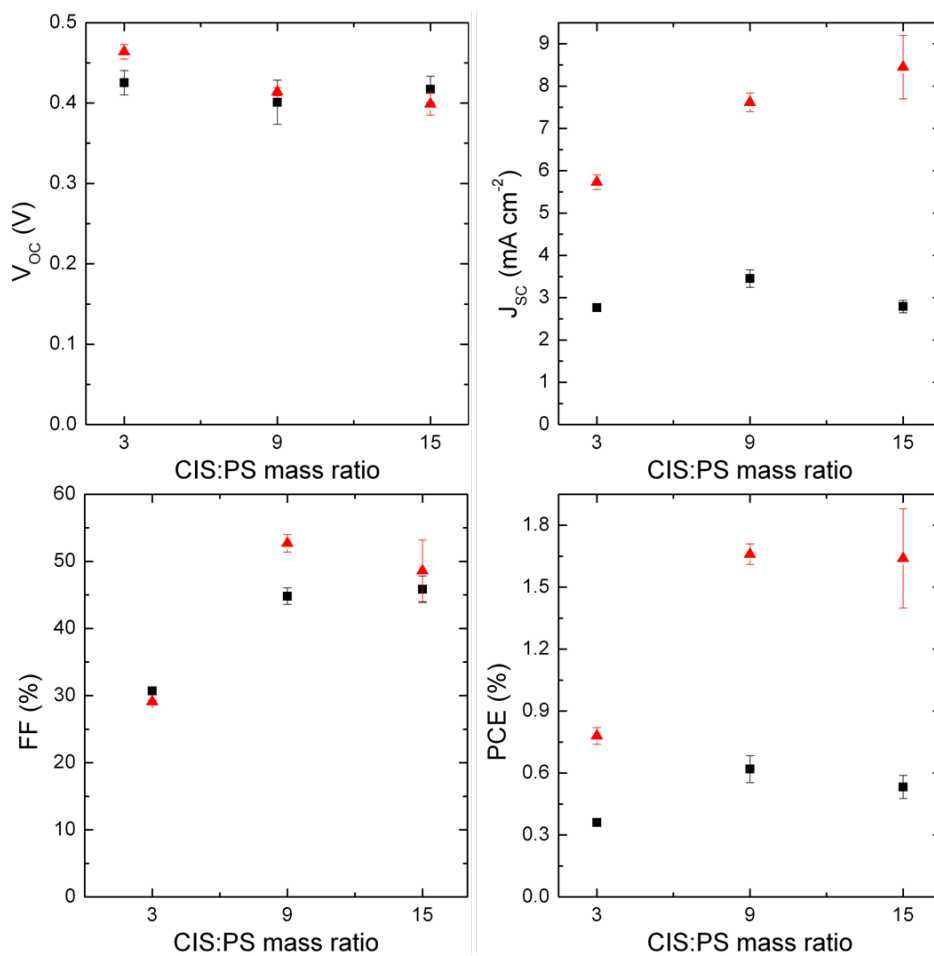
Figure 4.4.: Comparison of characteristic parameters of PS:CIS solar cells (black squares) with PSiF-DBT:CIS hybrid solar cells (red triangles) with different polymer:CIS ratios.

In a general sense, the current density falls prone to the distinctly reduced absorption due to the absence of the conjugating polymer; however, the contribution of the CIS-phase to the current density still is immense. The IPCE measurement depicted in Fig. 4.5 reveals the (advantageous) reason: a conversion of photons to electrons over nearly the whole visible regime.
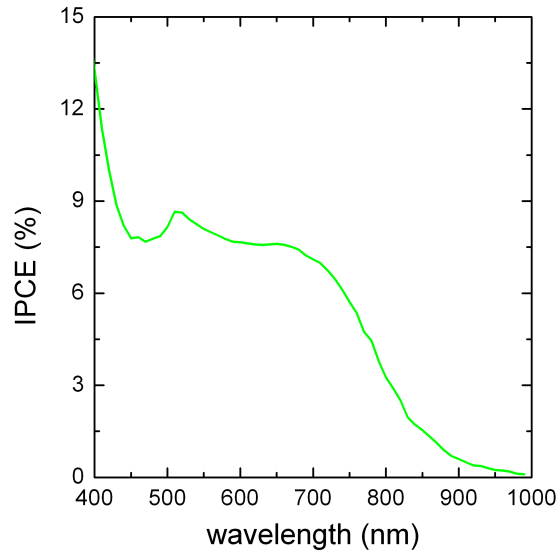
Figure 4.5.: IPCE measurement of a PS:CIS solar cell. To overcome stability issues a silver/aluminum electrode (see Ch. 5) was applied.

A gain in current density is observed when increasing the PS:CIS-ratio from 1:3 to 1:9; this trend was expected as a consequence of enhanced absorption. However, a further CIS-increment does not lead to a higher J_{SC}. The reasons for this behavior could not be enlightened to full satisfaction and are currently under investigation.

A comparison of the characteristic photovoltaic parameters of PS:CIS solar cells with PSiF-DBT:CIS hybrid solar cells (as presented in Ch. 3.3) reveals a solid contribution of the CIS-phase as a single layer solar cell. The V_{OC} and FF values

occur in a similar regime; the short circuit current density provides an output at about 1/3 to 1/4 in a solar cell without the conjugated polymer.

Nonetheless, the single layer solar cell of CIS nanoparticles in a polystyrene matrix performed surprisingly well and opened a wide array of interesting research topics.

4.4. Conclusions

In this work, PS:CIS solar cells with different mass ratios have been prepared to investigate the contribution of the CIS-phase to the overall performance of PSiF-DBT:CIS hybrid solar cells. The CIS nanoparticles have been embedded into a PS matrix to provide a possibility to investigate them in a similar morphology as they occur in hybrid solar cells. Its operational mechanism seems to base on a Schottky barrier between CIS-phase and aluminum cathode. The prepared solar cells exhibited an surprisingly high power conversion efficiency, compared to reports found in the scientific literature. A mediocre fill factor indicates, that the interface between CIS-phase and both electrodes exhibits an unfavorable resistance.

The results found in this part suggest, that the additional contribution of the inorganic phase in hybrid solar cells could be significant. However, more detailed analyses of the charge generation mechanisms are indispensable.

5. Silver-modified Aluminum Electrodes in PSiF-DBT:CIS Solar Cells

"There are two possible outcomes: if the result confirms the hypothesis, then you've made a measurement. If the result is contrary to the hypothesis, then you've made a discovery."

Enrico Fermi

(cited by Jevremovic (2005) [121])

This chapter was published in

The Journal of Physical Chemistry C (ACS Publications):

Comprehensive Investigation of Silver Nanoparticle/Aluminum Electrodes for Copper Indium Sulfide/Polymer Hybrid Solar Cells

Mario Arar, Andreas Pein, Wernfried Haas, Ferdinand Hofer, Kion Norrman, Frederik C. Krebs, Thomas Rath, and Gregor Trimmel

5.1. Introduction

Polymer based solar cells are on the brink of success as their assets are well known (lightweight, flexible, readily processable) and their major flaws of low efficiency [122] and stability [123] are waning due to soaring scientific interest and, subsequently, steady progress. Currently, electroactive polymers combined with fullerene derivatives are most prominent and leading with respect to power conversion efficiencies (PCE), as they are rapidly approaching 10% [124] (presently certified: 8.37% [125], 9% [126]) as single junction and have recently attained 10.6% [53] in a tandem setup. In recent years, introducing inorganic nanoparticles into a polymer matrix has attracted much interest due to numerous advantages.[127] Mainly, there is a large number of possible inorganic components that can be combined with suitable conjugated polymers to absorb at complementary wavelengths even up to the near infrared. Furthermore, the nanoparticles are structurally shapeable (*e.g.,* spheres, rods, tetrapods) and offer an easy adaption of their band gap by changing their size.[65] This additionally offers flexibility regarding morphology of the active layer, especially improving charge transport properties.[128] These hybrid solar cells exhibit efficiencies which cannot compete with fullerene based solar cells yet, but show a steady progress approaching 5%.[129] Common medium and low band gap materials are, *e.g.*, cadmium sulfide [84, 88, 92, 95] and selenide [129–132], copper indium sulfide [93, 109] and selenide [133, 134], and lead sulfide [90] and selenide [135]. The hybrid solar cells investigated in this work comprise *in situ* prepared copper indium sulfide (CIS) nanoparticles embedded in a PSiF-DBT matrix. The *in situ* preparation procedure offers the

advantage that (i) no additional nanoparticles synthesis step using capping agents and their subsequent removal or exchange is necessary, and (ii) that an unobstructed polymer/nanoparticle interface facilitating charge separation is achieved.[95] Following this procedure, metal xanthate precursors (copper and indium *O*-2,2-dimethylpentan-3-yl dithiocarbonate) are mixed with the polymer, coated onto a substrate and via a thermal conversion step the desired nanoparticles are formed inside the polymer matrix through decomposition of the precursors.[93] Byproducts during decomposition are volatile and do not remain in the layer. The facile process and low temperature needed (<200 °C) enable roll-to-roll processing [136] on flexible polymer substrates. State-of-the-art solar cells produced by this route exhibit promising efficiencies of almost 3%.[93] A depiction of this method can be found in Fig. 5.1, accompanied by the basic layout of a hybrid solar cell.

In a previous study, we observed that the electrode materials aluminum and silver behave differently in regard to two things: (i) While aluminum cathodes on these hybrid solar cells lead to higher open circuit voltages, they lack with respect to stability. (ii) Polymer/CIS solar cells with silver cathodes, on the other hand, offer good stability but exhibit reduced V_{OC}.[93] The most prominent difference between aluminum and silver in this respect is the work function. However, its influence on the V_{OC} is much debated and not yet totally clarified.[137, 138] In the present work we focus on an innovative possibility to enhance the overall power conversion efficiency of the aforementioned solar cells by introducing a silver nanolayer acting as aluminum cathode modification. A comprehensive structural investigation was performed by means of transmission electron microscopy (TEM) and time-of-flight secondary ion

mass spectrometry (TOF-SIMS). The solar cell parameters were compared to standard polymer/CIS solar cells with Al and Ag cathodes, respectively, in order to elucidate the influence of the silver interlayer.
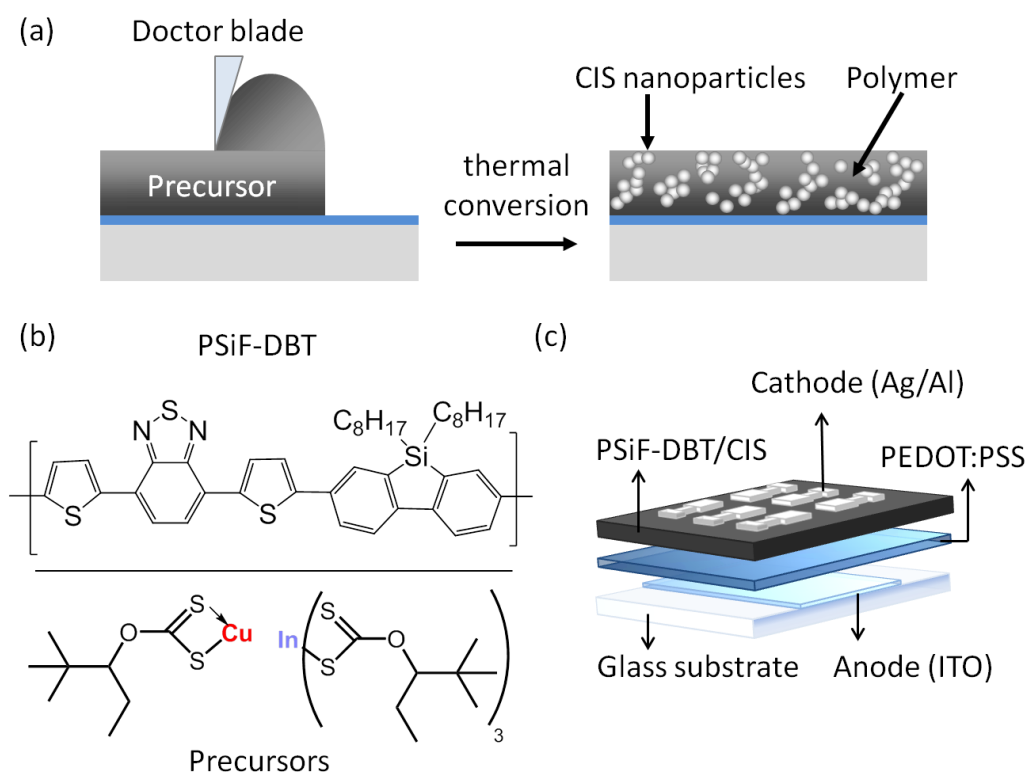
Figure 5.1.: (a) Coating and formation of polymer/CIS nanoparticle active layer, (b) chemical structures of PSiF-DBT and metal xanthate precursors, and (c) schematic layout of a bulk heterojunction nanocomposite solar cell using indium doped tin oxide (ITO) as anode, PEDOT:PSS as hole conducting layer, a blend of PSiF-DBT and CIS as active layer, and silver and/or aluminum as cathode.

5.2. Experimental

Device Fabrication PEDOT:PSS layers (Clevios P VP.AI 4083, Heraeus) were spin-coated from solution using deionized water (1:1, vol.) on glass/ITO sub-

strates (Delta Technologies, R_S = 15 - 25 Ω/sq, sonicated in deionized water and isopropanol, O_2 plasma cleaned (FEMTO, Diener electronic)) and thermally dried in nitrogen atmosphere (150 °C, 15 min). Thereon, nanocomposite layers were prepared by doctor blading of a chlorobenzene solution containing copper xanthates, indium xanthates (copper and indium *O*-2,2-dimethylpentan-3-yl dithiocarbonate),[93] and PSiF-DBT (1-Material, Chemscitech Inc., St. Laurent, Canada) and subsequent thermal treatment in a tube furnace (Heraeus 4/25, temperature program: 15 min heating from room temperature to 195 °C, holding time of 15 min at 195 °C). Aluminum and silver electrodes and interlayers, respectively, were deposited using a thermal evaporation chamber mounted inside a glovebox system (LABmaster dp, MBRAUN Glovebox Technology, Germany) at a base pressure of 8x10^{-6} mbar (nitrogen atmosphere). Evaporation rates: Ag/Al electrode: Ag 0.1 Å s^{-1}, Al 0.1 Å s^{-1} for the first 10 nm, then 10 Å s^{-1}; pure Ag or Al electrodes: 0.1 Å s^{-1} for the first 10 nm, then 10 Ås^{-1}. The substrate was not cooled during evaporation. A cross section of the device was prepared using the "lift-out" technique on a focused ion beam microscope (FEI Nova 200 NanoLab FIB/SEM Dual Beam Microscope).[139]

Characterization I-V curves were recorded using a Keithley 2400 Source-Meter and a custom-made LabVIEW software. Solar simulation was achieved using a Dedolight DLH400D (used in conjunction with Dedolight DEB400D electronic ballast). The intensity of the incoming light was set to 100 mW cm^{-2} providing a spectrum quite similar to AM1.5G (determined using a KippZonen-CMP-11 pyranometer, no spectral mismatch was considered). The

effective device area (0.09 cm^2) was defined by shadow masks applied to the solar cells. TEM analyses were conducted on a Tecnai F 20 microscope (FEI Company, 200 kV, Schottky emitter), a high resolution Gatan Imaging Filter (GIF), an UltraScanCCD camera and a Fischione HAADF STEM detector. EDX-spectrum images were acquired using a Digiscan II controller and an EDAX Sapphire Si(Li) detector. Layer thicknesses were additionally specified on a DekTak 150 surface profiler (Veeco). IPCE spectra were obtained from a MuLTI-mode 4 monochromator equipped with a xenon lamp (AMKO) and a Keithley 2400 SourceMeter. Reflectance spectra were recorded using a Lambda 35 spectrometer equipped with an integrating sphere (PerkinElmer). TOF-SIMS depth profiling analyses were performed using a TOF-SIMS IV (ION-TOF GmbH, Münster, Germany). 25-ns pulses of 25-keV Bi$^+$ (primary ions) were bunched to form ion packets with a nominal temporal extent of ¡0.9 ns at a repetition rate of 10 kHz yielding a target current of 1.0 pA. The analysis area (200 x 200 μ^2) was centered in the sputter area of 300 x 300 μ^2. 30 nA of 3-keV Xe$^+$ was used as sputter ions. Electron bombardment (20 eV) was used to minimize charge built-up at the surface. Desorbed secondary ions were accelerated to 2 keV, mass analyzed in the flight tube, and post-accelerated to 10 keV before detection.

5.3. Results and Discussion

Aluminum electrodes are extensively used in polymer based solar cells due to their matching work function. However, because of its non-noble nature and reactivity towards especially water leading to formation of aluminum oxide

the device stabilities are not sufficient for stable operation. In recent years, especially regarding roll-to-roll production of organic solar cells, silver electrodes became popular.[8] While stability was also improved in the investigated PSiF-DBT/CIS solar cells, the work function of Ag is less favorable leading to lower open circuit voltages.[93] To reduce the aforementioned drawbacks of silver and aluminum, respectively, while maintaining their advantages, we investigated the effects of a thin silver interlayer at the interface between active layer and aluminum electrode. For proper comparison of the respective effects, hybrid solar cells with silver, aluminum, and silver interlayer/aluminum electrodes, respectively, were produced and thoroughly examined. As shown in Fig. 5.2, polymer/CIS hybrid solar cells with aluminum as top electrode material provide a higher V_{OC} while exhibiting a lower fill factor (FF) compared to using a silver cathode. In both cases similar short circuit currents (I_{SC}) and PCEs were achieved (see Tab. 5.1).

cathode material	V_{OC} (mV)	J_{SC} (mA cm^{-2})	FF (%)	PCE (%)
Al	505	9.72	39.7	1.95
Ag	420	11.27	44.0	2.08
Ag/Al	455	10.40	56.1	2.66

Table 5.1.: Characteristic parameters for PSiF-DBT/CIS nanocomposite solar cells with different cathode materials as depicted in Figure 5.2.

However, when applying a thin Ag interlayer (nominal 2 nm) prior to application of the standard Al cathode a distinct PCE enhancement is observed. The outcomes concerning I_{SC} and V_{OC} were as expected: the open circuit voltage lies in between those with unmodified cathodes, while the short circuit current hardly changes. This effect is reproducible; the averaged values of the best 40 devices (approx. 5% of the total devices) and statistical data are given in the supporting information (Table 5.2). The substantial PCE enhancement can
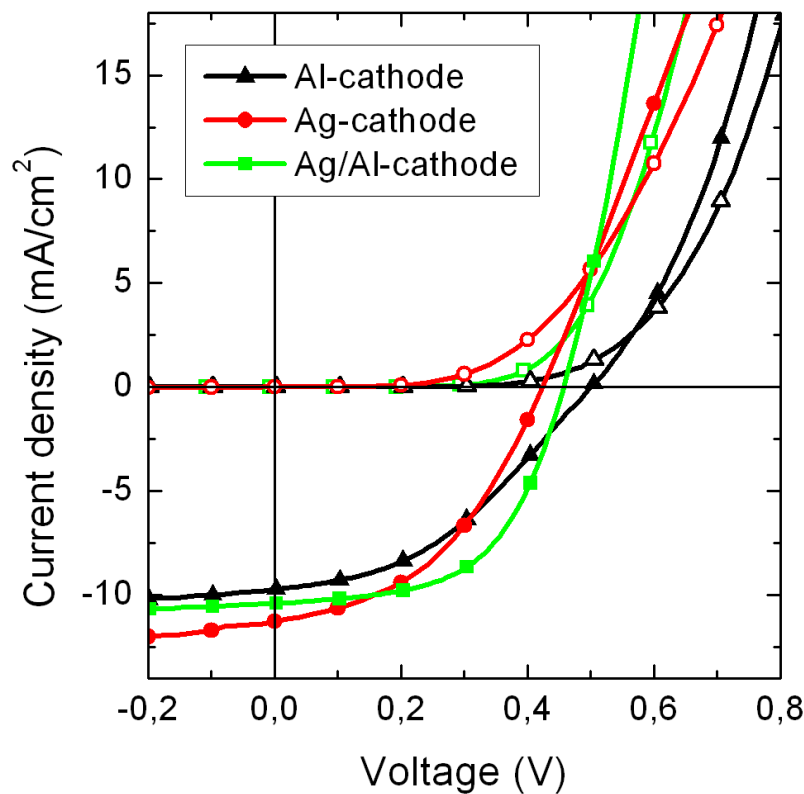
Figure 5.2.: Comparison of typical current density-voltage (J-V) characteristics under AM1.5 illumination for PSiF-DBT/CIS nanocomposite solar cells with different cathode materials (filled symbols denote measurements under AM1.5 illumination, empty symbols without illumination).

mainly be ascribed to the increase in fill factor, namely from 39.7% for Al and 44.0% for silver, respectively, to 56.1% for the Ag-modified Al electrode, which is a clear advantage but also an issue warranting further clarification. The improvement of the fill factor may have several origins, depending on whether silver is present as an interlayer or diffuses into the active layer or into the electrode. For elucidation of this circumstance we prepared a cross section using the "lift-out" technique on a focused ion beam (FIB) microscope [139] and subsequently investigated the specimen by TEM imaging as well as EDXS (energy dispersive X-ray spectroscopy) elemental mappings.
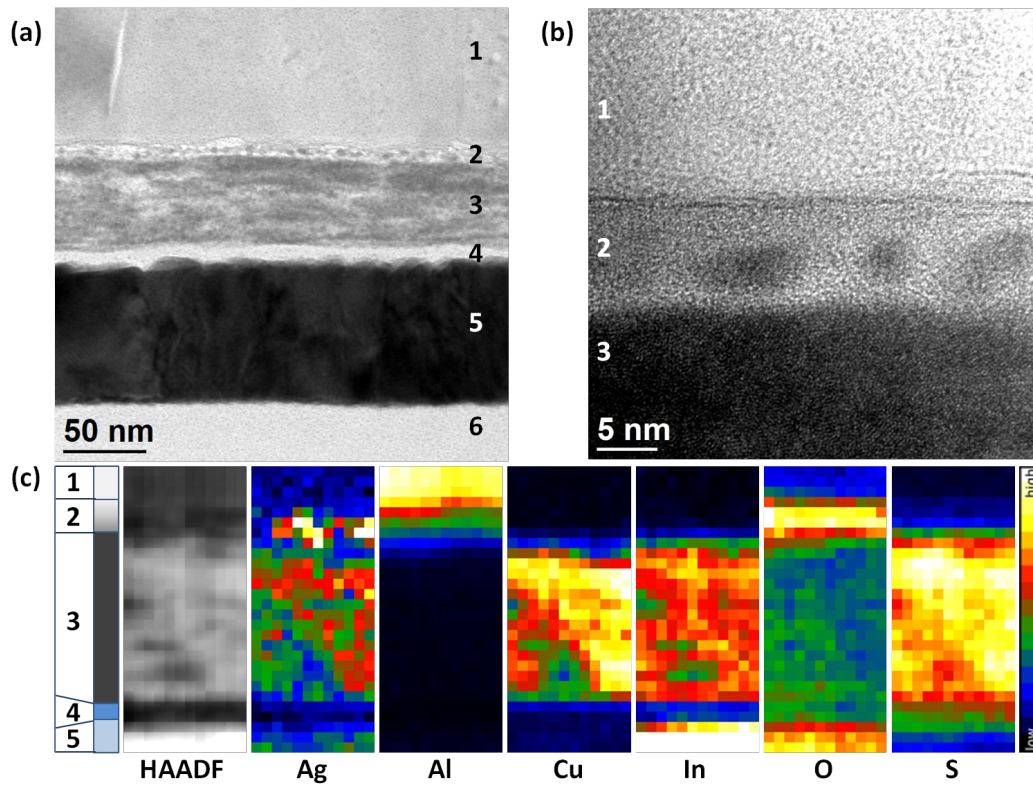
Figure 5.3.: Cross section of a hybrid solar cell with a silver interlayer prepared using the "lift-out" technique. (a) Bright-field TEM image illustrating the basic layout. 1: Aluminum electrode (150 nm), 2: silver layer embedded in AlO_x (8 nm), 3: active layer (54 nm), 4: PEDOT:PSS (9 nm), 5: ITO (85 nm), 6: glass. (b) Magnification of the silver interlayer. (c) High angle angular dark-field (HAADF) image and elemental maps of Ag, Al, Cu, In, O, and S extracted from EDX spectrum imaging.

A bright-field TEM image is depicted in Fig. 5.3(a) showing the device layout of the bulk-heterojunction hybrid solar cell (according to the scheme in Fig. 5.1). From top to bottom, the respective layers are as follows: aluminum (1), silver interlayer (2), polymer/copper indium sulfide nanocomposite layer (3), PEDOT:PSS (4), ITO (5), glass substrate (6). Remarkably, the active layer only amounts to about 50 nm (the layer thickness was additionally verified by profilometric measurements), yet supplying a decent quantity of current. The surface of the active layer remains smooth, although the precursors gen-

erate gaseous byproducts during the annealing step, enabling a plain interface between nanocomposite layer and cathode. The aluminum layer is present as consistent bulk material. A closer look at the cross section (Fig. 5.3(b)) reveals that the Ag interlayer does not form a continuous layer but silver nanoparticles (darker islands) in an environment of different composition, which appears brighter in the TEM image. The elemental composition determined by EDX spectroscopy shows Ag islands embedded in a matrix of aluminum oxide. The overall thickness of this layer amounts to 8 nm, the nanoparticle diameters range from 5 to 8 nm. Furthermore, silver can be found in lower amounts distributed in the active layer. Smearing of silver over the course of the cutting process is doubtful, as this technique cuts bottom-up, so simple diffusion is most probable. However, attributing the positive influence of silver to effects inside the bulk is unlikely, as silver diffusion would also appear using pure Ag cathodes leading to equal results. In addition, the vicinity of this layer seems darker, *i.e.*, indicating an accumulation of polymer. As electrons are transferred from the CIS layer to the cathode, excess polymer at this interface may impede charge carrier extraction. We are currently exploring in a separate study if an inverse device layout could possibly benefit from this fact. For further clarification of the elemental composition in the respective layers TOF-SIMS analyses were conducted. A TOF-SIMS image of the FIB-cut area revealed that material from all layers was "sprayed" onto the surrounding electrode surface, extending out to about 500 μm. Therefore, depth profiles were obtained at positions with sufficient distance to the contaminated area (see supporting information Figure 5.6). Normalized depth profiles are shown in Fig. 5.4. Due to the thick cathode ($\approx$ 150 nm) the depth resolution deteriorates to less
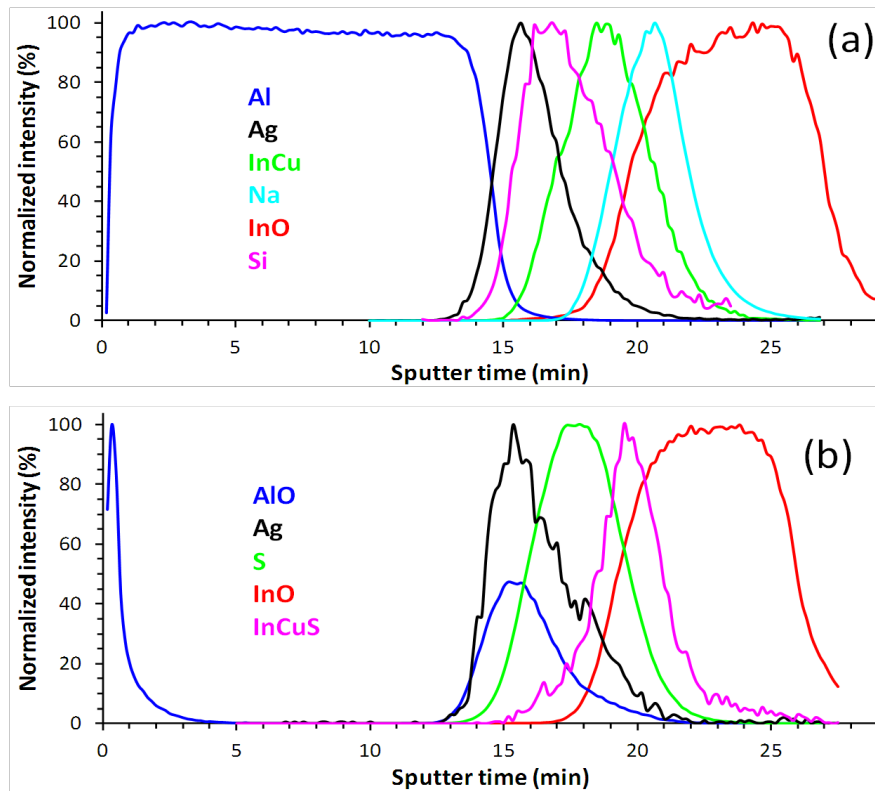
Figure 5.4.: TOF-SIMS depth profiles. (a) Positive ion mode, InCu is a marker for CIS, Na is a marker for PEDOT:PSS, InO is a marker for ITO, and Si is a marker for PSiF-DBT. (b) Negative ion mode, AlO is a marker for aluminum oxide, S is a marker for both CIS and PSiF-DBT, and InCuS is a marker for CIS.

resolution when reaching the active layer, however, valuable information can still be extracted. Due to minor interlayer mixing during the sputter process a small amount of material is pushed into deeper layers, which is manifested as tailing in the profiles. It is thus difficult to detect small degrees of material migration in the sputter direction. The most prominent result of the analysis confirms the interlayer composition, showing clearly an overlap of aluminum oxide and silver. The intensity profiles for Cu, In and S match perfectly, but the CIS and polymer (represented by Si) profiles obviously are not congruent, rather suggesting a polymer rich layer close to the cathode, as noticed above in

the TEM/EDX section. Na and InO, respectively, complete the profiles denoting PEDOT:PSS and ITO, respectively. Based on TEM- and TOF-SIMS-analyses the electrode interlayer was identified as silver nanoparticles (particle size: 5 to 8 nm) embedded in an aluminum oxide matrix, so plasmonic effects could be considered as a possible reason for the fill factor enhancement. Utilizing silver nanoparticles (or Au, Al, Cu) as plasmonic enhancers is no novelty.[140] Positioning them at the metal/semiconductor interface may excite surface plasmon polaritons (SPP), electromagnetic waves guided along the interface enhancing the local field density. However, the surface plasmon resonance energy of silver nanoparticles increases with decreasing diameter.[141] Additionally, the intensity of absorption and scattering is directly proportional to the volume of the nanoparticles.[142] Keeping in mind that the nanoparticles found in the discussed interlayer are smaller than 10 nm, the resulting intensity would be hard to detect and, furthermore, the plasmonic resonance wavelength is shifted into the ultraviolet regime, where the used glass substrates show no transmittance. Thus, the assumption that plasmonic effects are responsible for the fill factor enhancement is implausible, as their influence is marginal at best. In fact, this was verified experimentally, as cells prepared with aluminum and silver-modified aluminum cathodes hardly differ in reflection (see Fig. 5.5(a)), especially in the low wavelength range where plasmonic effects could occur. Additionally, incident photon to electron conversion efficiency measurements (IPCE) of pure and silver-modified aluminum cathodes were conducted to determine if a difference in quantum efficiency occurs. In the IPCE spectra depicted in Fig. 5.5(b) no significant differences towards plasmonic effects can be observed, supporting the results of the reflection spectroscopy. In any case,

charge carrier generation over a broad wavelength range up to 900 nm can be observed. As PSiF-DBT only absorbs light up to about 700 nm this extended current generation (from 700 to 900 nm) can be assigned to CIS.[93]
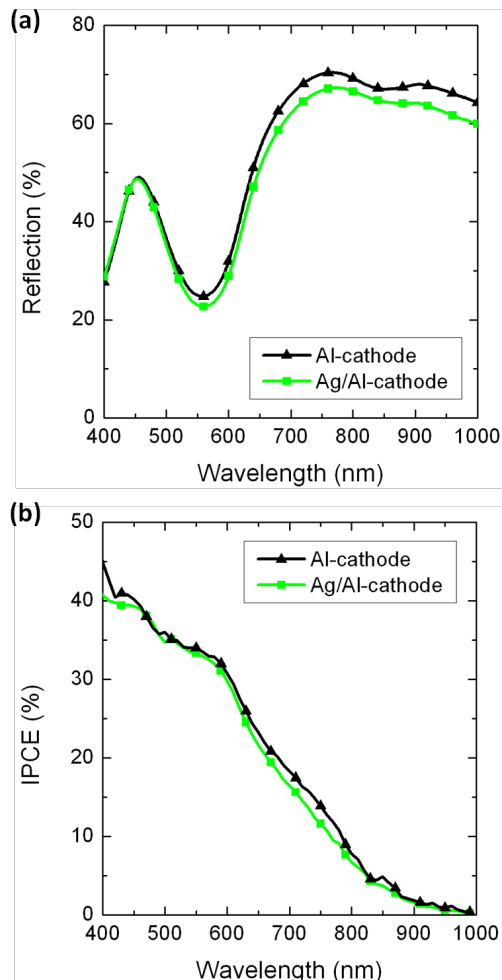
Figure 5.5.: (a) Reflection spectra and (b) IPCE measurements of typical hybrid solar cells with pure aluminum (black triangles) and silver-modified aluminum (green squares) cathodes (J-V curves of these particular solar cells can be found in the supporting information, Figure 5.7).

Even if structural and optical characterization cannot provide sufficient evidence for the phenomena, they can explain the effects at the interface. Specif-

ically, when reflecting on the J-V-curves depicted in Fig. 5.2, additional information can be found based upon present knowledge: there are three typical regions appearing in current density-voltage curves.[143, 144] The linear regime at low positive and negative voltages is generally interface-dependant and gives information about shunt resistances. At intermediate positive voltages the current density is controlled by the diode and shows exponential behavior. For higher voltages electric characteristics are mainly attributed to the bulk semiconductor as well as contact resistances providing information on the series resistance. Valuable data can be retrieved when applying tangents to the curves at the intersections with the x- and y-axis, respectively. The reciprocal values of the slopes represent the shunt (at I_{SC}) and serial resistance (at V_{OC}), respectively.[143] While the shunt resistance hardly changes with electrode material, strong varieties of the serial resistance are apparent. Examining the J-V curves of our solar cells with a pure Al-cathode, only a moderate slope occurs at bias voltages around V_{OC}. This could be explained by the low difference in work function of aluminum to the LUMO of polymer and copper indium sulfide, respectively, facilitating charge carrier injection. This would lead to enhanced charge carrier recombination, strongly influencing the fill factor; however, the insulating interfacial aluminum oxide reduces charge carrier injection. Conversely, extraction of charge carriers is also impeded, which obviously has a greater and detrimental impact than injection.[138] The short circuit current should also be affected; however, the built-in field (V_{bi}), which acts as driving force for exciton dissociation, for solar cells with pure aluminum electrodes is higher compared to solar cells with pure Ag cathodes, compensating this adverse effect. Notably, the fill factor for PSiF-DBT/CIS solar cells with pure

silver cathodes is considerably larger than when using aluminum electrodes, which can be ascribed to the lower serial resistance due to an unobstructed interface between electrode and active layer. Then again, it is still far from the values obtained with our modified cathode. This can be explained by the fact that the V_{bi}, when using pure silver cathodes, obviously does not suffice for efficient exciton dissociation, thus, limiting the fill factor caused by recombination. In the silver-modified Al electrode the silver nanoparticles are too small to completely change the work function to the value of pure silver, so the V_{bi} remains adequate for efficient dissociation and charge carrier transport. Additionally, this reduces unintentional charge carrier injection. Furthermore, the silver nanoparticles infiltrate the insulating aluminum oxide layer, which offers pathways for charge carriers. This significantly reduces the serial resistance of the interface and enables superior charge carrier extraction.

5.4. Conclusion

In summary, we have studied the influence of silver nanoparticles acting as modification of an aluminum electrode in PSiF-DBT/CIS nanocomposite solar cells. The silver interlayer was introduced by deposition of a silver layer with nominally 2 nm. Interestingly, TEM images of a cross section as well as TOF-SIMS measurements of a finished device exhibit that silver is present in the form of nanoparticles (5 to 8 nm diameter) embedded in an aluminum oxide layer. This modification results in V_{OC} and I_{SC} which lie between hybrid solar cells with pure aluminum and silver cathodes, respectively, but expose a distinct fill factor enhancement. To clarify if plasmonic effects due to

the silver nanoparticles could occur reflection and IPCE measurements were conducted. However, the results show no indication towards this assumption. According to the J-V curves the series resistance of devices with the silver modified aluminum cathodes is significantly lower than with unmodified cathodes. This strongly indicates that the silver nanoparticles facilitate charge transport through the impeding aluminum oxide layer. The obtained results propose that making use of the introduced process could possibly also improve the fill factors of other polymer based solar cells with aluminum (or other non-noble) electrodes, as the (mostly insulating) oxide layers could be infiltrated with silver nanoparticles, which offer low-resistance pathways for charge carriers.

Supporting Information Available Characteristic solar cell parameters averaged over 40 solar cells and statistical data on the PCEs of the fabricated solar cells. Positions of FIB-cut and TOF-SIMS profiling areas as well as current density-voltage curves of the polymer/CIS hybrid solar cells used for IPCE measurements. This material is available free of charge via the Internet at http://pubs.acs.org.

5.5. Supporting Information

Cathode material	V_{OC} (mV)	J_{SC} (mA cm^{-2})	FF (%)	PCE (%)
Al	494 ± 40	8.74 ± 0.42	41.9 ± 2.9	1.80 ± 0.11
Ag	435 ± 26	10.82 ± 0.39	44.3 ± 2.5	2.08 ± 0.18
Ag/Al	469 ± 21	9.93 ± 0.51	54.4 ± 1.5	2.53 ± 0.06

Table 5.2.: Characteristic parameters and their standard deviations for PSiF-DBT/CIS nanocomposite solar cells with different cathode materials averaged over the best 40 solar cells each.

Totally 826 devices with Ag/Al electrodes were produced in the course of this investigation, 107 (approx. 13%) are "champion devices" exhibiting PCEs greater than 2 %. About 28% each perform between 1.5% and 2% (229 devices) and 1% and 1.5% (237 devices), respectively. *Ca.* 8.6% (71) of all devices show PCEs below 0.1%.

500×500 and
25×25 µm^2
TOF-SIMS imaging

TOF-SIMS depth
profiling: 300×300
µm^2 sputtering and
200×200 µm^2
analysis.

TOF-SIMS depth
profiling: 750×750
µm^2 sputtering and
500×500 µm^2
analysis.

FIB cut

Before analysis   After analysis
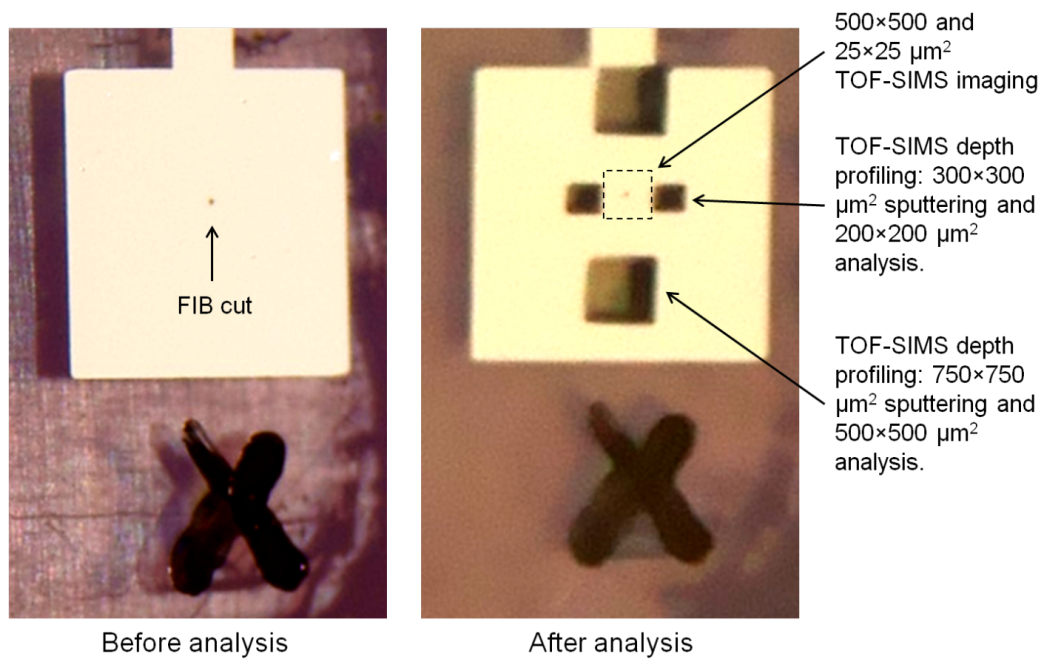
Figure 5.6.: Positions of FIB-cut and TOF-SIMS measurements on the 9 mm^2 polymer/CIS hybrid solar cell. TOF-SIMS depth profiling was performed on 2 scales corresponding to an information area of 200 x 200 µm and 500 x 500 µm in order to see if a larger analysis area improved the quality of the data, which was not the case.
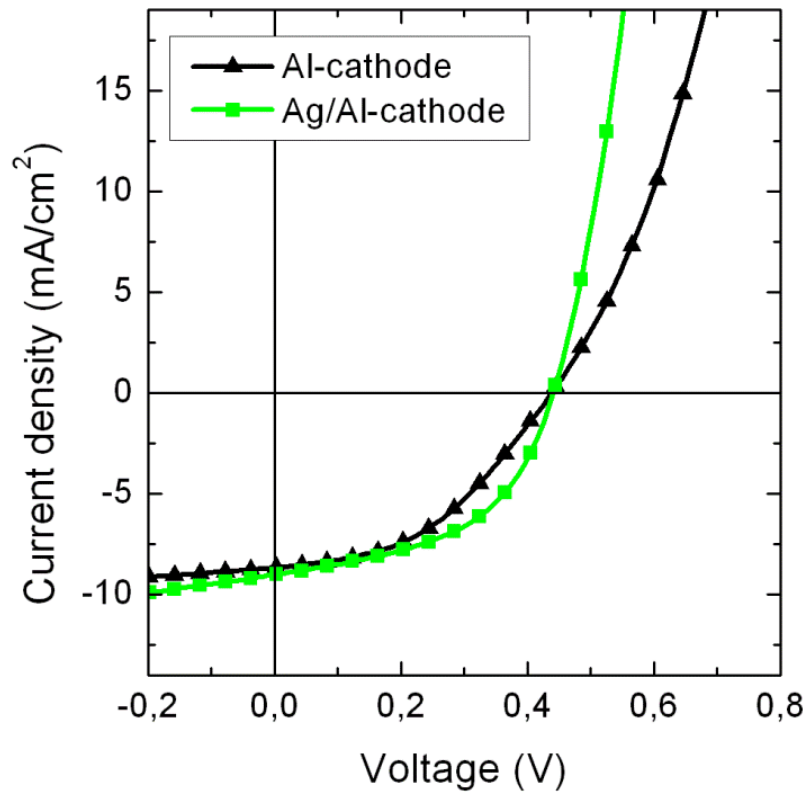
Figure 5.7.: Current density-voltage curves of the polymer/CIS hybrid solar cells used for IPCE measurements.

6. Silver-modified Aluminum Electrodes in Polymer:PCBM Solar Cells

"Whether you can observe a thing or not depends on the theory which you use. It is the theory which decides what can be observed."

Albert Einstein (1926)

(cited by Salam et al. (1990) [145])

The following chapter was submitted to and accepted to publish at the

39th Photovoltaic Specialists Conference Proceedings (IEEE):

Comparing Photovoltaic Parameters of Conventional Cathodes with a Novel Silver Nanoparticle/Aluminum Cathode in Polymer Based Solar Cells

Mario Arar, Wernfried Haas, Ferdinand Hofer, Thomas Rath, and Gregor Trimmel

6.1. Introduction

Solar power, as a readily available energy resource, is most promising for perpetual clean energy when thinking economically and future-oriented. Silicon solar cells are still dominating the PV-market due to their advance in terms of power conversion efficiency (PCE), however, polymer-based solar cells offer several advantages (cost-effective, lightweight, flexible, readily processable) making them a prominent target of scientific interest. While leading polymer-based solar cells rely on fullerene-derivatives as electron acceptors (with continuous progress in PCE, already having cleared the 10% hurdle for single junction organic solar cells [146]), inorganic nanoparticles as acceptors introduced in a polymer matrix entered the stage due to numerous benefits (*e.g.,* shapeability [127], band gap tuning via size [65], improved charge carrier transport properties through flexible morphologies of active layers [128]). In this work, both fully organic and hybrid inorganic-organic solar cells were examined using PSiF-DBT and PCDTBT as donor polymers; PCBM and CIS completed the absorber layers (see experimental part). Hybrid inorganic-organic solar cells were prepared via an in situ route, comprising copper indium sulfide nanoparticles in a polymer matrix. This is achieved by mixing metal xanthate precursors with the respective polymer and coating the solution onto a substrate. Through thermal decomposition of the xanthates (<200 °C) the desired nanoparticles are formed embedded inside the polymer layer; decomposition products are volatile and do not remain inside the film [93]. In a previous work [72] using PSiF-DBT/CIS hybrid solar cells, we observed two major differences when applying different cathode materials: (i) aluminum cathodes establish

higher open-circuit voltages (V_{OC}) at the cost of fill factor. Furthermore, they show shortcomings in stability. (ii) Silver as cathode material on the cells offered higher fill factors and better stability; however, they could not compete with respect to V_{OC}. To combine the advantages of both, a thin silver interlayer was deposited between absorber layer and aluminum electrode.
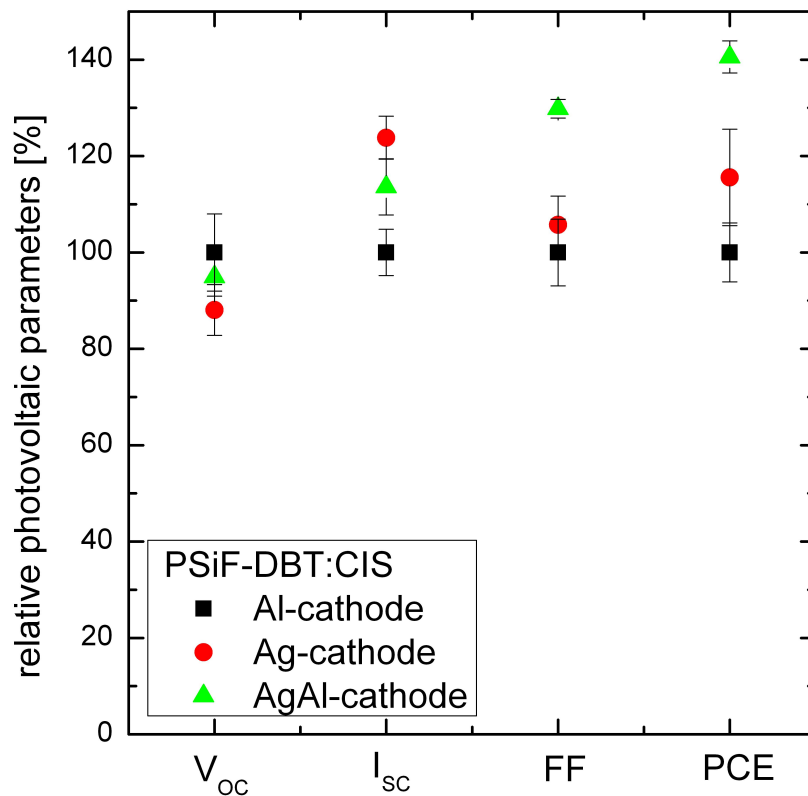
Figure 6.1.: Comparison of the relative photovoltaic parameters open-circuit voltage (V_{OC}), short-circuit current (I_{SC}), fill factor (FF), and power conversion efficiency (PCE) of PSiF-DBT hybrid solar cells [72]

A comparison of solar cell parameters with this sort of cathode compared to regular Al and Ag cathodes revealed an enhancement in overall power conversion efficiency, as displayed in Fig 6.1.

Material	HOMO (eV)	LUMO (eV)
PSiF-DBT [74]	3.6	5.4
PCDTBT [147]	3.6	5.5
PCBM [148]	3.7	6.1
CIS (nano) [82]	3.7	6.0
CIS (bulk) [82]	4.1	5.6

Table 6.1.: HOMO/LUMO Levels of the Active Materials Used

Therefore, in this work we present the influence of this novel electrode on combinations of two low band gap polymers and PCBM as acceptor. Table 6.1 shows the energy levels of the highest occupied molecular orbitals (HOMO) and lowest unoccupied molecular orbitals (LUMO) of the materials used in the course of this work.

6.2. Experimental

Solar cell preparation PEDOT:PSS layers (Clevios P VP.AI 4083, Heraeus) were spin-coated from solution using deionized water (1:1, vol.) on glass/ITO substrates (Xin Yan Technology Ltd., R_S = 10 Ω/sq, sonicated in deionized water and isopropanol, O_2 plasma cleaned (FEMTO, Diener electronic)) and thermally dried in nitrogen atmosphere (150 °C, 15 min). The donor polymers used were: poly[(2,7-silafluorene)-*alt*-(4,7-di-2-thienyl-2,1,3-benzothia-diazole)] (PSiF-DBT), and poly[*N-9″*-heptadecanyl-2,7-carbazole-*alt*-5,5-(4′,7′-di-2-thienyl-2′,1′,3′-benzothia-diazole)] (PCDTBT). In case of inorganic acceptors, nanocomposite layers were thereon prepared by doctor blading of a chlorobenzene solution containing copper xanthates, indium xanthates (copper and indium *O*-2,2-dimethylpentan-3-yl dithiocarbonate) [93], and the

respective polymers and subsequent thermal treatment on a programmable heating plate (CAT MCS66, temperature program: 15 min heating from room temperature to 195 °C, holding time of 15 min at 195 °C) in nitrogen atmosphere. In case of PCBM as acceptor different mass ratios were chosen according to literature: PSiF-DBT:PCBM 1:2 (w/w) [74], PCDTBT:PCBM 1:4 (w/w) [147]; the respective blends were doctor bladed. Aluminum and silver electrodes and interlayers were deposited using a thermal evaporation chamber mounted inside a glovebox system (LABmaster dp, MBRAUN Glovebox Technology, Germany) at a base pressure of 8×10^{-6} mbar (nitrogen atmosphere). Evaporation rates: AgAl electrode: Ag 0.1 Å s^{-1}, Al 0.1 Å s^{-1} for the first 10 nm, then 10 Å s^{-1}; pure Ag or Al electrodes: 0.1 Å s^{-1} for the first 10 nm, then 10 Ås^{-1}.

Characterization Current density-voltage (I-V) curves were recorded using a Keithley 2400 SourceMeter and custom-made Lab-View software. The solar cells were illuminated using a Dedolight DLH400D (used in conjunction with Dedolight DEB400D electronic ballast). The intensity of the incoming light was set to 100 mW cm^{-2} providing a spectrum quite similar to AM1.5G (determined using a KippZonen-CMP-11 pyranometer, no spectral mismatch was considered). The effective device area (0.0784 cm^2) was defined by shadow masks applied to the solar cells. A cross section of the device was prepared using the "lift-out" technique on a focused ion beam microscope (FEI Nova 200 NanoLab FIB/SEM dual beam microscope) [139]. TEM analyses were conducted on a Tecnai F 20 microscope (FEI Company, 200 kV, Schottky emitter) equipped with a high resolution Gatan Imaging Filter (GIF), an UltraScanCCD

camera and a Fischione HAADF STEM detector. EDX-spectrum images were acquired using a Digiscan II controller and an EDAX Sapphire Si(Li) detector. EDX quantification was performed using the approximation for thin films by Cliff and Lorimer [105]. Layer thicknesses were additionally specified on a DektakXT surface profiler (Bruker).

6.3. Results and Discussion

The work functions of both all-aluminum and all-silver electrodes match the energy levels in polymer-based solar cells. As a non-noble metal Al shows reactivity to oxygen and water, quickly forming aluminum oxide layers in ambient atmosphere. Thus, research soon extended to other, more stable materials, such as Ag [8]. Its lower work function, however, is slightly unfavorable resulting in lower open-circuit voltages. To reduce the aforementioned disadvantages of Al and Ag, respectively, we deposited a thin silver layer (nominally 2 nm) onto the active layer prior to the aluminum electrode (referred to as AgAl). In PSiF-DBT:CIS hybrid solar cells a strong fill factor enhancement compared to both pure electrodes could be observed; open-circuit voltage and short-circuit current density (I_{SC}) of the solar cells with silver-modified aluminum electrodes settle in between those with unmodified electrodes. Thus, the overall power conversion efficiency was increased significantly (see Fig 6.1). To determine the origin of this enhancement a cross section of our device was prepared using the "lift-out" technique on a focused ion beam (FIB) microscope. A combination of TEM imaging and EDXS elemental mappings revealed an interesting interlayer between the bulk heterojunction active layer and the aluminum electrode.

The silver interlayer is not formed continuously but rather as aggregated silver nanoparticles inside an aluminum oxide matrix (see Fig 6.2). These findings were additionally confirmed by means of time-of-flight secondary ion mass spectrometry (TOF-SIMS) [72].
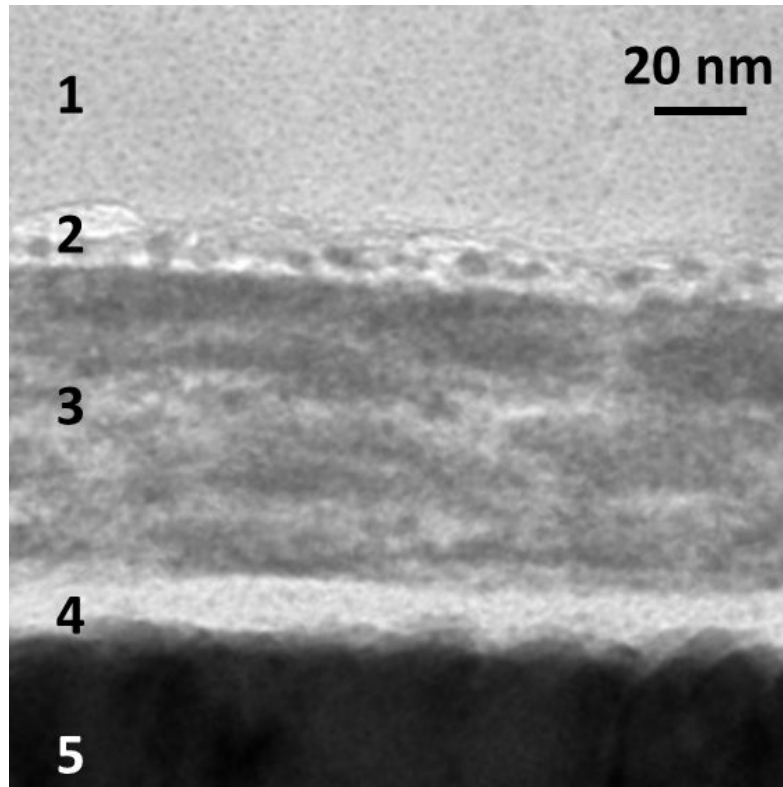
Figure 6.2.: Bright-field TEM image illustrating the cross section of a PSiF-DBT:CIS hybrid solar cell with AgAl cathode prepared using the "lift-out" technique. 1: aluminum electrode; 2: silver layer embedded in AlO_x; 3: active layer; 4: PEDOT:PSS; 5: ITO (recorded by W. Haas).[72]

The distinct AlO_x layer formed at the interface clearly increases the serial resistance by inhibiting the charge carrier extraction and thus leading to lower fill factors. When applying pure silver cathodes there is no such interfering interlayer, leading to a higher fill factor. However, the V_{OC} is limited due to the

slightly less favorable work function, which entails a smaller built-in field, *i.e.,* the driving force for exciton dissociation. Therefore, when introducing silver nanoparticles into the electronically obstructive AlO_x layer, the built-in field is still dominated by the Al cathode, however, an easier charge carrier extraction is offered. Polymer:fullerene solar cells did not exhibit the same behavior as polymer:CIS hybrid solar cells. The relative changes in photovoltaic parameters with aluminum cathodes as reference as well as their respective standard deviations for PSiF-DBT:CIS hybrid solar cells are displayed in Fig. 6.1, where substantial changes depending on the cathode material are observable. On the other hand, solar cells with PCDTBT:PCBM as absorber material exhibit hardly any changes in photovoltaic parameters, independent of the cathode material used. PSiF-DBT:PCBM solar cells display only slightly lower values when applying the AgAl electrode, while utilizing a pure silver electrode even decreases the fill factor and, thus, the power conversion efficiency (see Fig 6.3). According to literature, as summarized in Table 6.1, the HOMO and LUMO levels of PSiF-DBT and PCDTBT are quite similar, as are those of CIS nanoparticles and PCBM. Therefore, we assumed that the cathode modification would lead to an enhancement in fill factor as well. However, the positive effects of the silver interlayer as observed in the PSiF-DBT:CIS hybrid solar cells did not occur when PCBM was used as acceptor.

It seems, as if the same mechanisms as described for PSiF-DBT:CIS hybrid solar cells do not appear at the PCBM-cathode interface. The typical fill factors in polymer:PCBM solar cells usually are comparable or even exceed the best values for PSiF-DBT:CIS hybrid solar cells, indicating issues based on the inorganic acceptor phase. Therefore, it is feasible that the contact between the
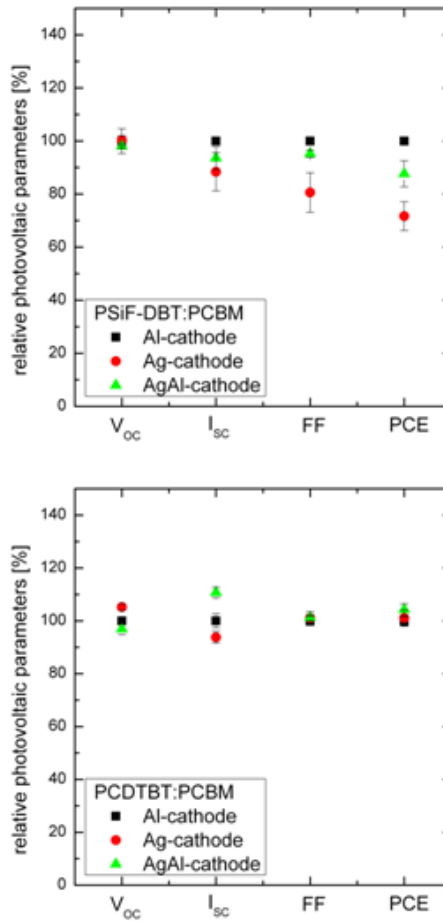
Figure 6.3.: Comparison of the relative photovoltaic parameters open-circuit voltage (V_{OC}), short-circuit current (I_{SC}), fill factor (FF), and power conversion efficiency (PCE) for different polymers.

inorganic phase and the metal electrode behaves differently compared to the PCBM-metal contact in polymer:PCBM solar cells, which shows that a direct knowledge transfer regarding well performing electrodes from polymer:PCBM to polymer:nanoparticle hybrid solar cells, and *vice versa*, is not generally expedient.

6.4. Conclusions

In this work, we intended to apply the positive effect of a silver interlayer between absorber layer and top electrode, as found for hybrid solar cells, which led to a significant enhancement in fill factor [72], to polymer:PCBM solar cells. The results indicate that the enhancement induced by cathode modification in PSiF-DBT:CIS hybrid solar cells seems to stem from the CIS nanoparticle-metal interface and are, therefore, not directly applicable to other polymer-based solar cells. It can be assumed, that the PCBM-metal junction cannot be enhanced by introducing a silver interlayer; no fill factor enhancement could be observed.

7. Synopsis and Perspective

"We must trust to nothing but facts: These are presented to us by Nature, and cannot deceive. We ought, in every instance, to submit our reasoning to the test of experiment, and never to search for truth but by the natural road of experiment and observation."

Antoine Lavoisier (1790) [149]

7. Synopsis and Perspective

In the last decade, polymer-based solar cells have attracted much interest and, thereupon, made rapid progress. As a very fascinating branch, organic-inorganic hybrid solar cells also found their way into scientific research. Their fabrication, function, and advantages are described in Chapters 1 and 2: "Introduction" and "Basics", respectively.

The experimental part of this thesis comprises studies in polymer-based solar cells, which can be divided into two major investigation topics: morphology and electrode modification. Chapter 3, "Variation of PSiF-DBT:CIS mass ratio", deals with the influence of morphology in *in situ* prepared PSiF-DBT:CIS hybrid solar cells. A series of solar cells with different polymer:inorganic mass ratios, ranging from 1:3 to 1:15, have been prepared and thoroughly investigated. Additionally, numerical simulations based on the drift diffusion model have been conducted at the Institute for Theoretical Physics (Graz University of Technology).

The changes in photovoltaic performance of solar cells based on different morphologies allowed inferences regarding charge carrier generation and percolation. While the ideal morphology for charge generation in the polymer phase is found at a mass ratio of 1:9, which corresponds to a volumetric ratio of about 1:2, and this ratio primarily excels in terms of fill factor, the other photovoltaic parameters do not allow for a clear trend to be identified. Moreover, very interesting insights concerning the impacts on the separate parameters could be gained, especially on the interplay between polymer- and CIS-phase.

The simulations additionally provided access to theoretical options for substantially enhancing PSiF-DBT:CIS solar cells by slight adjustments of electron and hole transport level offsets and built-in voltage. These changes could be re-

alized through chemical tailoring, material optimization, and suitable interlayers. The characteristic solar cell parameters from the experiments are depicted in Fig. 7.1, accompanied by results from the simulations with resembling characteristics as well as idealized parameters.
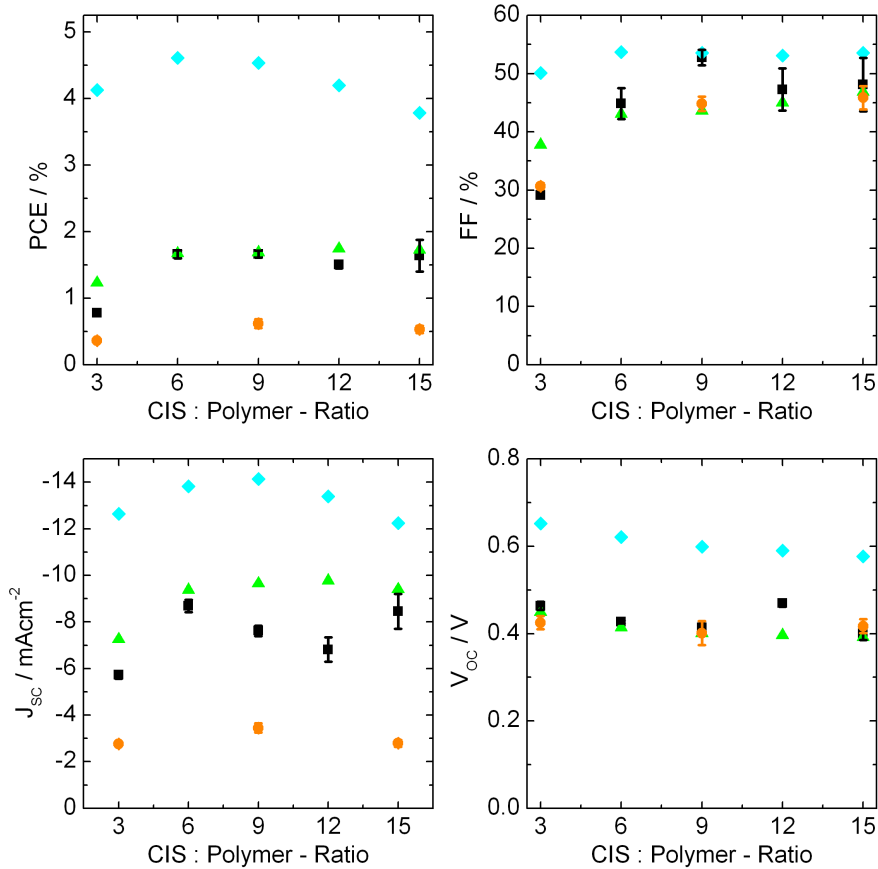
Figure 7.1.: Results for power conversion efficiency, fill factor, short circuit current density (J_{SC}), and open circuit voltage (V_{OC}) extracted from experiments (black squares), resembling simulations (green triangles), and simulations using idealized parameters (cyan diamonds) for PSiF-DBT:CIS solar cells. The orange circles represent the results for PS:CIS solar cells.

Based on these findings, the subsequent Chapter 4, "Polystyrene:CIS solar cells", copes with the separate contribution of the CIS-phase to the performance in hybrid solar cells. For that purpose, the same *in situ* process is applied to fabricate a CIS nanocomposite in a polystyrene matrix. The PS counterpart was introduced as optically transparent and inactive filler material, which provides a fundament for a CIS-phase equivalent to the beforehand examined hybrid solar cells. The charge separation process, apparently based on a Schottky-junction at the CIS-electrode interface, performs exceptionally well. According to the experimental results, the separate CIS-phase exhibits about one third of the power conversion efficiency of PSiF-DBT:CIS hybrid solar cells, which is directly ascribable to a breakdown in short circuit current density (see Fig. 7.1). Albeit a direct knowledge and performance transfer presumably is not valid, this study provides information on the capability of inorganic nanocrystals in polymer matrices.

An approach to enhance the overall performance in PSiF-DBT:CIS hybrid solar cells through a simple modification of the aluminum electrode is described in Chapter 5, "Silver-modified Aluminum Electrodes in PSiF-DBT:CIS Solar Cells". This enhancement is caused by thermal evaporation of a nominally 2 nm thin silver interlayer between absorber layer and electrode. This interlayer shapes in form of silver nanocrystals with a size of 5 to 8 nm embedded in an aluminum oxide layer. Through the infiltration of the insulating layer faster pathways for charge carrier extraction are facilitated. Thus, the serial resistance is strongly decreased, leading to a substantial increase in fill factor and, therefore, PCE. The fill factor increased from 39.7% (Al cathode) and

44.0% (Ag cathode), respectively, to an astonishing 56.1% with the modified cathode. With open circuit voltage and short circuit current density values found between those of the compared solar cells, the power conversion efficiency could be amplified from 1.95% (Al cathode) and 2.08% (Ag cathode), respectively, to 2.66% with the silver-modified aluminum cathode.

In the last experimental part, Chapter 6, "Silver-modified Aluminum Electrodes in Polymer:PCBM Solar Cells", a possible influence of the modified aluminum electrode on polymer:PCBM solar cells was investigated. These experiments were conducted with two similar low band gap polymers, PSiF-DBT as well as PCDTBT, as donors. However, in the case of PCBM as acceptor material no positive influence on any characteristic parameter could be evoked through the cathode modification. The impact of the silver interlayer in the PSiF-DBT:CIS was, thus, attributed to an enhancement of the CIS nanoparticle-metal interface.

Outlook   The research topics and their respective results summarized above indicate the complexity of the components themselves as well as their interplay. An isolation of the separate contributions poses a great challenge; however, upon success it can reward with astounding insights. Some of the conclusions presented in this work opened doors to topics definitely worth investigating. Albeit the results indicate a multitude of white spots on the map, they clearly show the potential of hybrid solar cells.

Appendix

Appendix A.

General Experimental Information

This chapter comprises general information that is not *limited* to certain experiments. If not specifically stated otherwise, the data and information provided here describe those measuring instruments (see Table A.1), materials and chemicals (see Table A.2) and characterization techniques (cf. section A.2) used over the course of the complete experimental work. It is supposed to provide more detailed information for the interested reader to be able to reproduce the measurements presented in this thesis.

A.1. Preface

A.1.1. Measuring Instruments

In case of two equivalent instruments from different manufacturers, the upgrade from one to another will be noted at the respective passage in the text.

instrument	label	manufacturer
doctor blading unit	Coatmaster 509 MC	Erichsen
electron microscope	Tecnai 12	FEI Company
electron microscope	Tecnai F 20	FEI Company
glovebox + evaporation unit		MBraun
hot plate	MCS 66	CAT
monochromator + Xenon lamp	MuLTImode4	AMKO
plasma etcher	Femto	Diener electronic
profilometer	DekTak 150	Veeco
profilometer	DekTak XT	Bruker
sourcemeter	2400	Keithley
spin coater	CT 62	Karl Suss Technique
TOF-SIMS	TOF-SIMS IV	ION-TOF GmbH
tube furnace	ROF 4/25	Heraeus
ultrasonic cleaner	USC1200D	VWR
UV/Vis spectrometer	UV-1800	Shimadzu
UV/Vis spectrometer	Lamda 35	PerkinElmer

Table A.1.: Measuring instruments used

A.1.2. Chemicals and Materials

If a material is listed more than once, the experimental section contains information on the actually used product/batch.

chemical/material	purity/description	source of supply
acetone	99%	Sigma-Aldrich
acetonitrile	99.8%, anhydrous	Sigma-Aldrich
aluminum	99.999%, pellets	Kurt J. Lesker
chloroform	$\geq$ 99.9%, HPLC grade	Sigma-Aldrich
chlorobenzene	99.9%, HPLC grade	Sigma-Aldrich
copper xanthate		AGLYCON
indium xanthate		AGLYCON
isopropyl alcohol	puriss	Sigma-Aldrich
ITO-coverd glass substrate	R_S= $15-25$ $\Omega/\square$	Delta Technologies
ITO-coverd glass substrate	R_S= 10 $\Omega/\square$, patterned	KINTEC
ITO-coverd glass substrate	R_S= 10 $\Omega/\square$, patterned	Xin Yan Technology
[60]PCBM	99.5%	Solenne BV
[70]PCBM	99%	Solenne BV
PEDOT:PSS	Clevios P VP AI 4083	Heraeus
PMMA	avg $M_W \approx 350.000$	Aldrich
PSiF-DBT	OS0927	1-material
silver	99.99%, wire	Umicore
TBAP	$\geq$ 99%	Fluka
toluene	$\geq$ 99.9%	Sigma-Aldrich

Table A.2.: Chemicals and materials used

A.2. Characterization Techniques

A.2.1. I-V Measurements

As a basic characterization technique, the current (I) is measured as a function of the voltage (V) applied between the electrodes of the solar cell. The current density (J) is then calculated as current per solar cell area (A):

$$J = \frac{I}{A} \tag{A.1}$$

As already described in Sec. 2.2.1 the power conversion efficiency can be determined from the resulting graph/data. The applied voltage is typically in the regime between +1.5 and -0.5 V. The according current is measured via a custom made LabView software, which also controls the voltage source of the Keithley 2400 SourceMeter.

During measurement the devices were kept in a glovebox in N_2 atmosphere; the mean irradiance was checked (and the measured value employed in the calculations) after every measured series through a photodiode arranged in closest proximity to the measured device.

A.2.2. UV/Vis-Spectrometry

Considering UV/Vis-spectrometry to be a straight-forward measuring technique involves the risk of being to casual about it. Especially, when dealing

with composite thin films on a substrate with additional layers (ITO, PE-DOT:PSS, or the like). The difference in optical density (represented by the refraction index) may greatly affect the transmission and reflection, respectively. Therefore, absorption in this work was determined through reflection and transmission measurements of the samples from both sides (glass and absorber layer).

A.2.3. IPCE Measurements

Measurement of IPCE corresponds to a technique that is able to determine the conversion efficiency of impinging photons of a given wavelength into electrons. For that purpose, still inside the glovebox single solar cells are cut from the device and transferred into a hermetically sealed measuring module with a quartz glass window and contacts for current measurements. A white light source in combination with a monochromator (Xenon lamp + monochromator, MuLTImode4, AMKO) provides monochromatic light in 10 nm steps illuminating the solar cell; the resulting current is measured (Keithley 2400).

As a reference, a calibrated photodiode (calibrated by Hamamatsu Photonics K.K.) is measured at the beginning and the end of each series. Via the calibration factor the actual IPCE can be calculated.

A.2.4. S/TEM, EDX, SAED

These analyses have been conducted at the Austrian Centre for Electron Microscopy and Nanoanalysis, Graz University of Technology and Graz Centre

for Electron Microscopy.

Performing electron microscopic analyses is a science itself, a brief summary could never cope with its challenges so I refrain from trying and rather like to refer the interested reader to the aforementioned institute.

A.2.5. TOF-SIMS

Time-of-flight secondary ion mass spectrometry analyses were conducted at the Department of Energy Conversion and Storage (Technical University of Denmark). Basically, the sample's surface is sputtered with a focused ion beam (here: Xe^+). The ejected ions are collected to determine the elemental composition of the sputtered material by means of mass spectrometry.

The validity of the result strongly depends on the sample's composition. The difficulties regarding the hybrid solar cells analyzed herein are as follows: generally, the depth resolution of digging profiles deteriorates for longer sputter times. This issue is even more serious with these devices, where prior to reaching the (very thin) active layer a relatively thick electrode has to be ablated. Hence, the resolution suffers and one has to be cautious when interpreting the collected data. First to mention is, that all signals intensities are normalized as the absolute signal contains no information on the composition. Furthermore, owing to the sputter process small amounts of the material can be pushed into deeper layers, which results in the observable tailing of the signals. Additionally, the different densities of the layers may lead to a discrepancy between layer thickness and sputter time window. Therefore, it is neither possible to provide exact information on the layer thickness nor on a possible

migration of small amounts of material in sputter direction (migration towards top surface is well measurable).

A.2.6. Transient Absorption Spectroscopy

We were able to garner support from the Department of Chemistry at the Imperial College London. With this technique the sample can be probed and excited at different wavelengths at the same time. The detector records the time-resolved absorption difference, which allows for conclusions on excitation phenomena.

Appendix B.

List of Abbreviations

λ	wavelength
FF	fill factor
I_{SC}	short circuit current
I	current
J_{SC}	short circuit current density
J_{mp}	current density at the maximum power point
P_{in}	incident light power
P_{max}	maximum power point
P	electric power
V_{OC}	open circuit voltage
V_{mp}	voltage at the maximum power point
V	voltage
c	speed of light
e	elementary charge
h	Planck's constant
AZO	aluminum doped zinc oxide
CdSe	cadmium selenide
CIS	copper indium sulfide
CuInS$_2$	copper indium disulfide
EBL	electron blocking layer
EQE	external quantum efficiency
FTO	fluorine doped tin oxide

GO	graphene oxide
HOMO	highest occupied molecular orbital
HTL	hole transport layer
IPCE	incident photon to electron conversion efficiency
IQE	internal quantum efficiency
ITO	tin doped indium oxide
LUMO	lowest unoccupied molecular orbital
MoO$_3$	molybdenum oxide
P3HT	poly(3-hexylthiophene-2,5-diyl)
PbS	lead sulfide
PCBM	phenyl-C61-butyric-acid-methyl ester
PCDTBT	poly[*N-9''*-heptadecanyl-2,7-carbazole-*alt*-5,5-(4',7'-di-2-thienyl-2',1',3'-benzothia-diazole)]
PCE	power conversion efficiency
PEDOT:PSS	poly(3,4-ethylenedioxythiophene)-poly(styrenesulfonate)
PS	polystyrene
PSiF-DBT	poly[(2,7-silafluorene)-*alt*-(4,7-di-2-thienyl-2,1,3-benzothiadiazole)]
TEM	transmission electron microscopy
TiO$_2$	titanium dioxide
TiO$_x$	titanium oxide
UV	ultraviolet
UV-Vis	ultraviolet-visible spectrophotometry
V$_2$O$_5$	vanadium oxide
ZnO	zinc oxide

Appendix C.

List of Figures

Appendix C. List of Figures

Appendix D.

List of Tables

Appendix D. List of Tables

Appendix E.

Bibliography

[1] M. Cendrowski, C. Lorre, and B. Prady. *The Big Bang Theory*. 2009 (cit. on p. iv).

[2] W. Pauli. *Physical chemistry in the service of medicine*. Ed. by M. H. Fischer. 1st ed. 1s. New York, J. Wiley & sons, 1907 (cit. on p. vii).

[3] J. von Liebig. *Chemische Briefe*. 6. Auflage. C.F. Winter'sche Verlagshandlung, 1878, p. 479 (cit. on p. x).

[4] J. D. Newton. *Uncommon Friends: Life With Thomas Edison, Henry Ford, Harvey Firestone, Alexis Carrel, & Charles Lindbergh*. Henry Ford Estate Collection. Harcourt Brace & Company, 1989 (cit. on p. 1).

[5] K. Butti and J. Perlin. *A golden thread: 2500 years of solar architecture and technology*. Cheshire Books, 1980 (cit. on p. 2).

[6] IEA. *Key World Energy Statistics*. Ed. by O. Publishing. 2012 (cit. on p. 3).

[7]   IEA. *Solar Energy Perspectives*. OECD Publishing, Dec. 2011. DOI: 10 . 1787/9789264124585-en (cit. on pp. 3, 4).

[8]   F. C. Krebs. "Fabrication and processing of polymer solar cells: A review of printing and coating techniques." In: *Solar Energy Materials and Solar Cells* 93.4 (Apr. 2009), pp. 394–412. DOI: 10.1016/j.solmat.2008.10.004 (cit. on pp. 4, 32, 80, 99).

[9]   W. Heisenberg. *Physik und Philosophie*. Ullstein Buch. Hirzel, 1959 (cit. on p. 7).

[10] J. Nelson. *The Physics of Solar Cells*. Series on Properties of Semiconductor Materials. Imperial College Press, 2003 (cit. on p. 8).

[11] T. Markvart and L. Castañer. *Practical Handbook of Photovoltaics: Fundamentals and Applications*. Electronics & Electrical. Elsevier, 2003 (cit. on p. 8).

[12] S. Sun and N. Sariciftci. *Organic photovoltaics: mechanisms, materials, and devices*. Optical Science and Engineering. Taylor & Francis, 2010 (cit. on p. 8).

[13] A. Becquerel. "Mémoire sur les effets électriques produits sous l'influence des rayons solaires." In: *Comptes Rendus* (1839), pp. 561–567 (cit. on p. 8).

[14] H. Hertz. "Ueber einen Einfluss des ultravioletten Lichtes auf die electrische Entladung." In: *Annalen der Physik* (1887), pp. 983–1000 (cit. on p. 8).

[15] A. Einstein. "Über einen die Erzeugung und Verwandlung des Lichtes betreffenden heuristischen Gesichtspunkt." In: *Annalen der Physik* (1905), pp. 132–148 (cit. on p. 9).

[16] Nobelprize.org. *The Nobel Prize in Physics 1921*. ADDRESS: http://www.nobelprize.org/nobel_prizes/physics/laureates/1921/ (visited on 09/13/2013) (cit. on p. 9).

[17] D. M. Chapin, C. S. Fuller, and G. L. Pearson. "A New Silicon p-n Junction Photocell for Converting Solar Radiation into Electrical Power." In: *Journal of Applied Physics* 25.5 (1954), p. 676. DOI: 10.1063/1.1721711 (cit. on p. 9).

[18] D. Kearns and M. Calvin. "Photovoltaic Effect and Photoconductivity in Laminated Organic Systems." In: *The Journal of Chemical Physics* 29.4 (1958), p. 950. DOI: 10.1063/1.1744619 (cit. on p. 9).

[19] D. L. Morel, A. K. Ghosh, T. Feng, E. L. Stogryn, P. E. Purwin, R. F. Shaw, and C. Fishman. "High-efficiency organic solar cells." In: *Applied Physics Letters* 32.8 (1978), p. 495. DOI: 10.1063/1.90099 (cit. on p. 9).

[20] C. W. Tang. "Two-layer organic photovoltaic cell." In: *Applied Physics Letters* 48.2 (1986), p. 183. DOI: 10.1063/1.96937 (cit. on pp. 9, 16).

[21] B. O'Regan and M. Grätzel. "A low-cost, high-efficiency solar cell based on dye-sensitized colloidal TiO2 films." In: *Nature* 353 (1991), pp. 737–740 (cit. on p. 9).

[22] N. S. Sariciftci, L. Smilowitz, A. J. Heeger, and F. Wudl. "Photoinduced electron transfer from a conducting polymer to buckminsterfullerene."

In: *Science* 258.5087 (Nov. 1992), pp. 1474–1476. DOI: 10.1126/science. 258.5087.1474 (cit. on p. 9).

[23] W. U. Huynh, J. J. Dittmer, and A. P. Alivisatos. "Hybrid nanorod-polymer solar cells." In: *Science* 295.5564 (Mar. 2002), pp. 2425–2427. DOI: 10.1126/science.1069156 (cit. on pp. 10, 33).

[24] Heliatek. *Heliatek sets new world record efficiency of 10.7% for its organic tandem cell*. Apr. 2012. ADDRESS: http://www.heliatek.com/ newscenter/latest_news/heliatek-erzielt-mit-107-effizienz-neuen-weltrekord-fur-seine-organische-tandemzelle/?lang=en% 5C# (visited on 03/21/2013) (cit. on p. 10).

[25] Heliatek. *Heliatek consolidates its technology leadership by establishing a new world record for organic solar technology with a cell efficiency of 12%*. 2013. ADDRESS: http://www.heliatek.com/newscenter/latest_news/neuer-weltrekord-fur-organische-solarzellen-heliatek-behauptet-sich-mit-12-zelleffizienz-als-technologiefuhrer/?lang=en (visited on 09/18/2013) (cit. on p. 10).

[26] A. C. Mayer, S. R. Scully, B. E. Hardin, M. W. Rowell, and M. D. McGehee. "Polymer-based solar cells." In: *Materials Today* 10.11 (2007), pp. 28–33 (cit. on p. 10).

[27] A. Moliton and R. C. Hiorns. "The origin and development of (plastic) organic electronics." In: *Polymer International* 61.3 (Mar. 2012), pp. 337–341. DOI: 10.1002/pi.4173 (cit. on p. 11).

[28] Z. He, C. Zhong, S. Su, M. Xu, H. Wu, and Y. Cao. "Enhanced power-conversion efficiency in polymer solar cells using an inverted device

structure." In: *Nature Photonics* 6.9 (Aug. 2012), pp. 593–597. DOI: `10.1038/nphoton.2012.190` (cit. on pp. 11, 12, 32).

[29]   K. Norrman, M. V. Madsen, S. A. Gevorgyan, and F. C. Krebs. "Degradation Patterns in Water and Oxygen of an Inverted Polymer Solar Cell." In: *Journal of the American Chemical Society* 132.47 (Dec. 2010), pp. 16883–16892. DOI: `10.1021/ja106299g` (cit. on p. 12).

[30]   M. Jørgensen, K. Norrman, S. A. Gevorgyan, T. Tromholt, B. Andreasen, and F. C. Krebs. "Stability of polymer solar cells." In: *Advanced Materials* 24.5 (Feb. 2012), pp. 580–612. DOI: `10.1002/adma.201104187` (cit. on p. 12).

[31]   J. V. D. Horst and P. Bobbert. "Predicting polarizabilities and lifetimes of excitons on conjugated polymer chains." In: *Chemical Physics Letters* 334.February (2001), pp. 303–308 (cit. on p. 13).

[32]   J. Piprek. *Semiconductor Optoelectronic Devices: Introduction to Physics and Simulation*. Elsevier Science, 2003 (cit. on pp. 15, 68).

[33]   I. Hill, D. Milliron, J. Schwartz, and A. Kahn. "Organic semiconductor interfaces: electronic structure and transport properties." In: *Applied Surface Science* 166.1-4 (Oct. 2000), pp. 354–362. DOI: `10.1016/S0169-4332(00)00449-9` (cit. on p. 15).

[34]   N. Koch. "Organic electronic devices and their functional interfaces." In: *ChemPhysChem* 8.10 (July 2007), pp. 1438–1455. DOI: `10.1002/cphc.200700177` (cit. on p. 15).

[35]   M. M. Wienk, M. P. Struijk, and R. A. Janssen. "Low band gap polymer bulk heterojunction solar cells." In: *Chemical Physics Letters* 422.4-6 (May 2006), pp. 488–491. DOI: 10.1016/j.cplett.2006.03.027 (cit. on p. 16).

[36]   M. A. Green. "Self-consistent optical parameters of intrinsic silicon at 300K including temperature coefficients." In: *Solar Energy Materials and Solar Cells* 92.11 (Nov. 2008), pp. 1305–1310. DOI: 10.1016/j.solmat.2008.06.009 (cit. on p. 16).

[37]   G. Yu, J. Gao, J. C. Hummelen, F. Wudl, and A. J. Heeger. "Polymer Photovoltaic Cells: Enhanced Efficiencies via a Network of Internal Donor-Acceptor Heterojunctions." In: *Science* 270.5243 (Dec. 1995), pp. 1789–1791. DOI: 10.1126/science.270.5243.1789 (cit. on p. 16).

[38]   J. Halls, C. Walsh, and N. Greenham. "Efficient photodiodes from interpenetrating polymer networks." In: *Nature* 376 (1995), pp. 498–500 (cit. on p. 16).

[39]   G. Yu and A. J. Heeger. "Charge separation and photovoltaic conversion in polymer composites with internal donor/acceptor heterojunctions." In: *Journal of Applied Physics* 78.7 (1995), p. 4510. DOI: 10.1063/1.359792 (cit. on p. 17).

[40]   S. E. Shaheen, C. J. Brabec, N. S. Sariciftci, F. Padinger, T. Fromherz, and J. C. Hummelen. "2.5% efficient organic plastic solar cells." In: *Applied Physics Letters* 78.6 (2001), p. 841. DOI: 10.1063/1.1345834 (cit. on p. 17).

[41]   J. D. Kotlarski and P. W. M. Blom. "Ultimate performance of polymer:fullerene bulk heterojunction tandem solar cells." In: *Applied*

Physics Letters 98.5 (2011), p. 053301. DOI: 10.1063/1.3549693 (cit. on p. 17).

[42]   K. O. Sylvester-Hvid, S. Rettrup, and M. A. Ratner. "Two-Dimensional Model for Polymer-Based Photovoltaic Cells: Numerical Simulations of Morphology Effects." In: *The Journal of Physical Chemistry B* 108.14 (Apr. 2004), pp. 4296–4307. DOI: 10.1021/jp036467o (cit. on p. 17).

[43]   M. Gruber, B. Stickler, G. Trimmel, F. Schürrer, and K. Zojer. "Impact of energy alignment and morphology on the efficiency in inorganic–organic hybrid solar cells." In: *Organic Electronics* 11.12 (Dec. 2010), pp. 1999–2011. DOI: 10.1016/j.orgel.2010.08.015 (cit. on pp. 17, 39).

[44]   J. You, C.-C. Chen, Z. Hong, K. Yoshimura, K. Ohya, R. Xu, S. Ye, J. Gao, G. Li, and Y. Yang. "10.2% power conversion efficiency polymer tandem solar cells consisting of two identical sub-cells." In: *Advanced Materials* 25.29 (Aug. 2013), pp. 3973–3978. DOI: 10.1002/adma.201300964 (cit. on p. 18).

[45]   T. Ameri, G. Dennler, C. Lungenschmied, and C. J. Brabec. "Organic tandem solar cells: A review." In: *Energy & Environmental Science* 2.4 (2009), pp. 347–363. DOI: 10.1039/b817952b (cit. on p. 18).

[46]   W. Shockley and H. J. Queisser. "Detailed Balance Limit of Efficiency of p-n Junction Solar Cells." In: *Journal of Applied Physics* 32.3 (1961), p. 510. DOI: 10.1063/1.1736034 (cit. on p. 18).

[47]   A. DeVos. "Detailed balance limit of the efficiency of tandem solar cells."
       In: *Journal of Physics D: Applied Physics* 13.5 (May 1980), pp. 839–846. DOI:
       10.1088/0022-3727/13/5/018 (cit. on p. 18).

[48]   F. Meillaud, A. Shah, C. Droz, E. Vallat-Sauvain, and C. Miazza. "Effi-
       ciency limits for single-junction and tandem solar cells." In: *Solar En-
       ergy Materials and Solar Cells* 90.18-19 (Nov. 2006), pp. 2952–2959. DOI:
       10.1016/j.solmat.2006.06.002 (cit. on p. 19).

[49]   A. Goetzberger, C. Hebling, and H.-W. Schock. "Photovoltaic materials,
       history, status and outlook." In: *Materials Science and Engineering: R: Re-
       ports* 40.1 (Jan. 2003), pp. 1–46. DOI: 10.1016/S0927-796X(02)00092-X
       (cit. on p. 19).

[50]   R. Kroon, M. Lenes, J. C. Hummelen, P. W. M. Blom, and B. de Boer.
       "Small Bandgap Polymers for Organic Solar Cells (Polymer Material
       Development in the Last 5 Years)." In: *Polymer Reviews* 48.3 (Aug. 2008),
       pp. 531–582. DOI: 10.1080/15583720802231833 (cit. on p. 19).

[51]   Y. Kim, S. Cook, S. M. Tuladhar, S. A. Choulis, J. Nelson, J. R. Durrant,
       D. D. C. Bradley, M. Giles, I. McCulloch, C.-S. Ha, and M. Ree. "A strong
       regioregularity effect in self-organizing conjugated polymer films and
       high-efficiency polythiophene:fullerene solar cells." In: *Nature Materials*
       5.3 (Feb. 2006), pp. 197–203. DOI: 10.1038/nmat1574 (cit. on p. 19).

[52]   M. Mayukh, I. H. Jung, F. He, and L. Yu. "Incremental optimization in
       donor polymers for bulk heterojunction organic solar cells exhibiting
       high performance." In: *Journal of Polymer Science Part B: Polymer Physics*
       50.15 (Aug. 2012), pp. 1057–1070. DOI: 10.1002/polb.23102 (cit. on
       p. 19).

[53] J. You, L. Dou, K. Yoshimura, T. Kato, K. Ohya, T. Moriarty, K. Emery, C.-C. Chen, J. Gao, G. Li, and Y. Yang. "A polymer tandem solar cell with 10.6% power conversion efficiency." In: *Nature Communications* 4 (Feb. 2013), p. 1446. DOI: 10.1038/ncomms2411 (cit. on pp. 19, 32, 75).

[54] L.-M. Chen, Z. Xu, Z. Hong, and Y. Yang. "Interface investigation and engineering – achieving high performance polymer photovoltaic devices." In: *Journal of Materials Chemistry* 20.13 (2010), p. 2575. DOI: 10.1039/b925382c (cit. on p. 22).

[55] Y. Sun, M. Wang, X. Gong, J. H. Seo, B. B. Y. Hsu, F. Wudl, and A. J. Heeger. "Polymer bulk heterojunction solar cells: function and utility of inserting a hole transport and electron blocking layer into the device structure." In: *Journal of Materials Chemistry* 21.5 (2011), p. 1365. DOI: 10.1039/c0jm02224a (cit. on p. 23).

[56] V. Shrotriya, G. Li, Y. Yao, C.-W. Chu, and Y. Yang. "Transition metal oxides as the buffer layer for polymer photovoltaic cells." In: *Applied Physics Letters* 88.7 (2006), p. 073508. DOI: 10.1063/1.2174093 (cit. on p. 23).

[57] R. Li, Y. Peng, C. Ma, R. Wang, Y. Wang, H. Xie, T. Yang, J. Xie, S. Yan, and J. Zhang. "Effect of mixture ratio on the performance of MDMO-PPV:PCBM bulk heterojunction solar cells: A numerical study." In: *Materials Science and Engineering B* 172.3 (Sept. 2010), pp. 305–310. DOI: 10.1016/j.mseb.2010.06.013 (cit. on p. 23).

[58] A. Hayakawa, O. Yoshikawa, T. Fujieda, K. Uehara, and S. Yoshikawa. "High performance polythiophene/fullerene bulk-heterojunction solar

cell with a TiOx hole blocking layer." In: *Applied Physics Letters* 90.16 (2007), p. 163517. DOI: 10.1063/1.2730746 (cit. on p. 23).

[59]   A. Manor, E. A. Katz, T. Tromholt, and F. C. Krebs. "Enhancing functionality of ZnO hole blocking layer in organic photovoltaics." In: *Solar Energy Materials and Solar Cells* 98 (Mar. 2012), pp. 491–493. DOI: 10.1016/j.solmat.2011.11.026 (cit. on p. 23).

[60]   K. Zilberberg, A. Behrendt, M. Kraft, U. Scherf, and T. Riedl. "Ultrathin interlayers of a conjugated polyelectrolyte for low work-function cathodes in efficient inverted organic solar cells." In: *Organic Electronics* 14.3 (Mar. 2013), pp. 951–957. DOI: 10.1016/j.orgel.2013.01.018 (cit. on p. 23).

[61]   D. S. Hecht, L. Hu, and G. Irvin. "Emerging transparent electrodes based on thin films of carbon nanotubes, graphene, and metallic nanostructures." In: *Advanced Materials* 23.13 (Apr. 2011), pp. 1482–1513. DOI: 10.1002/adma.201003188 (cit. on p. 24).

[62]   K. S. Kim, Y. Zhao, H. Jang, S. Y. Lee, J. M. Kim, K. S. Kim, J.-H. Ahn, P. Kim, J.-Y. Choi, and B. H. Hong. "Large-scale pattern growth of graphene films for stretchable transparent electrodes." In: *Nature* 457.7230 (Feb. 2009), pp. 706–710. DOI: 10.1038/nature07719 (cit. on p. 24).

[63]   N. C. Greenham, X. Peng, and A. P. Alivisatos. "Charge separation and transport in conjugated-polymer/semiconductor-nanocrystal composites studied by photoluminescence quenching and photoconductivity." In: *Physical Review B* 54.24 (Dec. 1996), pp. 17628–17637 (cit. on p. 25).

[64] B. R. Saunders and M. L. Turner. "Nanoparticle-polymer photovoltaic cells." In: *Advances in Colloid and Interface Science* 138.1 (Apr. 2008), pp. 1–23. DOI: 10.1016/j.cis.2007.09.001 (cit. on p. 25).

[65] A. P. Alivisatos. "Semiconductor clusters, nanocrystals, and quantum dots." In: *Science* 271.5251 (1996), pp. 933–937 (cit. on pp. 25, 75, 95).

[66] S. Dayal, M. O. Reese, A. J. Ferguson, D. S. Ginley, G. Rumbles, and N. Kopidakis. "The Effect of Nanoparticle Shape on the Photocarrier Dynamics and Photovoltaic Device Performance of Poly(3-hexylthiophene):CdSe Nanoparticle Bulk Heterojunction Solar Cells." In: *Advanced Functional Materials* 20.16 (Aug. 2010), pp. 2629–2635. DOI: 10.1002/adfm.201000628 (cit. on p. 25).

[67] B. Vercelli, G. Zotti, A. Berlin, and M. Natali. "Self-Assembled Structures of Semiconductor Nanocrystals and Polymers for Photovoltaics. (3) PbSe Nanocrystal-Polymer LBL Multilayers. Optical, Electrochemical, Photoelectrochemical, and Photoconductive Properties." In: *Chemistry of Materials* 22.6 (Mar. 2010), pp. 2001–2009. DOI: 10.1021/cm903824e (cit. on p. 25).

[68] A. H. Khan, U. Thupakula, A. Dalui, S. Maji, A. Debangshi, and S. Acharya. "Evolution of Long Range Bandgap Tunable Lead Sulfide Nanocrystals with Photovoltaic Properties." In: *The Journal of Physical Chemistry C* 117.15 (Apr. 2013), pp. 7934–7939. DOI: 10.1021/jp402030p (cit. on p. 25).

[69] S. N. Sharma, U. Kumar, T. Vats, M. Arora, V. N. Singh, B. R. Mehta, K. Jain, R. Kakkar, and A. K. Narula. "Hybrid organic-inorganic (MEH-PPV/P3HT:CdSe) nanocomposites: linking film morphology to pho-

tostability." In: *The European Physical Journal Applied Physics* 50.2 (Mar. 2010), p. 20602. DOI: 10.1051/epjap/2010041 (cit. on p. 25).

[70] H. J. Cortina-Marrero, C. Martínez-Alonso, L. Hechavarría-Difur, and H. Hu. "Photovoltaic performance improvement in planar P3HT/CdS solar cells induced by structural, optical and electrical property modification in thermal annealed P3HT thin films." In: *The European Physical Journal Applied Physics* 63.1 (July 2013), p. 10201. DOI: 10.1051/epjap/2013120361 (cit. on p. 25).

[71] Y. N. Liang, K. Yu, Q. Yan, and X. Hu. "Colloidal CuInSe2 nanocrystals: from gradient stoichiometry toward homogeneous alloyed structure mediated by conducting polymer P3HT." In: *ACS Applied Materials & Interfaces* 5.10 (May 2013), pp. 4100–4106. DOI: 10.1021/am3032212 (cit. on p. 25).

[72] M. Arar, A. Pein, W. Haas, F. Hofer, K. Norrman, F. C. Krebs, T. Rath, and G. Trimmel. "Comprehensive Investigation of Silver Nanoparticle/Aluminum Electrodes for Copper Indium Sulfide/Polymer Hybrid Solar Cells." In: *The Journal of Physical Chemistry C* 116.36 (Sept. 2012), pp. 19191–19196. DOI: 10.1021/jp306242e (cit. on pp. 25, 28, 33, 34, 95, 96, 100, 103).

[73] T. Rath, V. Kaltenhauser, W. Haas, A. Reichmann, F. Hofer, and G. Trimmel. "Solution-processed small molecule/copper indium sulfide hybrid solar cells." In: *Solar Energy Materials and Solar Cells* 114 (July 2013), pp. 38–42. DOI: 10.1016/j.solmat.2013.02.024 (cit. on pp. 25, 33).

[74] E. Wang, L. Wang, L. Lan, C. Luo, W. Zhuang, J. Peng, and Y. Cao. "High-performance polymer heterojunction solar cells of a polysilaflu-

orene derivative." In: *Applied Physics Letters* 92.3 (2008), p. 033307. DOI: 10.1063/1.2836266 (cit. on pp. 25, 26, 34, 97, 98).

[75] P. W. M. Blom, V. D. Mihailetchi, L. J. A. Koster, and D. E. Markov. "Device Physics of Polymer:Fullerene Bulk Heterojunction Solar Cells." In: *Advanced Materials* 19.12 (June 2007), pp. 1551–1566. DOI: 10.1002/adma.200601093 (cit. on p. 26).

[76] C. Zhang, S.-W. Tong, C.-Y. Jiang, E.-T. Kang, D. S. H. Chan, and C. Zhu. "Origin of Different Dependences of Open-Circuit Voltage on the Electrodes in Layered and Bulk Heterojunction Organic Photovoltaic Cells." In: *IEEE Transactions on Electron Devices* 57.2 (Feb. 2010), pp. 397–405. DOI: 10.1109/TED.2009.2036787 (cit. on p. 26).

[77] J. C. Blakesley and D. Neher. "Relationship between energetic disorder and open-circuit voltage in bulk heterojunction organic solar cells." In: *Physical Review B* 84.7 (Aug. 2011), p. 075210. DOI: 10.1103/PhysRevB.84.075210 (cit. on p. 26).

[78] D. Credgington and J. R. Durrant. "Insights from Transient Optoelectronic Analyses on the Open-Circuit Voltage of Organic Solar Cells." In: *The Journal of Physical Chemistry Letters* 3.11 (June 2012), pp. 1465–1478. DOI: 10.1021/jz300293q (cit. on p. 26).

[79] W. Yue, S. Han, R. Peng, W. Shen, H. Geng, F. Wu, S. Tao, and M. Wang. "CuInS2 quantum dots synthesized by a solvothermal route and their application as effective electron acceptors for hybrid solar cells." In: *Journal of Materials Chemistry* 20.35 (2010), p. 7570. DOI: 10.1039/c0jm00611d (cit. on p. 26).

[80]   H. Lewerenz. "Development of copperindiumdisulfide into a solar material." In: *Solar Energy Materials and Solar Cells* 83.4 (July 2004), pp. 395–407. DOI: 10.1016/j.solmat.2004.02.034 (cit. on pp. 26, 43, 62).

[81]   A. M. Smith and S. Nie. "Semiconductor nanocrystals: structure, properties, and band gap engineering." In: *Accounts of Chemical Research* 43.2 (Feb. 2010), pp. 190–200. DOI: 10.1021/ar9001069 (cit. on pp. 27, 32).

[82]   E. Arici, N. Sariciftci, and D. Meissner. "Hybrid solar cells based on nanoparticles of CuInS2 in organic matrices." In: *Advanced Functional Materials* 2 (2003), pp. 165–171 (cit. on pp. 27, 34, 57, 63, 68, 97).

[83]   F. M. Courtel, R. W. Paynter, B. Marsan, and M. Morin. "Synthesis, Characterization, and Growth Mechanism of n-Type CuInS2 Colloidal Particles." In: *Chemistry of Materials* 21.16 (Aug. 2009), pp. 3752–3762. DOI: 10.1021/cm900601k (cit. on p. 27).

[84]   E. Maier, A. Fischereder, W. Haas, G. Mauthner, J. Albering, T. Rath, F. Hofer, E. J. List, and G. Trimmel. "Metal sulfide–polymer nanocomposite thin films prepared by a direct formation route for photovoltaic applications." In: *Thin Solid Films* 519.13 (Apr. 2011), pp. 4201–4206. DOI: 10.1016/j.tsf.2011.02.020 (cit. on pp. 28, 75).

[85]   T. Rath and G. Trimmel. "In situ syntheses of semiconducting nanoparticles in conjugated polymer matrices and their application in photovoltaics." In: *Hybrid Materials* 1 (2013), pp. 15–36. DOI: 10.2478/hyma-2013-0003 (cit. on p. 28).

[86]   M. Dardo. *Nobel Laureates and Twentieth-Century Physics*. Nobel Laureates and 20th Century Physics. Cambridge University Press, 2004 (cit. on p. 30).

[87]   Z. Chen, H. Zhang, X. Du, X. Cheng, X. Chen, Y. Jiang, and B. Yang. "From planar-heterojunction to n–i structure: an efficient strategy to improve short-circuit current and power conversion efficiency of aqueous-solution-processed hybrid solar cells." In: *Energy & Environmental Science* 6.5 (2013), p. 1597. DOI: 10.1039/c3ee40481a (cit. on p. 32).

[88]   S. Ren, L.-Y. Chang, S.-K. Lim, J. Zhao, M. Smith, N. Zhao, V. Bulović, M. Bawendi, and S. Gradecak. "Inorganic-organic hybrid solar cell: bridging quantum dots to conjugated polymer nanowires." In: *Nano Letters* 11.9 (Sept. 2011), pp. 3998–4002. DOI: 10.1021/nl202435t (cit. on pp. 32, 35, 75).

[89]   C. de Mello Donegá. "Synthesis and properties of colloidal hetero-nanocrystals." In: *Chemical Society Reviews* 40.3 (Mar. 2011), pp. 1512–1546. DOI: 10.1039/c0cs00055h (cit. on p. 32).

[90]   J. Seo, M. J. Cho, D. Lee, A. N. Cartwright, and P. N. Prasad. "Efficient Heterojunction Photovoltaic Cell Utilizing Nanocomposites of Lead Sulfide Nanocrystals and a Low-Bandgap Polymer." In: *Advanced Materials* 23.34 (Sept. 2011), pp. 3984–3988. DOI: 10.1002/adma.201101912 (cit. on pp. 32, 75).

[91]   H. C. Leventis, S. P. King, A. Sudlow, M. S. Hill, K. C. Molloy, and S. A. Haque. "Nanostructured hybrid polymer-inorganic solar cell active layers formed by controllable in situ growth of semiconducting sul-

fide networks." In: *Nano Letters* 10.4 (Apr. 2010), pp. 1253–1258. DOI: 10.1021/nl903787j (cit. on pp. 33, 35).

[92]   S. Dowland, T. Lutz, A. Ward, S. P. King, A. Sudlow, M. S. Hill, K. C. Molloy, and S. A. Haque. "Direct growth of metal sulfide nanoparticle networks in solid-state polymer films for hybrid inorganic-organic solar cells." In: *Advanced Materials* 23.24 (June 2011), pp. 2739–2744. DOI: 10.1002/adma.201100625 (cit. on pp. 33, 75).

[93]   T. Rath, M. Edler, W. Haas, A. Fischereder, S. Moscher, A. Schenk, R. Trattnig, M. Sezen, G. Mauthner, A. Pein, D. Meischler, K. Bartl, R. Saf, N. Bansal, S. A. Haque, F. Hofer, E. J. List, and G. Trimmel. "A Direct Route Towards Polymer/Copper Indium Sulfide Nanocomposite Solar Cells." In: *Advanced Energy Materials* 1.6 (Nov. 2011), pp. 1046–1050. DOI: 10.1002/aenm.201100442 (cit. on pp. 33, 36, 43, 45, 46, 62, 63, 75, 76, 78, 80, 86, 95, 97).

[94]   N. Bansal, F. T. F. O'Mahony, T. Lutz, and S. A. Haque. "Solution Processed Polymer-Inorganic Semiconductor Solar Cells Employing Sb2S3 as a Light Harvesting and Electron Transporting Material." In: *Advanced Energy Materials* 3.8 (Apr. 2013), pp. 986–990. DOI: 10.1002/aenm.201300017 (cit. on p. 33).

[95]   L. X. Reynolds, T. Lutz, S. Dowland, A. MacLachlan, S. King, and S. A. Haque. "Charge photogeneration in hybrid solar cells: a comparison between quantum dots and in situ grown CdS." In: *Nanoscale* 4.5 (Mar. 2012), pp. 1561–1564. DOI: 10.1039/c2nr12081j (cit. on pp. 33, 44, 46, 75, 76).

[96]   J. Yang, A. Tang, R. Zhou, and J. Xue. "Effects of nanocrystal size and device aging on performance of hybrid poly(3-hexylthiophene):CdSe nanocrystal solar cells." In: *Solar Energy Materials and Solar Cells* 95.2 (Feb. 2011), pp. 476–482. DOI: 10.1016/j.solmat.2010.09.005 (cit. on pp. 33, 42).

[97]   D. Li, R. Liang, H. Yue, P. Wang, L.-M. Fu, J.-P. Zhang, and X.-C. Ai. "Influence of Donor and Acceptor Mass Ratios on P3HT: PCBM Film Structure and Device Performance." In: *Acta Physico- Chimica Sinica* 28.6 (2012), pp. 1373–1379. DOI: 10.3866/PKU.WHXB201204061 (cit. on p. 34).

[98]   E. A. Parlak. "The blend ratio effect on the photovoltaic performance and stability of poly (3-hexylthiophene):[6,6]-phenyl-C61 butyric acid methyl ester (PCBM) and poly(3-octylthiophene):PCBM solar cells." In: *Solar Energy Materials and Solar Cells* 100 (May 2012), pp. 174–184. DOI: 10.1016/j.solmat.2012.01.011 (cit. on p. 34).

[99]   J. Y. Lek, Y. M. Lam, J. Niziol, and M. Marzec. "Understanding polycarbazole-based polymer:CdSe hybrid solar cells." In: *Nanotechnology* 23.31 (Aug. 2012), p. 315401. DOI: 10.1088/0957-4484/23/31/315401 (cit. on p. 34).

[100] Y. Zhou, M. Eck, C. Veit, B. Zimmermann, F. Rauscher, P. Niyamakom, S. Yilmaz, I. Dumsch, S. Allard, and U. Scherf. "Efficiency enhancement for bulk-heterojunction hybrid solar cells based on acid treated CdSe quantum dots and low bandgap polymer PCPDTBT." In: *Solar Energy Materials and Solar Cells* 95.4 (Apr. 2011), pp. 1232–1237. DOI: 10.1016/j.solmat.2010.12.041 (cit. on p. 34).

[101] K. Yoshino, K. Nomoto, A. Kinoshita, T. Ikari, Y. Akaki, and T. Yoshitake. "Dependence of Cu/In ratio of structural and electrical characterization of CuInS2 crystal." In: *Journal of Materials Science: Materials in Electronics* 19.4 (June 2007), pp. 301–304. DOI: 10.1007/s10854-007-9334-1 (cit. on p. 34).

[102] S. Dayal, N. Kopidakis, D. C. Olson, D. S. Ginley, and G. Rumbles. "Photovoltaic devices with a low band gap polymer and CdSe nanostructures exceeding 3% efficiency." In: *Nano Letters* 10.1 (Jan. 2010), pp. 239–242. DOI: 10.1021/nl903406s (cit. on p. 34).

[103] G. Dennler, M. C. Scharber, and C. J. Brabec. "Polymer-Fullerene Bulk-Heterojunction Solar Cells." In: *Advanced Materials* 21.13 (Apr. 2009), pp. 1323–1338. DOI: 10.1002/adma.200801283 (cit. on p. 35).

[104] S. D. Oosterhout, M. M. Wienk, S. S. van Bavel, R. Thiedmann, L. J. A. Koster, J. Gilot, J. Loos, V. Schmidt, and R. A. J. Janssen. "The effect of three-dimensional morphology on the efficiency of hybrid polymer solar cells." In: *Nature Materials* 8.10 (Oct. 2009), pp. 818–824. DOI: 10.1038/nmat2533 (cit. on p. 35).

[105] G. Cliff and G. W. Lorimer. "The quantitative analysis of thin specimens." In: *Journal of Microscopy* 103.2 (Mar. 1975), pp. 203–207. DOI: 10.1111/j.1365-2818.1975.tb03895.x (cit. on pp. 37, 99).

[106] L. A. A. Pettersson, L. S. Roman, and O. Inganas. "Modeling photocurrent action spectra of photovoltaic devices based on organic thin films." In: *Journal of Applied Physics* 86.1 (1999), p. 487. DOI: 10.1063/1.370757 (cit. on pp. 39, 57).

[107]   M. Gruber, B. Stickler, S. Possanner, K. Zojer, and F. Schürrer. "Simulation of the performance of organic electronic devices based on a two-dimensional drift-diffusion approach." In: *Communications in Applied and Industrial Mathematics* 2 (2011). DOI: 10.1685/journal.caim.384 (cit. on p. 39).

[108]   B. Stickler, M. Gruber, G. Trimmel, F. Schürrer, and K. Zojer. "Influence of transport-related material parameters on the I–V characteristic of inorganic–organic hybrid solar cells." In: *Organic Electronics* 12.8 (Aug. 2011), pp. 1434–1445. DOI: 10.1016/j.orgel.2011.04.021 (cit. on p. 39).

[109]   E. Maier, T. Rath, W. Haas, O. Werzer, R. Saf, F. Hofer, D. Meissner, O. Volobujeva, S. Bereznev, E. Mellikov, H. Amenitsch, R. Resel, and G. Trimmel. "CuInS2–Poly(3-(ethyl-4-butanoate)thiophene) nanocomposite solar cells: Preparation by an in situ formation route, performance and stability issues." In: *Solar Energy Materials and Solar Cells* 95.5 (May 2011), pp. 1354–1361. DOI: 10.1016/j.solmat.2010.12.025 (cit. on pp. 43, 62, 75).

[110]   F. T. F. O'Mahony, T. Lutz, N. Guijarro, R. Gómez, and S. A. Haque. "Electron and hole transfer at metal oxide/Sb2S3/spiro-OMeTAD heterojunctions." In: *Energy & Environmental Science* 5.12 (2012), pp. 9760–9764. DOI: 10.1039/c2ee23037b (cit. on p. 45).

[111]   N. Bansal, L. X. Reynolds, A. MacLachlan, T. Lutz, R. S. Ashraf, W. Zhang, C. B. Nielsen, I. McCulloch, D. G. Rebois, T. Kirchartz, M. S. Hill, K. C. Molloy, J. Nelson, and S. A. Haque. "Influence of Crystallinity and Energetics on Charge Separation in Polymer–Inorganic Nanocomposite

Films for Solar Cells." In: *Scientific Reports* 3 (Mar. 2013), pp. 1–8. DOI: 10.1038/srep01531 (cit. on p. 45).

[112] Refractiveindex.info. *RefractiveIndex.INFO: Refractive index database*. ADDRESS: http://refractiveindex.info/ (visited on 05/05/2013) (cit. on p. 58).

[113] L. A. A. Pettersson, S. Ghosh, and O. Inganas. "Optical anisotropy in thin films of poly (3, 4-ethylenedioxythiophene)–poly (4-styrenesulfonate)." In: *Organic Electronics* 3 (2002), pp. 143–148 (cit. on p. 58).

[114] M. Alonso, K. Wakita, J. Pascual, M. Garriga, and N. Yamamoto. "Optical functions and electronic structure of CuInSe2, CuGaSe2, CuInS2, and CuGaS2." In: *Physical Review B* 63.7 (Jan. 2001), p. 075203. DOI: 10.1103/PhysRevB.63.075203 (cit. on p. 58).

[115] M. Planck and J. V. Murphy. *Where is Science Going?* W.W. Norton, Incorporated, 1932 (cit. on p. 61).

[116] T. K. Chaudhuri, A. J. Kothari, D. Tiwari, and A. Ray. "Photoconducting nanocomposite films of PbS nanocrystals in insulating polystyrene." In: *Physica Status Solidi (a)* 210.2 (Feb. 2013), pp. 356–360. DOI: 10.1002/pssa.201228566 (cit. on p. 62).

[117] R. Motoyoshi, T. Oku, A. Suzuki, K. Kikuchi, S. Kikuchi, B. Jeyadevan, and J. Cuya. "Fabrication and Characterization of Copper System Compound Semiconductor Solar Cells." In: *Advances in Materials Science and Engineering* 2010 (2010), pp. 1–11. DOI: 10.1155/2010/562842 (cit. on p. 63).

[118] H. Zhong, S. S. Lo, T. Mirkovic, Y. Li, Y. Ding, Y. Li, and G. D. Scholes. "Noninjection gram-scale synthesis of monodisperse pyramidal CuInS2 nanocrystals and their size-dependent properties." In: *ACS Nano* 4.9 (Sept. 2010), pp. 5253–5262. DOI: 10.1021/nn1015538 (cit. on p. 68).

[119] J. Tang and E. H. Sargent. "Infrared colloidal quantum dots for photovoltaics: fundamentals and recent progress." In: *Advanced Materials* 23.1 (Jan. 2011), pp. 12–29. DOI: 10.1002/adma.201001491 (cit. on p. 68).

[120] V. V. Kislyuk, P. S. Smertenko, O. P. Dimitriev, and A. A. Pud. "A photovoltaic response of a Schottky diode based on the conducting polymer PEDOT:PSS and inorganic semiconductors." In: *The European Physical Journal Applied Physics* 51.2 (July 2010), p. 20301. DOI: 10.1051/epjap/2010095 (cit. on p. 69).

[121] T. Jevremovic. *Nuclear Principles in Engineering*. New York: Springer-Verlag, 2005. DOI: 10.1007/b101136 (cit. on p. 73).

[122] L. J. A. Koster, S. E. Shaheen, and J. C. Hummelen. "Pathways to a New Efficiency Regime for Organic Solar Cells." In: *Advanced Energy Materials* 2.10 (Oct. 2012), pp. 1246–1253. DOI: 10.1002/aenm.201200103 (cit. on p. 75).

[123] S. A. Gevorgyan, A. J. Medford, E. Bundgaard, S. B. Sapkota, H.-F. Schleiermacher, B. Zimmermann, U. Würfel, A. Chafiq, M. Lira-Cantu, T. Swonke, M. Wagner, C. J. Brabec, O. Haillant, E. Voroshazi, T. Aernouts, R. Steim, J. A. Hauch, A. Elschner, M. Pannone, M. Xiao, A. Langzettel, D. Laird, M. T. Lloyd, T. Rath, E. Maier, G. Trimmel, M. Hermenau, T. Menke, K. Leo, R. Rösch, M. Seeland, H. Hoppe, T. J. Nagle, K. B. Burke, C. J. Fell, D. Vak, T. Singh, S. E. Watkins, Y. Gala-

gan, A. Manor, E. A. Katz, T. Kim, K. Kim, P. M. Sommeling, W. J. Verhees, S. C. Veenstra, M. Riede, M. Greyson Christoforo, T. R. Currier, V. Shrotriya, G. Schwartz, and F. C. Krebs. "An inter-laboratory stability study of roll-to-roll coated flexible polymer solar modules." In: *Solar Energy Materials and Solar Cells* 95.5 (May 2011), pp. 1398–1416. DOI: 10.1016/j.solmat.2011.01.010 (cit. on p. 75).

[124] NREL. *NREL Efficiency Chart*. ADDRESS: http://www.nrel.gov/ncpv/images/efficiency_chart.jpg (visited on 06/13/2013) (cit. on p. 75).

[125] Z. He, C. Zhong, X. Huang, W.-Y. Wong, H. Wu, L. Chen, S. Su, and Y. Cao. "Simultaneous enhancement of open-circuit voltage, short-circuit current density, and fill factor in polymer solar cells." In: *Advanced Materials* 23.40 (Oct. 2011), pp. 4636–4643. DOI: 10.1002/adma.201103006 (cit. on p. 75).

[126] Konarka. *Konarka Technologies Advances Award Winning Power Plastic Solar Cell Efficiency with 9% Certification*. ADDRESS: http://konarka.com/index.php/site/pressreleasedetail/konarka_technologies_advances_award_winning_power_plastic_solar_cell_effici (visited on 05/12/2012) (cit. on p. 75).

[127] H. Xiang, S.-H. Wei, and X. Gong. "Identifying Optimal Inorganic Nanomaterials for Hybrid Solar Cells." In: *The Journal of Physical Chemistry C* 113.43 (Oct. 2009), pp. 18968–18972. DOI: 10.1021/jp907942p (cit. on pp. 75, 95).

[128] E. Martínez-Ferrero, J. Albero, and E. Palomares. "Materials, Nanomorphology, and Interfacial Charge Transfer Reactions in Quantum Dot/Polymer Solar Cell Devices." In: *The Journal of Physical Chemistry*

Letters 1.20 (Oct. 2010), pp. 3039–3045. DOI: 10.1021/jz101228z (cit. on pp. 75, 95).

[129] R. Zhou, Y. Zheng, L. Qian, Y. Yang, P. H. Holloway, and J. Xue. "Solution-processed, nanostructured hybrid solar cells with broad spectral sensitivity and stability." In: *Nanoscale* 4.11 (June 2012), pp. 3507–3514. DOI: 10.1039/c2nr30210a (cit. on p. 75).

[130] K. F. Jeltsch, M. Schädel, J.-B. Bonekamp, P. Niyamakom, F. Rauscher, H. W. A. Lademann, I. Dumsch, S. Allard, U. Scherf, and K. Meerholz. "Efficiency Enhanced Hybrid Solar Cells Using a Blend of Quantum Dots and Nanorods." In: *Advanced Functional Materials* 22.2 (Jan. 2012), pp. 397–404. DOI: 10.1002/adfm.201101809 (cit. on p. 75).

[131] D. Celik, M. Krueger, C. Veit, H. F. Schleiermacher, B. Zimmermann, S. Allard, I. Dumsch, U. Scherf, F. Rauscher, and P. Niyamakom. "Performance enhancement of CdSe nanorod-polymer based hybrid solar cells utilizing a novel combination of post-synthetic nanoparticle surface treatments." In: *Solar Energy Materials and Solar Cells* 98 (Mar. 2012), pp. 433–440. DOI: 10.1016/j.solmat.2011.11.049 (cit. on p. 75).

[132] J. Albero, Y. Zhou, M. Eck, F. Rauscher, P. Niyamakom, I. Dumsch, S. Allard, U. Scherf, M. Krüger, and E. Palomares. "Photo-induced charge recombination kinetics in low bandgap PCPDTBT polymer:CdSe quantum dot bulk heterojunction solar cells." In: *Chemical Science* 2.12 (2011), pp. 2396–2401. DOI: 10.1039/c1sc00514f (cit. on p. 75).

[133] E. Arici, H. Hoppe, F. Schäffler, D. Meissner, M. Malik, and N. Sariciftci. "Hybrid solar cells based on inorganic nanoclusters and conju-

gated polymers." In: *Thin Solid Films* 451-452 (Mar. 2004), pp. 612–618. DOI: 10.1016/j.tsf.2003.11.026 (cit. on p. 75).

[134] Y. Yang, H. Zhong, Z. Bai, B. Zou, Y. Li, and G. D. Scholes. "Transition from Photoconductivity to Photovoltaic Effect in P3HT/CuInSe2 Composites." In: *The Journal of Physical Chemistry C* 116.13 (Apr. 2012), pp. 7280–7286. DOI: 10.1021/jp300973c (cit. on p. 75).

[135] D. Cui, J. Xu, T. Zhu, G. Paradee, S. Ashok, and M. Gerhold. "Harvest of near infrared light in PbSe nanocrystal-polymer hybrid photovoltaic cells." In: *Applied Physics Letters* 88.18 (2006), p. 183111. DOI: 10.1063/1.2201047 (cit. on p. 75).

[136] F. C. Krebs, M. Jørgensen, K. Norrman, O. Hagemann, J. Alstrup, T. D. Nielsen, J. Fyenbo, K. Larsen, and J. Kristensen. "A complete process for production of flexible large area polymer solar cells entirely using screen printing—First public demonstration." In: *Solar Energy Materials and Solar Cells* 93.4 (Apr. 2009), pp. 422–441. DOI: 10.1016/j.solmat.2008.12.001 (cit. on p. 76).

[137] Y. Zhang, X.-D. Dang, C. Kim, and T.-Q. Nguyen. "Effect of Charge Recombination on the Fill Factor of Small Molecule Bulk Heterojunction Solar Cells." In: *Advanced Energy Materials* 1.4 (July 2011), pp. 610–617. DOI: 10.1002/aenm.201100040 (cit. on p. 76).

[138] R. Steim, F. R. Kogler, and C. J. Brabec. "Interface materials for organic solar cells." In: *Journal of Materials Chemistry* 20.13 (2010), p. 2499. DOI: 10.1039/b921624c (cit. on pp. 76, 87).

[139] B. Schaffer, C. Mitterbauer, A. Schertel, A. Pogantsch, S. Rentenberger, E. Zojer, and F. Hofer. "Cross-section analysis of organic light-emitting diodes." In: *Ultramicroscopy* 101.2-4 (Nov. 2004), pp. 123–128. DOI: 10.1016/j.ultramic.2004.05.007 (cit. on pp. 78, 81, 98).

[140] H. A. Atwater and A. Polman. "Plasmonics for improved photovoltaic devices." In: *Nature Materials* 9.3 (Mar. 2010), pp. 205–213. DOI: 10.1038/nmat2629 (cit. on p. 85).

[141] J. A. Scholl, A. L. Koh, and J. A. Dionne. "Quantum plasmon resonances of individual metallic nanoparticles." In: *Nature* 483.7390 (Mar. 2012), pp. 421–427. DOI: 10.1038/nature10904 (cit. on p. 85).

[142] C. F. Bohren and D. R. Huffman. *Absorption and scattering of light by small particles*. Wiley science paperback series. Wiley, 1983 (cit. on p. 85).

[143] A. Moliton and J.-M. Nunzi. "How to model the behaviour of organic photovoltaic cells." In: *Polymer International* 55.6 (June 2006), pp. 583–600. DOI: 10.1002/pi.2038 (cit. on p. 87).

[144] C. Waldauf, M. C. Scharber, P. Schilinsky, J. A. Hauch, and C. J. Brabec. "Physics of organic bulk heterojunction devices for photovoltaic applications." In: *Journal of Applied Physics* 99.10 (2006), p. 104503. DOI: 10.1063/1.2198930 (cit. on p. 87).

[145] A. Salam, P. A. M. Dirac, J. M. Evans, and G. Watts. *Unification of Fundamental Forces: The First 1988 Dirac Memorial Lecture*. Cambridge University Press, 1990 (cit. on p. 93).

[146] M. A. Green, K. Emery, Y. Hishikawa, W. Warta, and E. D. Dunlop. "Solar cell efficiency tables (version 41)." In: *Progress in Photovoltaics:*

Research and Applications 21.1 (Jan. 2013), pp. 1–11. DOI: 10.1002/pip.2352 (cit. on p. 95).

[147] N. Blouin, A. Michaud, and M. Leclerc. "A Low-Bandgap Poly(2,7-Carbazole) Derivative for Use in High-Performance Solar Cells." In: *Advanced Materials* 19.17 (Sept. 2007), pp. 2295–2300. DOI: 10.1002/adma.200602496 (cit. on pp. 97, 98).

[148] C. J. Brabec, N. S. Sariciftci, and J. C. Hummelen. "Plastic Solar Cells." In: *Advanced Functional Materials* 11.1 (Feb. 2001), pp. 15–26. DOI: 10.1002/1616-3028(200102)11:1<15::AID-ADFM15>3.0.CO;2-A (cit. on p. 97).

[149] A. L. Lavoisier and W. Creech. *Elements of Chemistry: In a New Systematic Order, Containing All the Modern Discoveries. Illustrated with Thirteen Copperplates.* William Creech, and sold in London, 1790 (cit. on p. 104).

Appendix F.

List of Publications

Articles in Professional Journals

Arar, M.; Pein, A.; Haas, W.; Hofer, F.; Norrman, K.; Krebs, F. C.; Rath, T.; Trimmel, G.: "Comprehensive Investigation of Silver Nanoparticle/Aluminum Electrodes for Copper Indium Sulfide/Polymer Hybrid Solar Cells." - in: *The Journal of Physical Chemistry C* 116 (2012) 36, S. 19191 - 19196.

Arar, M.; Gruber, M.; Edler, M.; Haas, W.; Hofer, F.; Bansal, N.; Reynolds, L. X.; Haque, S. A.; Zojer, K.; Trimmel, G.; Rath, T.: "Influence of morphology and polymer:nanoparticle ratio on device performance of hybrid solar cells – an approach in experiment and simulation" - revised submission to: *Nanotechnology*

Arar, M.; Haas, W.; Hofer, F.; Rath, T.; Trimmel, G.: "Silver-modified Aluminum Electrodes in Polymer:PCBM Solar Cells" - submitted to and accepted to publish at the *39th Photovoltaic Specialists Conference Proceedings (IEEE).*

Posters within Academic Meetings

Arar, M.; Pein, A.; Haas, W.; Kaltenhauser, V.; Fradler, C.; Dunst, S.; Hofer, F.; Norrman, K.; Krebs, F. C.; Rath, T.; Trimmel, G.: "Fill Factor Enhancement for PSiF-DBT/CIS Solar Cells through Silver-modified Aluminum Electrodes." - in: *Plastic Electronics 2012.* Dresden: 09.10.2012

Rath, T.; Edler, M.; Haas, W.; Moscher, S.; Pein, A.; Kaltenhauser, V.; Dunst, S.; Arar, M.; Fradler, C.; Saf, R.; Trattnig, R.; Jäger, M.; Postl, M.; Seidl, M.; Bansal, N.; Haque, S. A.; Hofer, F.; List, E.; Trimmel, G.: "A Direct In Situ-Preparation Route for Organic-Inorganic Hybrid Solar Cells Based on Metal Sulfides and Conjugated Polymers." - in: *Plastic Electronics 2012.* Dresden: 09.10.2012

Rath, T.; Edler, M.; Haas, W.; Moscher, S.; Trattnig, R.; Jäger, M.; Pein, A.; Kaltenhauser, V.; Dunst, S.; Arar, M.; Fradler, C.; Saf, R.; Postl, M.; Seidl, M.; Bansal, N.; Haque, S. A.; Hofer, F.; List, E.; Trimmel, G.: "Polymer / copper indium sulphide hybrid solar cells." - in: *EMRS Spring Meeting 2012.* Straßburg: 14.05.2012

Oral Presentations

Arar, M.; Pein, A.; Dunst, S.; Haas, W.; Hofer, F.; Norrman, K.; Krebs, F. C.; Rath, T.; Trimmel, G.: "Comparing Efficiency and Stability of Conventional Cathodes with a Novel Silver Nanoparticle/Aluminum Cathode in Hybrid Solar Cells." - in: *39th IEEE Photovoltaic Specialists Conference.* Tampa, FL am: 16.06.2013

Arar, M.; Schütz, D.; Kurta, C.; Sprengel, W.; Reichmann, K.: "Determination and Analysis of Diffusion of Metals in PZT." - in: *ICCPS-11 (International Conference on Ceramic Processing Science).* Zürich am: 29.08.2010Rath, T.;

Rath, T.; Arar, M.; Pein, A.; Fradler, C.; Kaltenhauser, V.; Edler, M.; Moscher, S.; Trattnig, R.; List, E.; Haas, W.; Dunst, S.; Hofer, F.; Trimmel, G.: "Copper Indium Sulphide / Polymer Nanocomposite Solar Cells." - in: *27th European PV Solar Energy Conference and Exhibition.* Frankfurt am: 25.09.2012

Schütz, D.; Kurta, C.; Arar, M.; Reichmann, K.: "A novel way to measure diffusional profiles in metal-ceramic composites." - in: *Electroceramics XII.* Trondheim am: 15.06.2010

Appendix G.

Curriculum Vitae

Persönliche Daten

Geboren in	Wels, am 15. 11. 1980
Adresse	Fichtestraße 71/8, 8020 Graz
E-Mail-Adresse	arar.mario@gmail.com
Telefon	+43 681 20301990
Familienstand	in Partnerschaft lebend
Staatsbürger-schaft	Österreich

Ausbildung

Universität	*01/2011–dato*	Technische Universität, Graz

Doktoratsstudium der techn. Wissenschaften (Techn. Chemie)

· Vorauss. Abschluss: 10/2013

· Institut: CD-Labor für Nanokompositsolarzellen

· Betreuer: Prof. Gregor Trimmel

10/2000–11/2010   Technische Universität, Graz

Diplomstudium: Technische Physik (Dipl.-Ing.)

· Diplomarbeit: "Diffusion in Lead-Zirconate-Titanate Ceramics (PZT)
measured by Laser Ablation in Combination with Mass Spectrometry"

· Institut: CD-Labor für Ferroische Materialien

· Betreuer: Prof. Wolfgang SPRENGEL & Prof. Klaus REICHMANN

BHS   *09/1994–07/1999*   Höhere Technische Bundeslehranstalt, Wels

Ausbildungszweig: Elektrotechnik

· Leistungszweig: Energiesysteme und Leistungselektronik
(mit Matura abgeschlossen)

BERUFSERFAHRUNG

Betreuung   *03/2011–dato*   Technische Universität, Graz

Betreuung von Studierenden
Laborübungen, Projektlabore, Abschlussarbeiten

IT Support   *03/2008–08/2009*   Technische Universität, Graz

First-Level-Support mit erweiterten Aufgaben am Zentralen Informatikdienst der
Technischen Universität Graz
Helpdesk, Fernwartung, Betreuung von Instituten vor Ort

Content   *08/2007–02/2008*   bit media e-Learning solutions, Graz
Entwicklung

Programmieren von Lektionen und Übungen für ECDL-Kurse sowie
e-Learning-Module

Bundesheer

Grundwehrdienst	*08/1999–04/2000*	Panzerpionierkompanie, Mautern/Donau
	vollständig abgeleistet	

Zusätzliche Qualifikationen

EDV-	· Origin
Kenntnisse	· MS Office XP–2013
	· LaTeX
	· Programmierkenntnisse (Matlab, C)
	· OS: Windows, MacOS X, Linux (Ubuntu)

Sprachen	Englisch ·	Verhandlungssicher
	Kroatisch ·	Gute Kenntnisse
	Spanisch ·	Grundkenntnisse
	Deutsch ·	Muttersprache

Weiterbildungen	Seminare (TU Graz, Universität Graz)
	· Projektmanagement
	· Führungsverhalten
	· Erfolgreiche Teamarbeit in Projekten
	· Erfolgreiche Rhetorik und professionelle Präsentationstechnik
	· Selbstorganisation, Zeitmanagement und Arbeitstechniken

Persönliche Interessen

Sport	Wandern/Bergsteigen · Fußball · Beach-/Volleyball · Radtouren
Sonstiges	Brett- und Kommunikationsspiele · Lesen · Reisen